INSTITUT SUPÉRIEUR DE L'AÉRONAUTIQUE ET DE L'ESPACE

DESIGN AND ANALYSIS OF THE ATTITUDE CONTROL SYSTEM FOR THE S2TEP MISSION

a thesis submitted in partial fulfilment of the requirements for the degree of

M.Sc. in Aerospace Engineering

presented by:

José Alfredo MACÉS HÉRNANDEZ

Supervisors:

Dr.-Ing. Stephan Theil
Dr.-Ing. David Seelbinder
at Institute of Space Systems, DLR, Germany

Dr. Yves Brière
at ISAE Supaero, France

Bremen, Germany
November 5, 2017

SUMMARY

This thesis describes the design, implementation and simulation process of the attitude control system for DLR's next compact satellite mission S2TEP, which is a three-axis actively stabilized satellite. Based on the requirements arisen during phases A/B, different pointing modes have been established in order to achieve the scientific objectives of this mission.

An analytical estimation of the worst-case disturbance torques is obtained for the whole mission, as well as detailed reconstruction for different fine pointing sub-modes for one orbit. This information was later used for the definition of the minimal requirements in attitude determination and attitude control hardware.

Some controllers are consequently proposed for every pointing mode. First, an enhanced B-dot controller is used to detumble the satellite after the separation from the launcher. Secondly, a spin controller is defined for coarse attitude acquisition during LEOP, and to maintain the satellite in a stable status in case of any failure. Finally, a LQR-based controller is used for the fine pointing manoeuvres.

The mathematical models for the satellite dynamics, actuators, sensor, and environmental models are also derived along this work. At the end, the capabilities of the control system are demonstrated by running some Monte-Carlo simulations under nominal and non-nominal conditions.

CONTENTS

LIST OF FIGURES

LIST OF TABLES

NOTATION

The following mathematical notation is used along this thesis:

VECTORS

Vectors are always given as column matrices

$$\vec{\boldsymbol{v}} = \begin{bmatrix} v_1 \\ v_2 \\ v_3 \end{bmatrix},$$

and they are represented by bold italic letters and an arrow $\vec{\square}$ on top of it. The following nomenclature shall also be taken into account:

$\hat{\boldsymbol{v}}$	Unit vector
$\vec{\boldsymbol{v}}^T$	Transpose of vector $\vec{\boldsymbol{v}}$
$\vec{\boldsymbol{v}}_\alpha$	Vector $\vec{\boldsymbol{v}}$ is representing a characteristic of α
${}^i\vec{\boldsymbol{v}}$	Vector $\vec{\boldsymbol{r}}$ is described in frame i
${}^i\vec{\boldsymbol{r}}_\alpha$	Position of α described in frame i
${}^i\vec{\boldsymbol{v}}_{\alpha/\beta}$	Position of α with respect to β, described in frame i
v_i	i-th element of vector $\vec{\boldsymbol{v}}$
v	Magnitude of vector $\vec{\boldsymbol{v}}$
$\hat{\boldsymbol{e}}$	Eigenvector
$\vec{\mathbf{0}}$	Zeros vector
$\vec{\mathbf{1}}$	Ones vector

MATRICES

The matrices are represented by bold letters, and the following nomenclature is used:

$\mathbf{M}$ or $\mathbf{M}_{n,m}$	Matrix
$\mathbf{M}^{-1}$	Inverse of matrix $\mathbf{M}$
$\mathbf{M}^T$	Transpose of matrix $\mathbf{M}$
$\mathbf{M}_\alpha$	Matrix $\mathbf{M}$ is representing a characteristic of α
${}^i\mathbf{R}_\beta$	Rotation/transformation matrix of β described in frame i
$m_{i,j}$	Element $\mathbf{M}(i,j)$ of matrix $\mathbf{M}$
$\mathbf{I}$	Identity matrix
$\mathbf{0}$	Zeros matrix

QUATERNIONS

The quaternions are represented by bold letters, and the following nomenclature is used:

$\mathbf{q}$	Quaternion
${}^i\mathbf{q}_\beta$	Rotation quaternion from frame β to frame i

q Real part of $\mathbf{q}$
$\vec{\boldsymbol{q}}$ Complex part of $\mathbf{q}$
q_i i-th element of $\mathbf{q}$

REFERENCE FRAMES

A summary of the coordinate reference frames used in this work is shown in Table 1. For Cartesian coordinates, the letter $\mathcal{F}_\alpha$ stands for the frame itself, $\mathcal{O}_\alpha$ is the origin, and the three axes are denoted by $\boldsymbol{X}_\alpha$, $\boldsymbol{Y}_\alpha$ and $\boldsymbol{Z}_\alpha$.

Name	**Short name**	**Index symbol**
Cartesian coordinate frames		
Earth-Centered Inertial frame	ECI, inertial	i
Earth-Centered/Earth-Fixed frame	ECEF, Earth-fixed	e
Orbital frame	orbit	o
Body-Fixed frame	body, satellite	b
Mechanical Coordinate frame	mechanical, structural	m
Principal axes frame	principal	p
Spherical coordinate frames		
Geocentric coordinates	geocentric	gc
Geodetic coordinates	geodetic	gd

Table 1: Coordinate frames summary.

UNITS

All the units presented in this work follow the International System convention, otherwise it will be indicated in the respective section.

List of Symbols

Abbreviations

ADCS	Attitude Determination and Control System
CoAF	Center of Aerodynamic Force
CoG	Center of Gravity
CoM	Center of Mass
CoSP	Center of Solar Pressure
DCM	Director Cosine Matrix
DLR	Deutsches Zentrum für Luft- und Raumfahrt
ECEF	Earth-Centered Earth-Fixed
ECI	Earth-Centered Inertial
EEE	Electrical, Electronic and Electromechanical
EPS	Electrical Power System
FoV	Field of View
GPS	Global Positioning System
GYR	Gyroscope
IOV	In Orbit Validation
IR	Infrared
JD	Julian Date
LEOP	Launch and Early Orbit Phase
LEO	Low Earth Orbit
LQR	Linear Quadratic Regulator
LTAN	Local Time of Ascending Node
MAG	Magnetometer
MEMS	Micro-Electro-Mechanical Systems
MJD	Modified Julian Date
MoI	Moment of Inertia
MTQ	Magnetic Torquer
OBC	On-Board Computer
RAAN	Right Ascension of the Ascending Node
RMS	Root Mean Square
RSS	Residual Sum of Squares
RW	Reaction Wheel

S2TEP Small Satellite Technology Experimental Platform
SRP Solar Radiation Pressure
SSO Sun Synchronous Orbit
SS Sun sensor
STR Star tracker
TCS Thermal Control System

GREEK LETTERS

η Noise
γ Precession angle
λ Geocentric/geodetic longitude
μ Gravitational constant
ν True anomaly
Ω Right ascension of the ascending node
ω Argument of perigee, angular rate
ϕ Roll angle
ϕ_{gc} Geocentric latitude
ψ Yaw angle
ρ Density
θ Pitch angle
Υ_{J2000} Vernal equinox of year 2000
ε Error
φ Geodetic latitude
$\vec{\boldsymbol{\tau}}$, τ Torque

ROMAN LETTERS

a Mean reference spherical radius
A Area
a Semi-major axis
BW Bandwidth
$\vec{\boldsymbol{B}}$, B Magnetic field
b Semi-minor axis
b_m Viscous friction coefficient
c Speed of light in vacuum
c Distance between the center of an ellipse and its main focal point
C_D Drag coefficient
C_d Coefficient of diffuse reflection

C_s	Coefficient of specular reflection
$\vec{\boldsymbol{D}}$, D	Magnetic dipole
e	Eccentricity
e_a	Electromotive force
$\mathcal{F}$	coordinate frame
$\vec{\boldsymbol{f}}$, f	Force
F	Focal point
g_n^m, h_n^m	Gauss coefficients
$\vec{\boldsymbol{H}}$, H	Angular momentum
h	Altitude from the Earth surface
i	Orbit inclination
i_a	Armature current
$\boldsymbol{J}$	Moment of inertia matrix
K_τ	Torque constant
K_v	Voltage constant
L_a	Armature inductance
$\vec{\boldsymbol{m}}$	Position of the North geomagnetic pole
$\mathcal{N}$	Radius of curvature in the prime vertical
$\vec{\boldsymbol{N}}$	Normal vector
$\vec{\boldsymbol{\mathfrak{N}}}$	Nadir vector
N_1	Descending node
N_2	Ascending node
$\mathcal{O}$	Origin of a coordinate frame
P	Electrical power
q_r	Reflectance factor
res	Resolution
$\vec{\boldsymbol{r}}$, r	Position and radius in spherical coordinates
R_a	Armature resistance
$\vec{\boldsymbol{S}}$	Sun vector
S_0	Solar constant
T	Time constant, period
u_a	Armature voltage
$\vec{\boldsymbol{v}}$, v	Orbital velocity
V	Lyapunov function

1

INTRODUCTION

1.1. MISSION DESCRIPTION

The German Aerospace Center (DLR in German) has the objective of building and operating a cost-effective satellite platform to be used as in-orbit demonstration for different scientific and technological payloads, for which several launches are planned from 2019. The name of the mission is *Small Satellite Technology Experimental Platform* or S2TEP (see Fig. 1.1) and it is considered as a microsatellite according the mass criterion classification of Kramer and Cracknell [26].

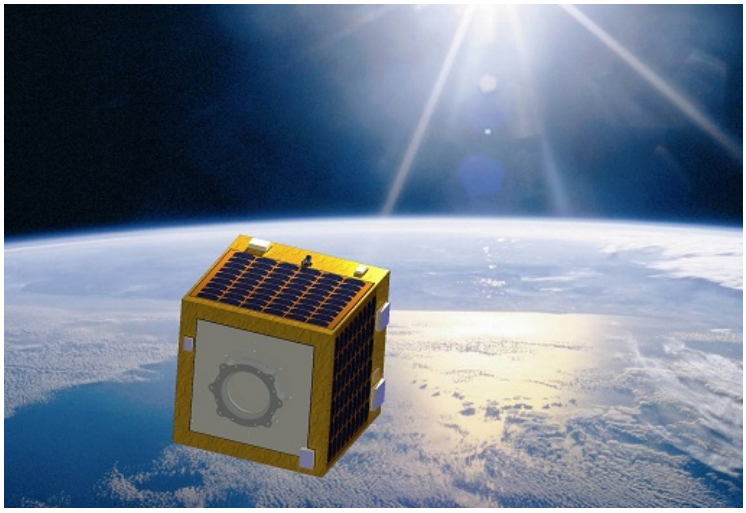

Figure 1.1: S2TEP in orbit (artist's impression).

One of the current design baselines of this platform is the re-usage of DLR's own technology, which is a result of several launches during the previous 10 years. Several hardware and software components will be thus inherited from the previous compact satellite *Eu:CROPIS (Euglena and Combined Regenerative Organic-Food Production in Space)*[18] with the aim of reducing design and integration times. S2TEP also has the heritage from missions like AlSAT [46], MASCOT [16] and AsteroidFinder [17].

This *technology-driven* [4] design approach allows DLR to shorten the development times and to increase the launching frequency, and consequently to provide better operational costs

for the overall mission.

To the date, many payloads are foreseen to be distributed during the different launches of this mission, they are provided by DLR and other external research institutes. For the preliminary design, the following list of payloads [4] was considered:

- **EEE part IOV**: Capacity and performance verification of electrical, electronic and electromechanical parts under space environment conditions.
- **GoSolar**. Proof-test/qualification of large lightweight high-power photovoltaic array technology.
- **InFex**: IR camera (0.09-1.7 μm) to observe spatio-temporal variations on the global atmospheric air-glow layer at 87 km height.
- **ISAoUWB**: Usage of ultra-wide band modules to replace wired intra-satellite communication.
- **JULIA**: Operation of a high-performance optical frequency reference based on Doppler-free spectroscopy on-board a satellite.
- **MITA**: Operation of a MEMS ion thruster for attitude and orbit control and to analyse the chemical composition of the ambient plasma and gas environment.
- **Novel Space Battery System**: Proof-of-concept of a new battery architecture which relies on semiconductors to achieve bus voltage rather than stacking of cells.
- **NoWire**: Usage of three communication modules at different locations within the satellite to demonstrate harness-lees communication.
- **SDRF**: Usage of highly integrated software defined radios for satellite communication.
- **SOLID**: Detection and analysis of space debris impacts using a solar generator.
- **USLP**: Test of a unified space link protocol frame generator

After an analysis of the requirements for the payloads, S2TEP has being foreseen as a three-axis stabilized satellite. It will be allocated on a Sun-synchronous Low Earth Orbit (LEO) within an envelope of 150 km (500 to 650 km). The current baseline design is desired to change as less as possible for future launches, and only critical issues in the design will be solved, if required.

1.2. OBJECTIVE

The objective of this thesis is to analyse, design and simulate the Attitude Determination and Control System (ADCS) for the S2TEP mission using the design requirements arisen in phases A and B of this project.

This main objective will be broken down into some sub-objectives in order to define the structure and direction in which the research will be carried out, they are:

1. The control system shall be easy to be implemented in the OBC.
2. The control system shall be able to provide three-axis active stabilization for the nominal mode (Nadir), and spin stabilization for the safe mode.

4. The control system shall be able to detumble the satellite after the separation from the launcher, or in case the satellite is uncontrollably spinning.

3. The control system shall be robust; this means, the performance shall not be compromised by any change in the environmental conditions (atmosphere, Sun, magnetic field or gravity gradient).

5. The attitude determination shall be accurate enough to cope with the required pointing performance.

In order to study the feasibility of the control system proposed in this work, some relevant question will be formulated aiming to obtain the respective answers along the chapters of this work. These questions are especially useful to highlight some critical design points in the baseline design of this system, they are:

1. *What are the worst environmental conditions that the satellite will face during its mission lifetime, and how much will they affect the ADCS performance?*

2. *What is the minimal hardware configuration that allows the satellite to fulfil its mission?*

3. *Are all the requirements established by the other sub-systems accomplished, and under what conditions?*

4. *What is the maximal allowed uncertainty in some critical parameters of the satellite (moment of inertia, magnetic dipole and center of mass, among others) before the stability of the satellite is compromised?*

5. *What shall be some critical design considerations for phase C in order to maintain the ADCS baseline design presented in this work?*

1.3. RESEARCH METHOLOGY

In order to achieve the proposed objectives, this research will be split up into four main parts.

First of all, the design requirements will be gathered from all the departments working in this mission. Based on that information, the pointing modes will be established and some restrictions in the performance and hardware will be defined.

Secondly, using DLR's proprietary libraries "High Performance Satellite" [55] and "Compact Satellite", the simulation models will be modified and adapted to cope with the characteristics of S2TEP. These libraries include models for the calculation of satellite dynamics, environmental conditions, disturbance torques, actuators and sensors, among others. The models not available within these libraries will be defined and then implemented using a *Matlab-Simulink* environment.

The ADCS baseline structure is presented in Fig. 1.2, where 7 main blocks can be identified from left to right.

- **Guidance**: The attitude references (quaternion and angular rates) will be generated within this block by using the measurements provided by the navigation algorithms. An autonomous switching function which simulates the transitions between modes is also included here.

- **Control**: The set of control algorithms defined for each pointing mode is modelled within this block.

- **Actuators**: This block simulates the dynamics of a triad of reaction wheels, and a triad of magnetic torquers.
- **Satellite dynamics**: Within this block, the attitude and position dynamics is calculated by employing both the Kepler parameters and the satellite characteristics.
- **External disturbances**: Four main sources of external disturbances are modelled within this block aiming to simulate the effects of the space environment on the satellite dynamics: gravity gradient, magnetic field, solar radiation pressure and atmospheric drag.
- **Sensors**: This model simulates the effects produced by each sensor on the measurements (bias, noise and random walk, among others).
- **Navigation**: A Kalman filter used for both states estimation and noise filtering will be simulated in this block. In addition, some useful attitude transformations and other calculations will be also computed here.

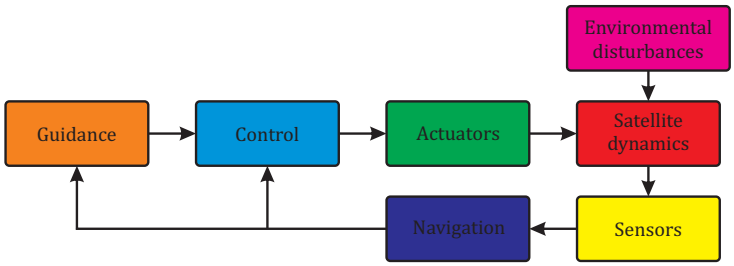

Figure 1.2: Proposed ADCS architecture for the S2TEP mission.

Lastly, a Monte-Carlo analysis will be run for four different simulation scenarios. This campaign allows studying the interaction of the pointing modes with the transitions under nominal and non-nominal conditions, as well as the impact of uncertainties in the ADCS's performance.

1.4. CURRENT STATE OF THE ADCS

The current baseline design is composed of the following attitude determination hardware:

- 1 × Gyroscope *STIM300* by Sensonor, Norway.
- 1 × Magnetometer *AMR digital* by ZARM Technik AG, Germany.
- 6 × Sun sensor *SSOC-D60* by Solar MEMS, Spain.
- 1 × Star tracker *ST-200* by Berlin Space Technologies, Germany.
- 1 × GPS receiver *Phoenix* by DLR, Germany.

and the following attitude control hardware:

- 3 × Reaction wheels *RW3-0.060* by Sinclair Interplanetary, Canada.
- 3 × Magnetic torquers *MT 10-2-H* by ZARM Technik AG, Germany.

as well as the following control laws:

- Enhanced B-dot controller.
- Spin, nutation and precession control.
- Linear Quadratic Regulator with magnetic unloading of the wheels.

1.5. STRUCTURE

This thesis is composed of 7 chapters and 4 appendices:

- **Chapter 2.** The attitude determination and pointing performance requirements are given in this chapter. This includes the definitions and constraints for every ADCS mode.
- **Chapter 3.** The analytical models for the different sources of environmental disturbances are discussed in this chapter. Later on, an accurate estimation of the disturbance torques for the nominal mode is performed, as well as a worst-case scenario calculation that covers all the phases of this mission.
- **Chapter 4.** The sizing of the attitude determination and attitude control hardware is carried out in this chapter, where also the minimal requirements for each hardware component are outlined. In addition, the dynamical models used for the simulation of sensors and actuators are also described.
- **Chapter 5.** This chapter covers the dynamical modelling of the satellite dynamics and some control theory definitions. Subsequently, the final feedback gains used for every pointing mode are given.
- **Chapter 6.** In this chapter, the experimental set-up for the simulations and Monte-Carlo campaign are explained in detail. Some results for the nominal and non-nominal cases are also presented.
- **Chapter 7.** The conclusions, improvements and design considerations for the phase C are discussed at the closure of this thesis.
- **Appendix A.** The mathematical definitions for the correct understanding of the chapters content is outlined in this appendix.
- **Appendix B.** In this appendix, some definitions about orbital mechanics and coordinate frames are summarized.
- **Appendix C.** Some control theory definitions and related analytical stability demonstrations are explained in this appendix.
- **Appendix D.** Extra plots are provided in this chapter with the aim of complementing the results presented in Chapter 6.

2

POINTING MODES AND REQUIREMENTS

A good definition of the pointing modes is not only important for the mission itself, but also for the estimation of the environmental torques and the correct sizing of the ADCS hardware. A detailed explanation of the pointing modes and their requirements is stressed out in this chapter, as well as the minimal hardware configuration that allows the correct operation of the ADCS. Finally, the mathematical formulations for the guidance laws are described for fine pointing mode.

2.1. EARLY-ORBIT MODES

2.1.1. Detumbling Mode (DTM)

This mode is also known as angular momentum dumping and it will be activated right after the separation from the launcher. It is used to reduce the satellite spin rate below 3.6 $\text{deg}\cdot\text{s}^{-1}$, limit that was imposed by the mission analysis and it is directly linked to some restrictions in the electronic components and payloads.

The launcher separation rate is at this moment unknown, and its value will be updated when a launcher provided is selected. From *Eu:CROPIS* [20], a good approximation would be 10 $\text{deg}\cdot\text{s}^{-1}$ in a worst-case scenario. The operational range of the angular rate for this mode is thus

$$2\,\omega_{orbit} \leq \omega_{sat} < 10\,\text{deg}\cdot\text{s}^{-1}. \tag{2.1}$$

For the detumbling phase, only magnetic actuation is required; therefore, the magnitude and direction of the geomagnetic field should be known at any moment so that the calculation of the correction manoeuvres is done in real time. The angular rate is not required for this mode; however, the performance of the controller can be improved if this measurement is available.

2.1.2. Coarse Acquisition Mode (CAM)

This model will be activated after DTM when an angular rate close to zero is detected. During its nominal operation, the satellite will spin-up around its axis with the maximal moment of inertia ($\boldsymbol{Z_b}$-axis for this analysis), and then the angular moment vector $\vec{\boldsymbol{H}}_{sat}$ will be reoriented towards orbit normal (to the Sun) direction for maximal efficiency of the solar array and to avoid overheating of the radiators located at the bottom face [50].

The nominal operation range of this mode is subsequently defined as

$$\begin{aligned} \omega_z &\geq \omega_{CAM_{min}}, \\ \underbrace{\cos^{-1}\left({}^{i}\hat{\boldsymbol{N}}_{orbit}\cdot{}^{i}\hat{\boldsymbol{H}}_{sat}\right)}_{\gamma} &\leq 5\,\text{deg}, \end{aligned} \tag{2.2}$$

where γ denotes the precession angle (angle between the angular momentum vector and the orbit normal vector, described in the inertial frame).

The minimal spinning rate $\omega_{CAM_{min}}$ to achieve stability and to perform precession manoeuvres will be further studied in Chapter 5. From *Eu:CROPIS*, it is known that the reorientation of $\vec{\boldsymbol{H}}_{sat}$ can be achieved with solely magnetic actuation. However, if one (or more) reaction wheels are used, the behaviour of this mode will be positively affected.

Besides the control capabilities, the measurements of the gyroscope together with the Sun vector and the geomagnetic field vector can be fused in a Kalman filter for the calculation of the attitude quaternion. The orbit normal vector is constant for circular orbits when seen from the inertial frame, otherwise its value can be determined on-board using the orbital velocity and position vectors, and the current attitude quaternion.

2.2. NOMINAL MODE (NOM)

Since the constraints for S2TEP's first mission have not been yet completely defined, several useful sub-modes are foreseen as baseline design in order to perform different scientific activities. Every sub-mode uses the same hardware and control laws configuration, the main difference lies in the reference signal generated by the guidance law.

For this mode, both magnetic and RW control will be used given the requirements in pointing accuracy. In addition, the measurements of a star tracker are foreseen in order to fulfil the attitude determination requirements.

2.2.1. Nadir pointing mode (NPM)

In this sub-mode one of the lateral faces of the satellite will point towards the Earth's CoM ($\boldsymbol{X}_{\mathcal{B}}$-axis). The axis with the largest moment of inertia ($\boldsymbol{Z}_{\mathcal{B}}$-axis) will be then parallel to the orbit normal (to the Sun) direction, and the remaining vector ($\boldsymbol{Y}_{\mathcal{B}}$-axis) will form an right-handed orthonormal system.

If the final mission orbit is circular, $\boldsymbol{Y}_{\mathcal{B}}$-axis will be always parallel to the orbital velocity vector, otherwise (elliptical orbits) the cross product between the Nadir vector ${}^{i}\vec{\mathcal{N}}$ and the orbital velocity vector ${}^{i}\vec{\boldsymbol{v}}$ is used to correct deviations, or in other words

- for $i \in [0°, 90°)$:

$$\begin{aligned} \boldsymbol{X}_{ref} &= {}^{i}\vec{\mathcal{N}}, \\ \boldsymbol{Y}_{ref} &= \left({}^{i}\vec{\mathcal{N}} \times {}^{i}\vec{\boldsymbol{v}}\right) \times {}^{i}\vec{\mathcal{N}}, \\ \boldsymbol{Z}_{ref} &= {}^{i}\vec{\mathcal{N}} \times {}^{i}\vec{\boldsymbol{v}}. \end{aligned} \tag{2.3}$$

- for $i \in [90°, 180°)$:

$$\begin{aligned} \boldsymbol{X}_{ref} &= {}^{i}\vec{\mathcal{N}}, \\ \boldsymbol{Y}_{ref} &= -\left({}^{i}\vec{\mathcal{N}} \times {}^{i}\vec{\boldsymbol{v}}\right) \times {}^{i}\vec{\mathcal{N}}, \\ \boldsymbol{Z}_{ref} &= {}^{i}\vec{\mathcal{N}} \times {}^{i}\vec{\boldsymbol{v}}. \end{aligned} \tag{2.4}$$

2.2.2. Sun pointing mode (SPM)

In this sub-mode, the $\boldsymbol{Z}_{\mathcal{B}}$-axis will be aligned with the Sun vector ${}^{i}\vec{\boldsymbol{S}}$ while $\boldsymbol{X}_{\mathcal{B}}$-axis points towards the direction of the orbital velocity vector. The $\boldsymbol{Y}_{\mathcal{B}}$-axis will form a right-handed orthonormal

system. The formal definition of this mode will thus be

$$\begin{aligned} \boldsymbol{X}_{ref} &= \left({}^{i}\vec{\boldsymbol{S}} \times {}^{i}\vec{\boldsymbol{v}}\right) \times {}^{i}\vec{\boldsymbol{S}}, \\ \boldsymbol{Y}_{ref} &= {}^{i}\vec{\boldsymbol{S}} \times {}^{i}\vec{\boldsymbol{v}}, \\ \boldsymbol{Z}_{ref} &= {}^{i}\vec{\boldsymbol{S}}. \end{aligned} \tag{2.5}$$

2.2.3. Inertial pointing mode (IPM)

For inertial pointing, all the axes of the body frame shall be aligned to the ECI coordinated frame (see Section B.5.1), or in other words

$$\begin{aligned} \boldsymbol{X}_{ref} &= \boldsymbol{X}_{i}, \\ \boldsymbol{Y}_{ref} &= \boldsymbol{Y}_{i}, \\ \boldsymbol{Z}_{ref} &= \boldsymbol{Z}_{i}. \end{aligned} \tag{2.6}$$

2.2.4. Ground point tracking (GPT)

Let ${}^{i}\vec{\boldsymbol{p}}$ be the vector representing the position of a point of interest on the Earth's surface, and ${}^{i}\vec{\boldsymbol{r}}$ the vector representing the position of the satellite, both of them measured from the Earth's CoM and described in the inertial frame. If it is assumed that a particular payload is located in satellite's $\boldsymbol{X}_{b}$-axis , the mathematical formulation for this mode will be

$$\begin{aligned} \boldsymbol{X}_{ref} &= {}^{i}\vec{\boldsymbol{p}} - {}^{i}\vec{\boldsymbol{r}}, \\ \boldsymbol{Y}_{ref} &= \left(\left[{}^{i}\vec{\boldsymbol{p}} - {}^{i}\vec{\boldsymbol{r}}\right] \times {}^{i}\vec{\boldsymbol{v}}\right) \times \left({}^{i}\vec{\boldsymbol{p}} - {}^{i}\vec{\boldsymbol{r}}\right), \\ \boldsymbol{Z}_{ref} &= \left({}^{i}\vec{\boldsymbol{p}} - {}^{i}\vec{\boldsymbol{r}}\right) \times {}^{i}\vec{\boldsymbol{v}}. \end{aligned} \tag{2.7}$$

It should be stressed out that this formulation is only valid when the point of interest is in the payload's visual field.

One of the disadvantages of this sub-mode is the fact that ${}^{i}\vec{\boldsymbol{p}}$ is only fixed when seen from the ECEF frame, therefore the rotation between the ECEF and ECI frames shall be either know or calculated at any moment (see Appendix B.5.1). ${}^{e}\vec{\boldsymbol{p}}$ vector can be obtained by using the longitude, latitude and elevation coordinates of the site of interest (e.g. Weilheim) and the transformations of Appendix B.5.2. The difficulty of measuring ${}^{i}\vec{\boldsymbol{p}}$ in real time could be also overcome by adding an Earth horizon sensor to the ADCS hardware.

2.2.5. Guidance loop reference

For this work, the signal generated by the guidance law will be a reference quaternion and an angular rates vector, the reference quaternion can be directly obtained from the formulations presented here-above. For that purpose, a DCM matrix is first constructed using $\boldsymbol{X}_{ref}$, $\boldsymbol{Y}_{ref}$, $\boldsymbol{Z}_{ref}$ and definition A.3 as

$$\begin{bmatrix} \boldsymbol{X}_{b} \\ \boldsymbol{Y}_{b} \\ \boldsymbol{Z}_{b} \end{bmatrix} = \begin{bmatrix} \boldsymbol{X}_{ref_1} & \boldsymbol{Y}_{ref_1} & \boldsymbol{Z}_{ref_3} \\ \boldsymbol{X}_{ref_2} & \boldsymbol{Y}_{ref_2} & \boldsymbol{Z}_{ref_3} \\ \boldsymbol{X}_{ref_3} & \boldsymbol{Y}_{ref_3} & \boldsymbol{Z}_{ref_3} \end{bmatrix} = {}^{b}\mathbf{R}_{i} \begin{bmatrix} \boldsymbol{X}_{i} \\ \boldsymbol{Y}_{i} \\ \boldsymbol{Z}_{i} \end{bmatrix}, \tag{2.8}$$

and then it is mapped into a quaternion using the procedure described in Section A.3. This new quaternion represents the orientation of the body frame with respect to the inertial frame (or also converts vectors from the inertial to the body frame) and will be used as reference for the control loop.

2.3. SAFE MODE (SFM)

The purpose of this mode is a fast battery re-charging while the satellite is kept in a stable status in case of any failure, this means, only essential subsystems will be activated for power saving. Basically, CAM is a specific case of SFM since the hardware and control algorithms configuration are the same.

The angular momentum stored in the RWs should be taken into account as part of the inputs for this mode, in case a transition from NOM is triggered. This means, the initial angular rate of the RWs should be slowly decreased in order not to start tumbling. If a failure occurs and the satellite tumbles, this mode should also be able to de-spin the satellite before stabilizing it again. The operation range for this mode is therefore repeated from CAM as

$$\begin{aligned} \omega_z &\geq \omega_{CAM_{min}}, \\ \underbrace{\cos^{-1}\left({}^{i}\hat{\boldsymbol{N}}_{orbit} \cdot {}^{i}\hat{\boldsymbol{H}}_{sat}\right)}_{\gamma} &\leq 5 \text{ deg}. \end{aligned} \tag{2.9}$$

All the requirements for the previous modes are summarized in Tables 2.1 and 2.2. The first table contains the input/exit conditions for the autonomous transitions, as well as the maximal allowed error ε for the attitude control and the minimal Δ provided by the attitude determination in order to achieve the required pointing performance. The second table describes the attitude control and attitude determination hardware for each mode.

Mode	**Entry conditions**	**Attitude knowledge**	**Control accuracy**	**Exit conditions**
DTM	$\omega_{sat} < 10 \text{ deg} \cdot s^{-1}$	$\Delta\omega \leq 0.01 \text{ deg} \cdot \text{s}^{-1}$	$\varepsilon_{\omega_{sat}} \leq 0.2 \text{ deg} \cdot \text{s}^{-1}$	$\omega_{sat} \approx \omega_{orbit}$ $\varepsilon_{\omega_{sat}} \leq 0.1 \text{ deg} \cdot \text{s}^{-1}$
CAM	$\omega_{sat} \leq 0.2 \text{ deg} \cdot \text{s}^{-1}$	$\Delta\omega \leq 0.01 \text{ deg} \cdot \text{s}^{-1}$ $\Delta\gamma \leq 0.5 \text{ deg}$	$\varepsilon_{\omega_{sat}} \leq 0.1 \text{ deg} \cdot \text{s}^{-1}$ $\gamma \leq 5 \text{ deg}$	$\varepsilon_{\omega_{sat}} \leq 0.1 \text{ deg} \cdot \text{s}^{-1}$ $\gamma \leq 5 \text{ deg}$ $\omega_{sat} \approx \omega_{CAM}$
NOM	$\omega_{sat} \leq 1 \text{ deg} \cdot \text{s}^{-1}$	$\Delta\phi \leq 0.1 \text{ deg}$ $\Delta\theta \leq 0.1 \text{ deg}$ $\Delta\psi \leq 0.1 \text{ deg}$ $\Delta\omega \leq 0.2\,\omega_{orbit}$	$\varepsilon_{\phi} \leq 1 \text{ deg}$ $\varepsilon_{\theta} \leq 1 \text{ deg}$ $\varepsilon_{\psi} \leq 1 \text{ deg}$ $\varepsilon_{\omega_{sat}} \leq 2\,\omega_{orbit}$	$\varepsilon_{\phi} \leq 1 \text{ deg}$ $\varepsilon_{\theta} \leq 1 \text{ deg}$ $\varepsilon_{\psi} \leq 1 \text{ deg}$ $\varepsilon_{\omega_{sat}} \leq 2\,\omega_{orbit}$
SFM	$\omega_{sat} < 10 \text{ deg} \cdot s^{-1}$	$\Delta\omega \leq 0.01 \text{ deg} \cdot \text{s}^{-1}$ $\Delta\gamma \leq 0.5 \text{ deg}$	$\varepsilon_{\omega_{sat}} \leq 0.1 \text{ deg} \cdot \text{s}^{-1}$ $\gamma \leq 5 \text{ deg}$	$\varepsilon_{\omega_{sat}} \leq 0.1 \text{ deg} \cdot \text{s}^{-1}$ $\gamma \leq 5 \text{ deg}$ $\omega_{sat} \approx \omega_{CAM}$

Table 2.1: Requirements and specifications for the ADCS modes.

Diagram 2.1 shows the available modes for S2TEP, as well as the possible transitions that can be triggered. It must be remarked that the autonomous transitions will be further studied in Chapter 5 using Monte-Carlo simulations.

*Not required, but, if added, the performance of the ADCS will be improved.

†Not taken into account in the first analysis, but, if the orbit normal vector is calculated on-board, it should be included in the final requirements.

Modes	Sensors					Actuators	
	GYR	MAG	SS	GPS	STR	RW	MTQ
DTM	*	×					×
CAM	×	×	×	†		*	×
NOM	×	×	×	×	×	×	×
SFM	×	×	×	×			×

Table 2.2: Minimal hardware configuration

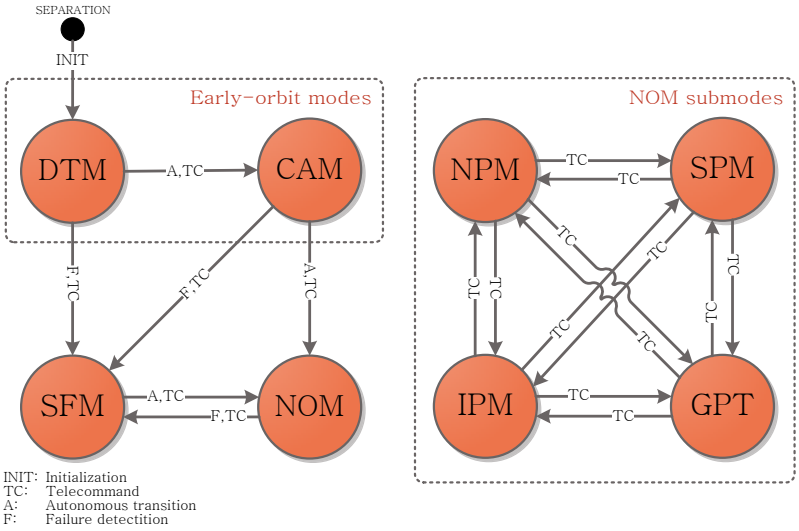

Figure 2.1: S2TEP ADCS modes

3

DISTURBANCE ANALYSIS

In this chapter, the environmental models used in the early design phase are described; these mathematical models were employed for the calculation of the disturbance torques given different sets of initial conditions, as well as different orbital and satellite parameters. The results were analysed in order to obtain the worst-case scenario disturbance torque, which will be used in the next chapter for hardware sizing purposes.

3.1. EXTERNAL DISTURBANCES

Any satellite orbiting the Earth is subject to some disturbance forces and torques, its magnitude and direction mainly depends on different physical parameters like shape, material, mass and environmental conditions, among others.

There are four main sources of disturbance that shall be taken into account when sizing the ADCS hardware: gravity gradient, atmosphere density, geomagnetic field and solar radiation. For LEO, the atmospheric and magnetic disturbances have the largest impact in terms of torque [51].

An on-ground reconstruction of the disturbance torques will be presented in the following sections, where the analytical estimation models depending on the position and orbital velocity will be obtained, as well as a more generic calculation which allows obtaining the maximal expected value not only for NOM, but also for the other modes.

3.1.1. Gravity gradient

The gravity gradient torque is produced by the variation of the Earth's gravitational force on the structure of the satellite; this effect has a bigger impact in satellites with non-symmetric shapes.

The gravity gradient torque is defined by Wertz [51] and NASA [35] as

$$\begin{aligned} {}^{b}\vec{\boldsymbol{\tau}}_{gg} &= \frac{3\,\mu_{earth}}{|{}^{b}\vec{\boldsymbol{r}}|^3}\left[{}^{b}\hat{\boldsymbol{r}} \times \left(\boldsymbol{J}_{sat}\cdot {}^{b}\hat{\boldsymbol{r}}\right)\right], \\ &= \frac{3\,\mu_{earth}}{|{}^{b}\vec{\boldsymbol{r}}|^5}\left[{}^{b}\vec{\boldsymbol{r}} \times \left(\boldsymbol{J}_{sat}\cdot {}^{b}\vec{\boldsymbol{r}}\right)\right], \end{aligned} \tag{3.1}$$

where ${}^{b}\vec{\boldsymbol{r}}$ is the position of the satellite's CoM with respect to Earth's CoM; represented in the body frame. $\boldsymbol{J}_{sat}$ is the moment of inertia matrix and μ_{earth} (3.9860×10^{14} $\mathrm{m}^3 \cdot \mathrm{s}^{-2}$) the Earth's gravitational constant.

Worst-case scenario

The maximal gravity gradient torque [52] can be thus simplified from equation 3.1 as

$$\tau_{gg_{max}} = \frac{3\,\mu_{earth}}{2\,{r_{orbit}}^3}\left(\boldsymbol{J}_{sat_{max}} - \boldsymbol{J}_{sat_{min}}\right)\sin(2\theta)\,, \tag{3.2}$$

where θ is the maximal deviation of the $\boldsymbol{Z}_{\mathcal{B}}$ axis from its local vertical; $\boldsymbol{J}_{sat_{max}}$ and $\boldsymbol{J}_{sat_{min}}$ are, respectively, the maximal and minimal moment of inertia; and r_{orbit} is called orbital radius which value is computed from the equatorial radius and the minimal altitude as

$$r_{orbit} = r_{earth} + h_{min}\,. \tag{3.3}$$

The evaluation of the following parameters:

$$\begin{aligned}
\boldsymbol{J}_{sat_{max}} &= 2.957\ \mathrm{kg\cdot m^2}\,,\\
\boldsymbol{J}_{sat_{min}} &= 2.899\ \mathrm{kg\cdot m^2}\,,\\
r_{earth} &= 6378.137\ \mathrm{km}\,,\\
h_{min} &= 500\ \mathrm{km}\,,\\
\theta &= 45^\circ\,,
\end{aligned}$$

resulted in a maximal torque of

$$\tau_{gg_{max}} = 1.0657\times10^{-7}\ \mathrm{N\cdot m}\,.$$

3.1.2. Geomagnetic field

The mathematical model of the geomagnetic field is defined by Wertz [51] as

$${}^{e}\vec{\boldsymbol{B}}_{earth} = \frac{a^3 H_0}{|{}^{e}\vec{\boldsymbol{r}}|^3}\left[3\,({}^{e}\hat{\boldsymbol{m}}\cdot{}^{e}\hat{\boldsymbol{r}})\,{}^{e}\hat{\boldsymbol{r}} - {}^{e}\hat{\boldsymbol{m}}\right], \tag{3.4}$$

where ${}^{e}\vec{\boldsymbol{r}}$ is the position of the satellite in the ECEF frame, ${}^{e}\hat{\boldsymbol{m}}$ is the normal vector representing the position of the north geomagnetic pole (this value is updated every 5 years by the International Association of Geomagnetism and Aeronomy (IAGA)[49]), the term $a^3 H_0$ denotes the strength of the geomagnetic moment, a (6371.2 km) is the mean reference spherical radius of the Earth, and

$$H_0 = \sqrt{\left(g_1^0\right)^2 + \left(g_2^1\right)^2 + \left(h_1^1\right)^2}, \tag{3.5}$$

where g_n^m and h_n^m are called Gauss coefficients and the most recent value found in [49] is:

$$\begin{aligned}
g_1^0 &= -29442\times10^{-9}\ \mathrm{T}\,,\\
g_1^1 &= -1501\times10^{-9}\ \mathrm{T}\,,\\
h_1^1 &= 4797.1\times10^{-9}\ \mathrm{T}\,.
\end{aligned}$$

The evaluation of previous parameters in equation 3.5 leads to an average geomagnetic moment of

$$a^3 H_0 = 7.724\times10^{15}\ \mathrm{T\cdot m^3}\,.$$

The magnetic disturbance torque is generated by the interaction between the Earth's magnetic field and any other magnetic field produced inside the satellite. There are three main phenomena that contribute to the generation of magnetic torques: Eddy currents, hysteresis and the magnetic dipole of the satellite's structure. In terms of magnitude, the torque generated by the Eddy currents and the hysteresis is negligible when compared to the one produced by the structure [34].

The computation of the total magnetic disturbance torque is hence performed using

$$^{b}\vec{\boldsymbol{\tau}}_{mag} = \vec{\boldsymbol{D}}_{sat} \times {}^{b}\vec{\boldsymbol{B}}_{earth}, \tag{3.6}$$

where $\vec{\boldsymbol{D}}_{sat}$ is the satellite's magnetic dipole and ${}^{b}\vec{\boldsymbol{B}}_{earth}$ is the Earth's magnetic field represented in the body frame [51].

Worst-case scenario

The maximal magnetic torque [52] can be simplified from equation 3.6, as

$$\tau_{mag_{max}} = D_{sat}\, B_{earth_{max}}, \tag{3.7}$$

where the maximal Earth's magnetic field is obtained from a simplification of equation 3.4 for an inclination of 90° (polar orbit), as

$$B_{earth_{max}} = \frac{2\, a^3 H_0}{{r_{orbit}}^3}. \tag{3.8}$$

For S2TEP, there is no further information about the magnetic dipole at the moment, therefore a maximal value of

$$\vec{\boldsymbol{D}}_{sat} = \begin{bmatrix} \frac{1}{\sqrt{3}} & \frac{1}{\sqrt{3}} & \frac{1}{\sqrt{3}} \end{bmatrix}^T \text{ A}\cdot\text{m}^2, \quad \text{or} \quad D_{sat} = 1 \text{ A}\cdot\text{m}^2,$$

is considered for this design.

The substitution of

$$\begin{aligned} a^3 H_0 &= 7.724 \times 10^{15} \text{ T}\cdot\text{m}^3, \\ r_{earth} &= 6\,378.137 \text{ km}, \\ h_{min} &= 500 \text{ km}, \end{aligned}$$

yields to a maximal magnetic dipole torque of

$$\tau_{mag_{max}} = 4.7477 \times 10^{-5} \text{ N}\cdot\text{m}.$$

3.1.3. Solar radiation pressure

The solar radiation impacting on the surface of the satellite produces a force on the faces that are pointing towards the Sun, these forces will generate a torque around the satellite's CoM. In the particular case of the S2TEP satellite, the structure has a prismatic configuration; therefore, Wertz [51] has proposed a model to compute the SRP force generated in each of the plane surfaces of the satellite as

$$\vec{\boldsymbol{f}}_i = -\frac{S_0}{c}\left[(1 - C_s)\,\hat{\boldsymbol{S}} + 2\left(C_s \cos\alpha + \frac{1}{3}C_d\right)\hat{\boldsymbol{N}}\right]\cos\alpha A_i, \tag{3.9}$$

where:

- S_0 is the solar constant (1 358 $\text{W}\cdot\text{m}^2$),
- c is the speed of light in vacuum (299 792 458 $\text{m}\cdot\text{s}^{-1}$),
- C_s is the coefficient of specular reflection,
- C_d is the coefficient of diffuse reflection,
- $\hat{\boldsymbol{S}}$ is the unit vector from the satellite to the Sun,
- $\hat{\boldsymbol{N}}$ is the outwards normal vector to A_i,

- α is the angle between $\hat{\boldsymbol{S}}$ and $\hat{\boldsymbol{N}}$,
- A_i is the area of the analysed surface.

Hence, the total solar force is

$$\vec{\boldsymbol{f}}_{srp} = \sum_{i=1}^{n} \vec{\boldsymbol{f}}_i, \tag{3.10}$$

and the total torque generated by this force will be

$$\vec{\boldsymbol{\tau}}_{srp} = \sum_{i=1}^{n} \vec{\boldsymbol{r}}_{face_i} \times \vec{\boldsymbol{f}}_i, \tag{3.11}$$

where $\vec{\boldsymbol{r}}_{face_i}$ is the vector from the satellite CoM to the CoSP of the i-th surface and n defines the number faces of the satellite [36].

The disturbance force generated by the Albedo effect (solar radiation reflected by the Earth) is not taken into account in this analysis since its magnitude is assumed to be small when compared to the SRP. It is true that in some cases this effect can have a significant negative effect in the satellite; however, enough margin is provided in next section for the calculation of the worst-case scenario conditions.

Worst-case scenario

Following the same procedure, the maximal SRP torque [52] is inferred from equation 3.9 and 3.11, as

$$\tau_{srp_{max}} = \frac{S_0}{c}\, A_s(1+q_r)\, \cos\alpha\, \left(d_{CoSP} - CoM\right), \tag{3.12}$$

where q_r is called the reflectance factor (ranging from 0 to 1), A_s is the exposed surface area, and d_{CoSP} is the location of center of solar pressure.

For the evaluation

$$\begin{aligned} A_s &= 0.36\,\mathrm{m}^2, \\ q_r &= 1, \\ \alpha &= 0^\circ, \\ d_{CoSP} - CoM &= 0.3 - 0.219 = 0.081\,\mathrm{m}, \end{aligned}$$

results in

$$\tau_{srp_{max}} = 2.6418 \times 10^{-7}\ \mathrm{N\cdot m}.$$

3.1.4. Atmospheric drag

The effect of the atmospheric drag is especially important for LEO since its magnitude exponentially increases as h decreases. The drag force acts in the opposite direction of the orbital velocity direction, and for very long missions it decreases the altitude of the satellite.

The evolution of the atmospheric drag [51, 33] is modelled by using

$$\vec{\boldsymbol{f}}_i = -\frac{1}{2}\, C_D\, \rho\, |\vec{\boldsymbol{v}}|^2 \left(\hat{\boldsymbol{N}} \cdot \hat{\boldsymbol{v}}\right) \hat{\boldsymbol{v}}\, A_i\,, \tag{3.13}$$

where:

- ρ is the atmospheric density,
- C_D is the drag coefficient,

- $\vec{\boldsymbol{v}}$ is the orbital velocity vector,
- $\hat{\boldsymbol{N}}$ is the outwards normal vector to A_i,
- A_i is the area of the analysed surface.

Thus, the total atmospheric force is

$$\vec{\boldsymbol{f}}_{atm} = \sum_{i=1}^{n} \vec{\boldsymbol{f}}_i \,, \tag{3.14}$$

and consequently the total torque produced by this force is

$$\vec{\boldsymbol{\tau}}_{atm} = \sum_{i=1}^{n} \vec{\boldsymbol{r}}_{face_i} \times \vec{\boldsymbol{f}}_i \,. \tag{3.15}$$

Worst-case scenario

Finally, the maximal atmospheric torque [52] can be obtained from equations 3.13 and 3.15, as

$$\tau_{atm_{max}} = \frac{1}{2} C_D \, \rho \, A_s \, v^2 \, (d_{CoAF} - CoM) \, \frac{3}{\sqrt{2}} \,, \tag{3.16}$$

where d_{CoAF} is the location of the center of atmospheric force and v is the orbital velocity for the given altitude.

It must be pointed out that since the value of C_D is not yet defined, Wertz and Larson [52] have proposed a table with typical drag coefficients for different missions launched in previous years, where it is observed that C_D usually varies between 1 and 4.

The value of atmospheric density ρ will depend on the altitude and the solar activity; for this reason, the JB2006 atmospheric model is used for the estimation of this parameter [11]. In this model, the value of the atmospheric density is given for different solar activity values (low, moderate, high low-term and high short-term). A simulation using these different values of atmospheric density and drag coefficient was carried out using equation 3.16 for different altitudes, the results are depicted in Fig. 3.1.

For the sizing procedure, only one value of drag coefficient and atmospheric density should be selected for the computation of the maximal disturbing torque. Fig. 3.2 shows the evolution of the solar activity in the previous 50 years, where it is observed that the Sun activity follows a cycle of eleven years. And since S2TEP's first launch is planned for 2019 (even if it is likely to face low solar activity) the sizing procedure will be done for long-term high solar activity to guarantee a safety margin for future missions.

The selected values for the estimation of the maximal atmospheric are thus

$$\begin{aligned} A_s &= 0.36 \ \mathrm{m}^2 \,, \\ C_D &= 2.5 \,, \\ \rho &= 3.04 \times 10^{-12} \ \mathrm{kg \cdot m^3} \,, \\ v &= 7.6126 \ \mathrm{km \cdot s^{-1}} \quad \text{(for 500 km)} \,, \\ d_{CoAF} - CoM &= 0.3 - 0.219 = 0.081 \ \mathrm{m} \,, \end{aligned}$$

which yields to

$$\tau_{atm_{max}} = 1.3622 \times 10^{-5} \ \mathrm{N \cdot m} \,.$$

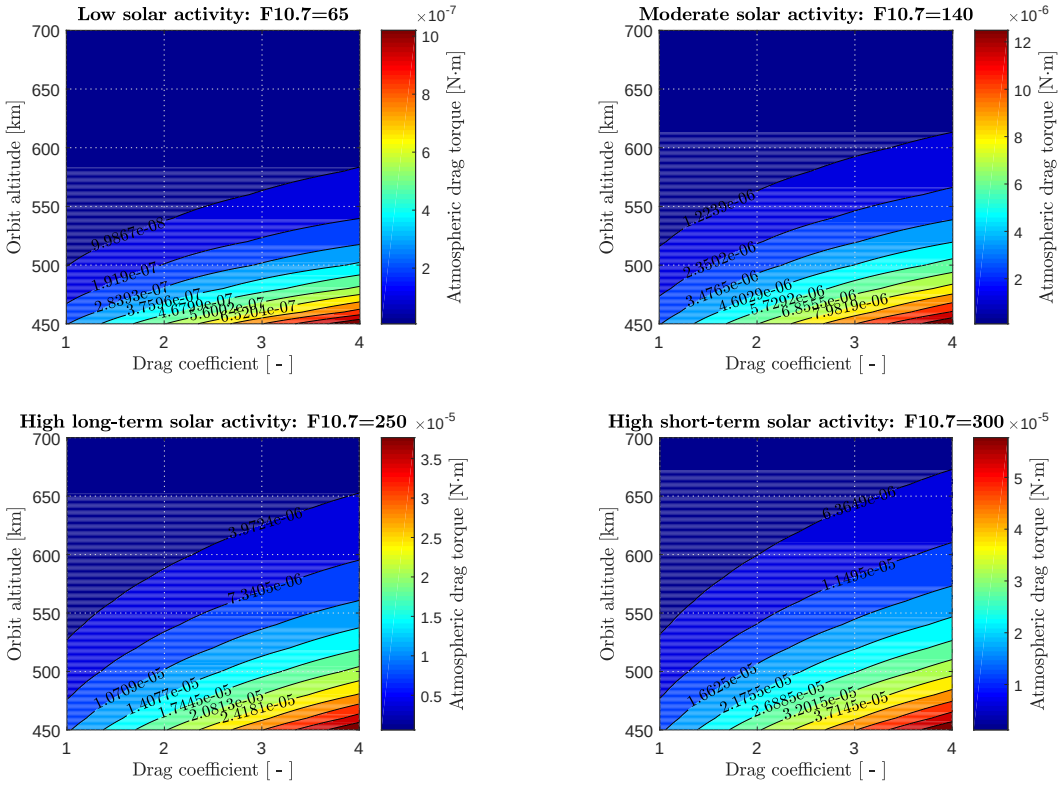

Figure 3.1: Evolution of the atmospheric torque in terms of h, C_D and the solar activity.

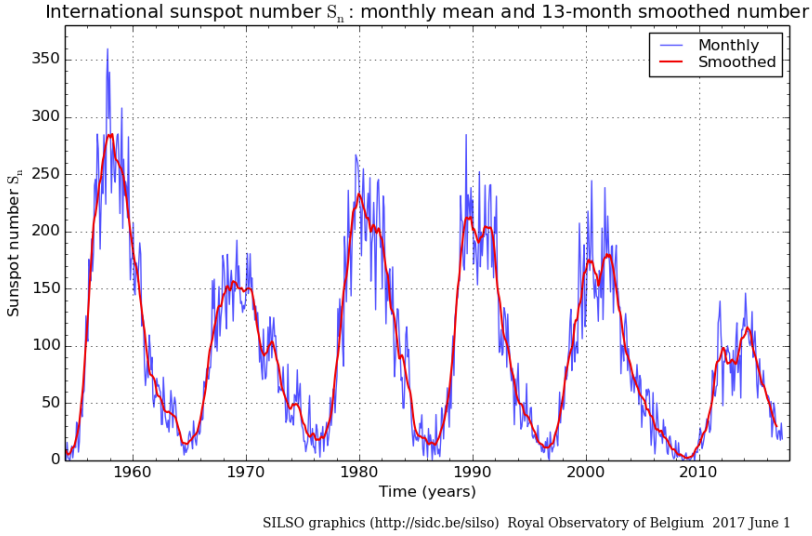

Figure 3.2: Solar activity for the last 50 years [38]

3.2. INTERNAL DISTURBANCES

For S2TEP, only external disturbances are taken into account for the hardware sizing procedure since the satellite, at the moment, does not have flexible appendages, fuel tanks, or propulsive elements for orbital manoeuvres.

If in the future any of these effects needs to be analysed, there will be a block within the simulator where they can be added.

3.3. ANALYSIS OF DISTURBANCES FOR NOM

As pointed out in previous section, one of the parameters that influences the magnitude of the disturbance torques is the orbit. An analysis taking into account different altitudes was carried out in order to obtain the evolution of the disturbance torques and the angular momentum for NOM during one orbital period. This analysis is particularly interesting since it allows to study how the angular momentum accumulates for one orbit.

The data presented in Table 3.1 was provided by the mission analysis team, and it shows the orbit envelope which will be used for the estimation of the disturbances.

Orbit parameter	**Constraint**
Orbit class	LEO
Orbit type	SSO
LTAN [hh:mm]	Negotiable (close to 6:00 h or 10:30 h)
Perigee [km]	Negotiable (from 500 to 650 km)
Apogee [km]	Negotiable (from 500 to 650 km)
Inclination [deg]	SSO (> 51°: Weilheim ground station)
Argument of perigee [deg]	No constraints
Eccentricity	No constraints

Table 3.1: Mission orbit envelope.

From Section 2.2, three sub-modes of NOM were selected to analyse the evolution of the disturbances: NPM, SPM and IPM. In Table 3.2, six simulation scenarios with different orbital parameters and different initial conditions are defined based on the envelop from Table 3.1. For each sub-mode, two simulation scenarios were defined: a worst-case scenario (min. altitude) and a relaxed-conditions scenario (max. altitude).

Case	**Pointing mode**	**Initial quaternion**	**Rotation XYZ [deg]**	**Altitude [km]**	**LTAN [hh:mm]**	**Solar activity**
1	NPM	$[0 \quad 0 \quad 0 \quad 1]^T$	$[0 \quad 0 \quad 0]^T$	500	06:00	high
2	NPM	$[0 \quad 0 \quad 0 \quad 1]^T$	$[0 \quad 0 \quad 0]^T$	650	10:30	low
3	SPM	$[0 \quad 0 \quad 0 \quad 1]^T$	$[0 \quad 0 \quad 0]^T$	500	06:00	high
4	SPM	$[0 \quad 0 \quad 0 \quad 1]^T$	$[0 \quad 0 \quad 0]^T$	650	10:30	low
5	IPM	$[0 \quad 0 \quad 0 \quad 1]^T$	$[0 \quad 0 \quad 0]^T$	500	06:00	high
6	IPM	$[0 \quad 0 \quad 0 \quad 1]^T$	$[0 \quad 0 \quad 0]^T$	650	10:30	low

Table 3.2: Simulation conditions for the nominal mode.

Simulation cases

The results from the evaluation of the simulation cases of Table 3.2 using model 6.1 are presented in the following section:

Nadir pointing

Parameters	h [km]	e [deg]	ω [deg]	i[deg]	Ω [deg]	ν [deg]	ρ [kg $\cdot$ m^{-3}] [11]
Worst-case	500	0°	0°	97.40°	270°	0°	3.04×10^{-12}
Relaxed case	650	0°	0°	97.98°	337.5°	0°	7.410×10^{-15}

Table 3.3: Simulation scenarios for Nadir pointing.

For NPM, the gravity gradient torque is zero in every axis, this result is only valid for this mode since vector ${}^{b}\vec{r}$ is always constant at any point in the orbit. In addition, as $\boldsymbol{X}_b$-axis is always oriented towards the Earth, the position vector has only one component, which means, the cross product of this vector with itself will be equal to zero (see equation 3.1).

For the torque generated by the geomagnetic field, its value shall be larger or smaller when the satellite is closer to the poles or the equator, respectively. The non-constant distribution of the geomagnetic field around the Earth generates a disturbance torque in every axis of the body frame. Furthermore, if the magnetic dipole $\vec{\boldsymbol{D}}_{sat}$ is concentrated in only one axis (e.g. $\vec{\boldsymbol{D}}_{sat} = \begin{bmatrix}1 & 0 & 0\end{bmatrix}$), only a disturbance torque will be generated in two axes (for previous example: $\boldsymbol{Y}_b$- and $\boldsymbol{Z}_b$-axes) after cross product of equation 3.6 is applied.

The atmospheric drag torque is only noticeable in $\boldsymbol{X}_b$-axis for NPM, this is due to the alignment between the drag force and the velocity vector. The drag generates a parallel force to $\boldsymbol{Y}_b$-axis and therefore a torque around $\boldsymbol{X}_b$-axis, as seen in the results.

The SRP torque affects only two axes of the body frame. The direction of the Sun vector changes according to the position on the orbit, therefore a force is generated in every axis. However, since $\boldsymbol{Z}_b$-axis is located exactly at the center of the face, no torques will be generated around this axis.

Sun pointing mode

Parameters	h [km]	e [deg]	ω [deg]	i [deg]	Ω [deg]	ν [deg]	ρ [kg $\cdot$ m^{-3}] [11]
Worst-case	500	0°	0°	97.40°	270°	0°	3.04×10^{-12}
Relaxed case	650	0°	0°	97.98°	375°	0°	7.410×10^{-15}

Table 3.4: Simulation scenarios for Sun pointing.

For SPM, the results are depicted in Figs. 3.5 and 3.6, the position of the $\boldsymbol{X}_b$-axis was fixed in parallel direction to the velocity vector, while $\boldsymbol{Z}_b$-axis was aligned with the Sun vector. In both cases the gravity gradient torque affects only two axes of the body frame; this result is valid given that the moment of inertial around $\boldsymbol{X}_b$- and $\boldsymbol{Y}_b$-axes are equal, therefore the cross product will be cancelled in $\boldsymbol{Z}_b$-axis.

The resulting magnetic torques have the same behaviour as for Nadir pointing.

For this mode, there are no torques generated by the SRP since the Sun vector is always parallel to $\boldsymbol{Z}_b$-axis. Therefore, torques around $\boldsymbol{X}_b$- and $\boldsymbol{Y}_b$-axes cancel each other.

For the atmospheric drag, the velocity vector is always contained inside plane $\mathbf{X}_b - \mathbf{Y}_b$; there-

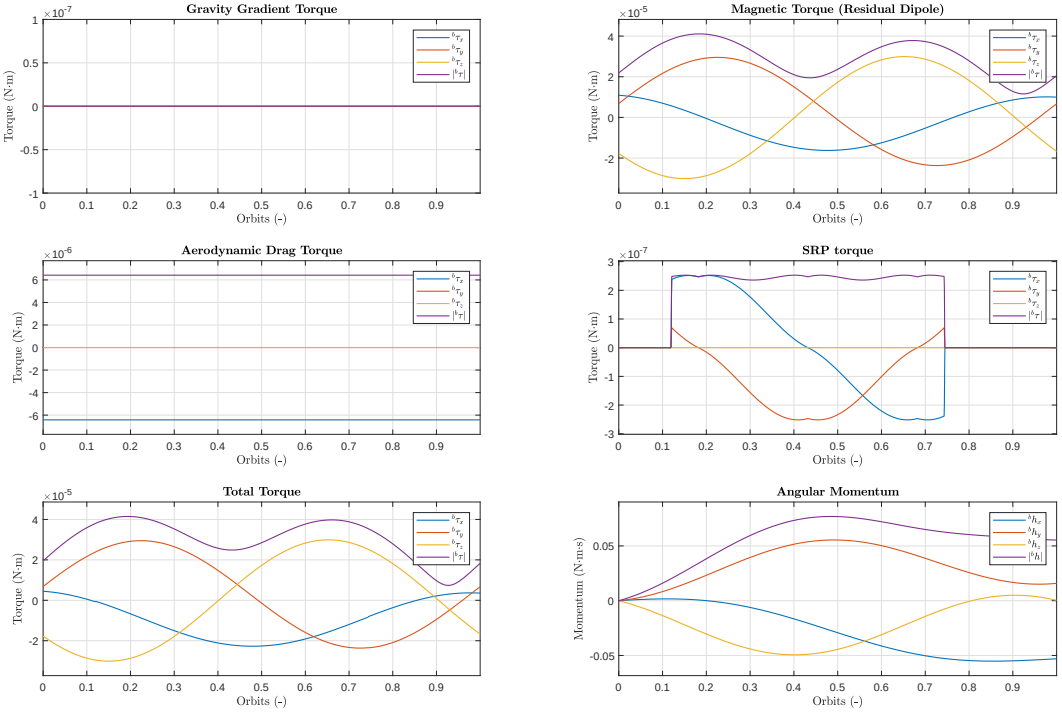

Figure 3.3: Evolution of the torques for Nadir pointing (worst case scenario).

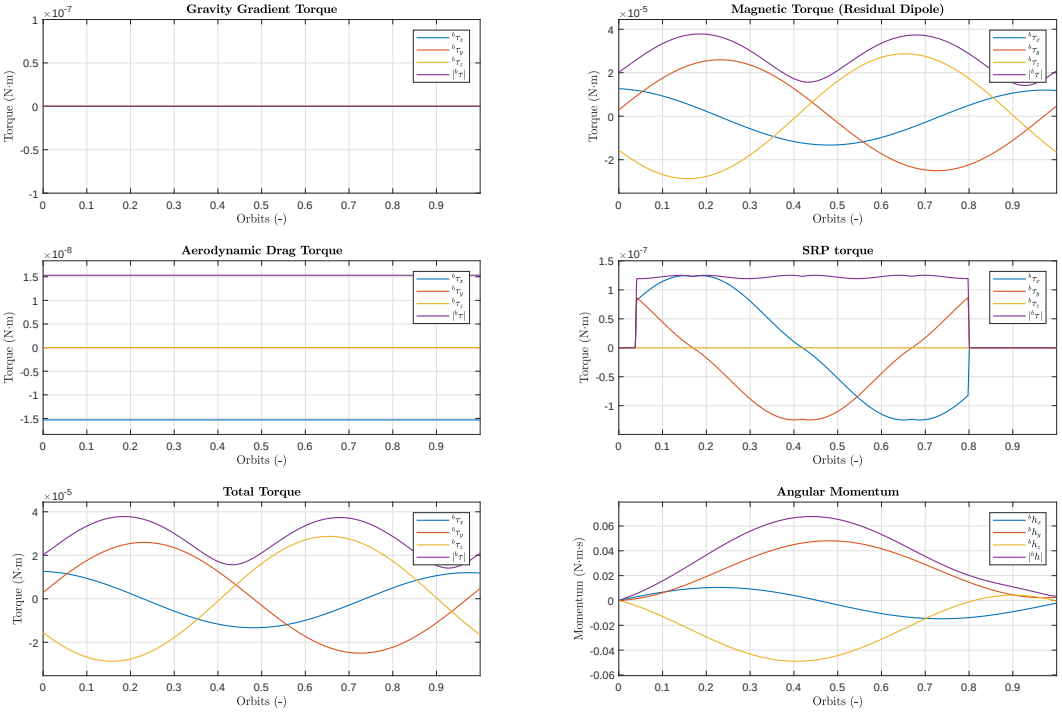

Figure 3.4: Evolution of the torques for Nadir pointing (relaxed conditions).

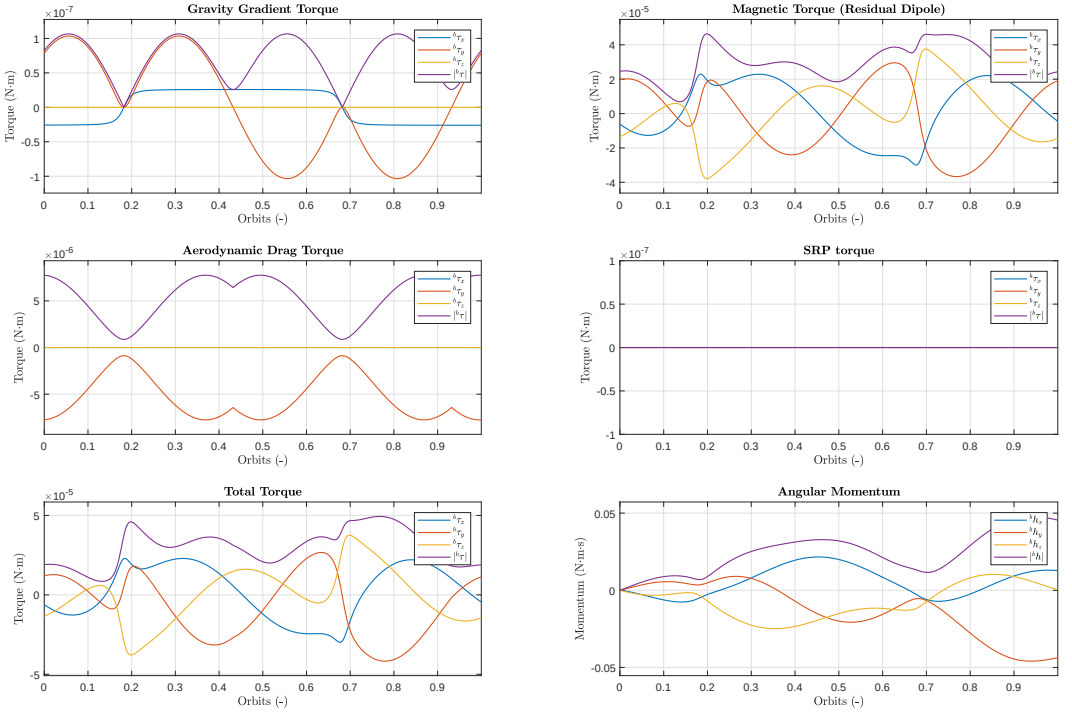

Figure 3.5: Evolution of the torques for Sun pointing (worst case scenario).

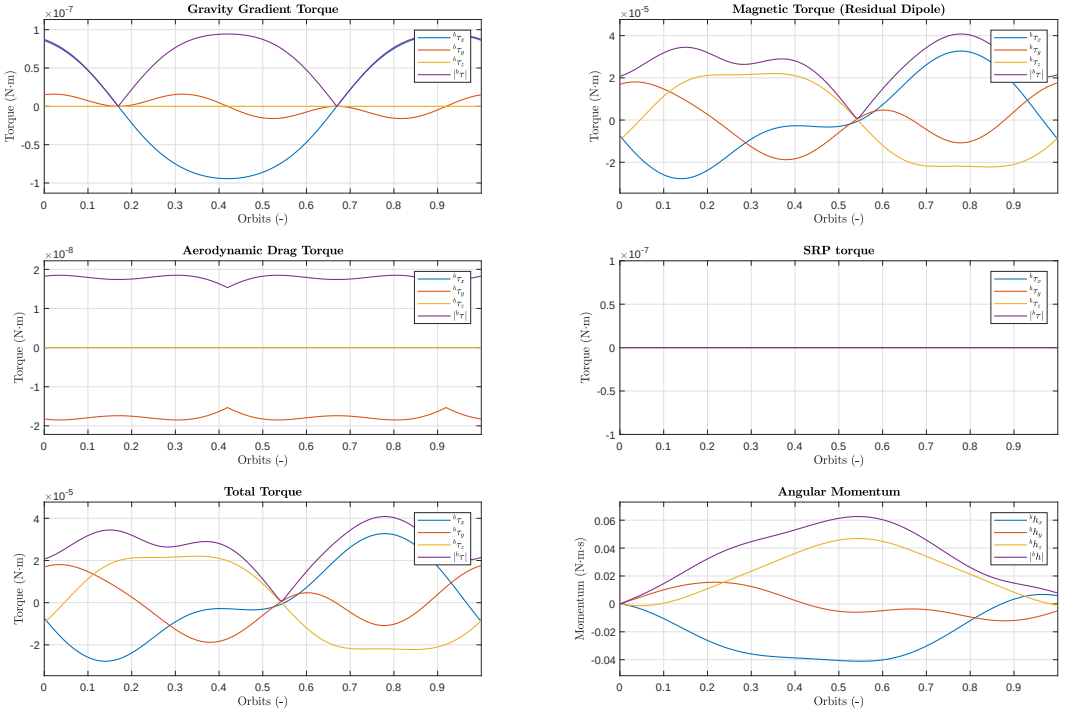

Figure 3.6: Evolution of the torques for Sun pointing (relaxed conditions).

fore, the drag force will only generate a torque around $\boldsymbol{Y}_b$-axis since $\boldsymbol{X}_b$-axis origin is shifted from the geometrical center of the cube.

Inertial pointing mode

Parameters	h [km]	e [deg]	ω [deg]	i [deg]	Ω [deg]	ν [deg]	ρ [kg $\cdot$ m^{-3}] [11]
Worst-case	500	0°	0°	97.40°	270°	0°	3.04×10^{-12}
Relaxed case	650	0°	0°	97.98°	375°	0°	7.410×10^{-15}

Table 3.5: Simulation scenarios for inertial pointing.

For inertial pointing mode, the resulting gravity gradient torque has the same behaviour as the one presented for Sun pointing mode, whereas the magnetic torque has the same behaviour as for Nadir pointing mode.

The SRP torque is always constant since the body frame is fixed in inertial space and the direction of the Sun vector does not change for one orbital period.

For the atmospheric drag torque, the orbital velocity vector rotates around the origin of the body frame; therefore, the resulting total force can have any direction. With respect to the CoM, this force will only create a torque in $\boldsymbol{X}_b$- and $\boldsymbol{Y}_b$-axes since the perpendicular components to planes $\mathbf{X}_b - \mathbf{Z}_b$ and $\mathbf{Y}_b - \mathbf{Z}_b$ will not generate a torque in $\boldsymbol{Z}_b$-axis given its location at the center of the face.

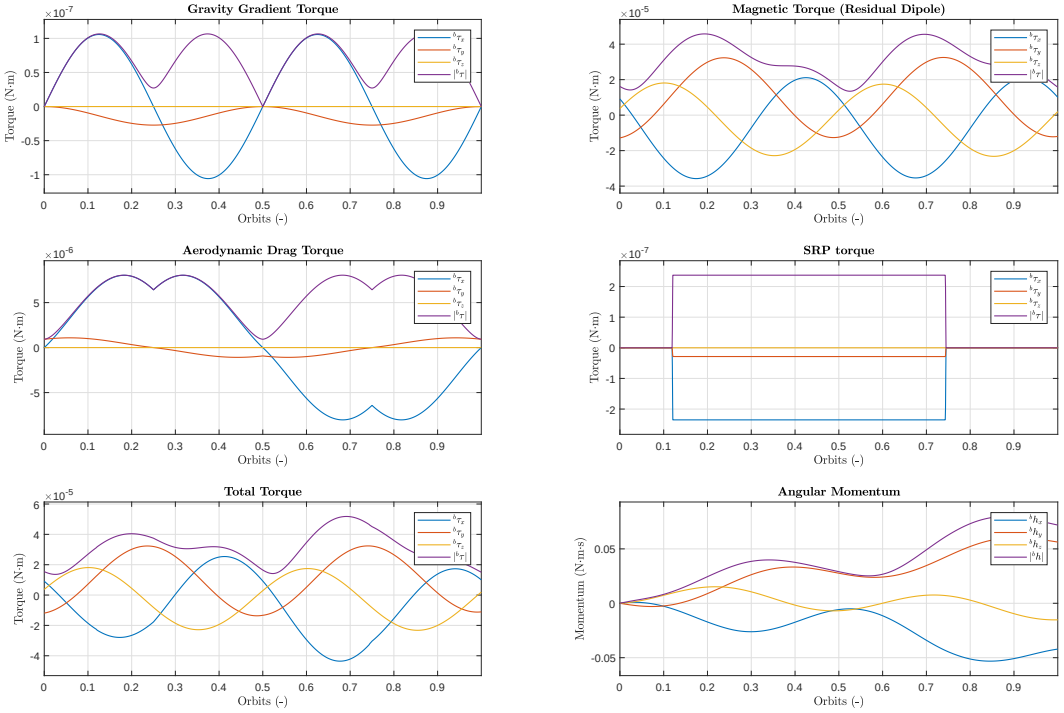

Figure 3.7: Evolution of the torques for inertial pointing (worst case scenario).

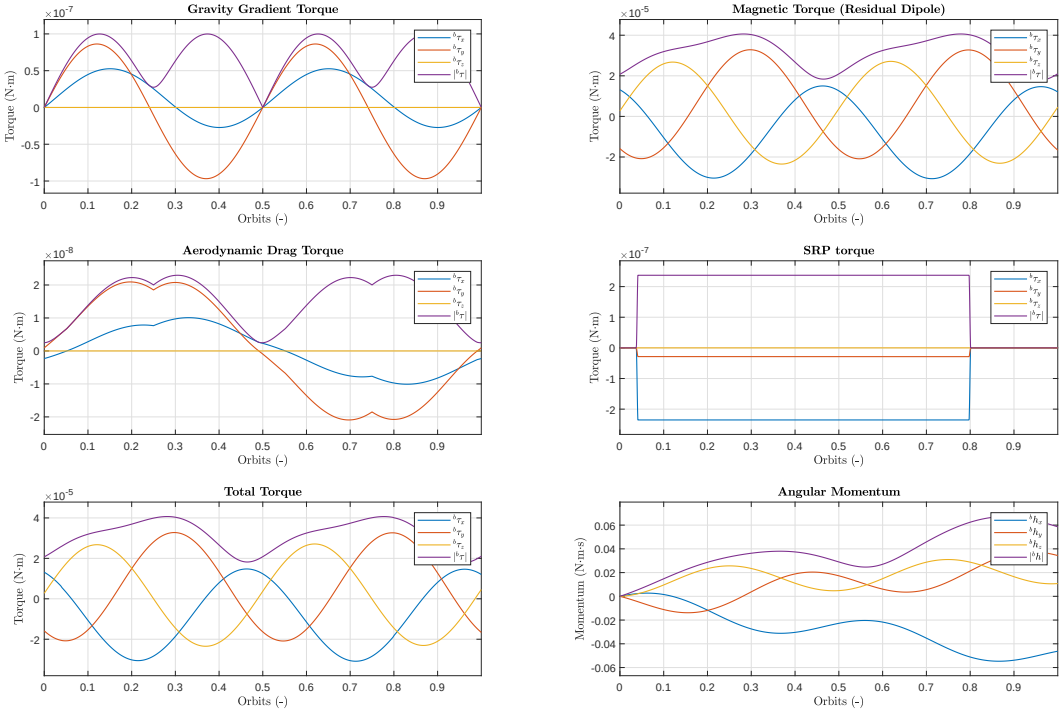

Figure 3.8: Evolution of the torques for inertial pointing (relaxed conditions).

4

HARDWARE

In this chapter, the sizing procedure for the attitude determination and control hardware is described. The minimal size for the actuators was calculated by taking into account the control accuracy and worst-case disturbance torques, while some restriction in the characteristics of the sensor were set by analysing the mission and the attitude determination requirements. At the end of each section, the characteristics of the selected components, as well as the modelling used for the simulations, are presented.

4.1. ACTUATORS

All the resulting worst-case disturbance torques calculated in Section 3.1 are summarized in Table 4.1, for which, two methods for estimating the total torque are proposed. Wertz and Larson [52] outlines that a good approximation would result from adding of all values these single values. Another approach, however more realistic, will be calculating the Residual Sum of Squares (RSS). The sum of all the disturbance torque was selected after a discussion, since it provides enough safety margin in case of non-modelled disturbances.

Source	**Maximal value** [$\mathbf{N \cdot m}$]
Gravity gradient torque	1.0657×10^{-7}
SRP torque	2.6418×10^{-7}
Aerodynamic drag torque	1.3622×10^{-5}
Magnetic dipole torque	4.7477×10^{-5}
Sum	$\mathbf{6.147 \times 10^{-5}}$
RSS	$\mathbf{4.9394 \times 10^{-5}}$

Table 4.1: Maximal environmental torques

4.1.1. Magnetic torquer

The magnetic torquers will be sized for each of the modes from Chapter 2, therefore the different sizing considerations according to the model are observed in Table 4.2. The maximal value from these results will be later sent to the procurements department for the acquisition of the hardware.

It shall be remarked that the RSS was employed for the calculation of the dipole for CAM and SFM under the assumption that , for one orbital period, the required dipoles for detumbling and disturbance rejection do not have the same direction.

Operational mode	Sizing considerations	Size of MTQ
DTM	$D_{MTQ} = D_{DTM}$	$5.7344\,\mathrm{A}\cdot\mathrm{m}^2$
CAM	$D_{MTQ} = \sqrt{{D_{DTM}}^2 + {D_{dist}}^2}$	$7.5542\,\mathrm{A}\cdot\mathrm{m}^2$
NOM	$D_{MTQ} = D_{dist}$	$4.9176\,\mathrm{A}\cdot\mathrm{m}^2$
SFM	$D_{MTQ} = \sqrt{{D_{DTM}}^2 + {D_{dist}}^2}$	$7.5542\,\mathrm{A}\cdot\mathrm{m}^2$

Table 4.2: Different sizing scenarios for the MTQs.

Magnetic dipole for detumbling

After the satellite is de-attached from the launcher, the magnetic torquers should be able to de-spin the satellite within the Δt provided by the EPS team. Given this assumption, the angular momentum of the satellite after separation can be calculated as

$$\begin{aligned} H_{sat} &= J_{sat_{max}}\,\omega_{sep_{max}}\,, \\ &= \left(2.957\,\mathrm{kg}\cdot\mathrm{m}^2\right)\left(0.1745\,\mathrm{rad}\cdot\mathrm{s}^{-1}\right), \\ &= 0.5161\,\mathrm{N}\cdot\mathrm{m}\cdot\mathrm{s}, \end{aligned} \tag{4.1}$$

where $\omega_{sep_{max}}$ is the maximal separation rate from the launcher. At this moment there is no further specification of this value, therefore a maximal separation rate of $10\,\mathrm{deg}\cdot\mathrm{s}^{-1}$ is assumed. The detumbling time should be $\Delta t \leq 4\,\mathrm{h}$, at most, given the EPS requirement and a maximal duty cycle of the MTQs during this phase of 50% is assumed; thus, the magnetic torque [52] necessary to slow-down the satellite will hence be

$$\begin{aligned} \tau_{DTM} &= \frac{H_{sat}}{0.5\,\Delta t}\,, \\ &= \frac{0.5161\,\mathrm{N}\cdot\mathrm{m}\cdot\mathrm{s}}{(0.5)\;14\,400\,\mathrm{s}}\,, \\ &= 7.168\times10^{-5}\,\mathrm{N}\cdot\mathrm{m}. \end{aligned} \tag{4.2}$$

Finally, the required MTQ dipole for detumbling can be computed by using

$$\begin{aligned} D_{DTM} &= \frac{\tau_{MTQ}}{B_{earth_{min}}\,\sin\theta}\,, \\ &= \frac{7.168\times10^{-5}\,\mathrm{N}\cdot\mathrm{m}}{(25\,000\,\mathrm{nT})\;\sin(30^\circ)}\,, \\ &= 5.7344\,\mathrm{A}\cdot\mathrm{m}^2\,, \end{aligned} \tag{4.3}$$

where $B_{earth_{min}}$ is the minimal magnitude of the geomagnetic field and θ is the minimal angle between the Earth's and the satellite's magnetic dipoles, both values where obtained from the previous mission [20].

After a discussion with the procurements department, the selected choice was a MTQ of $10\,\mathrm{A}\cdot\mathrm{m}^2$ which provides enough margin (more than 20%) against uncertainties in the MoI.

After the definition of the capabilities of the MTQs, a new analysis was proposed in order to determine the required time for detumbling using the current baseline MTQs. The results are consequently presented in Fig. 4.1, and they were obtained from equations 4.1, 4.2 and 4.3. Here, a maximal uncertainty of ±20 % in the MoI assumed.

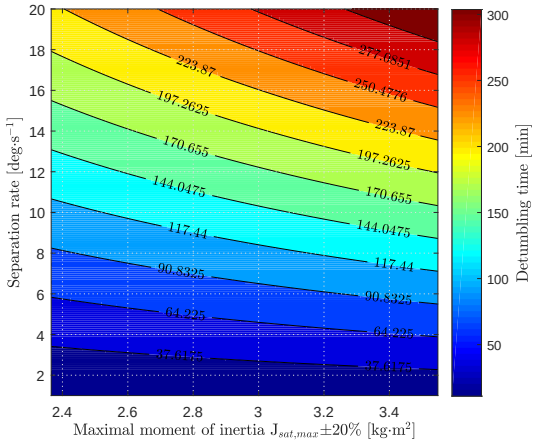

Figure 4.1: Estimated detumbling time for a MTQ of 10 A · m^2.

Magnetic dipole for disturbance rejection

The magnetic torquers will not only be used to detumble the satellite after launcher separation, but also for magnetic unloading of the wheels during NOM and for spin stabilization in absence of RW control during SFM & CAM.

In Fig. 4.2 the required magnetic dipole for disturbance rejection is presented for different environmental conditions. This values were calculated using the SRP, magnetic and gravity gradient torques from Chapter3 and the atmospheric drag torque estimated in Fig. 3.3.

For the sizing of the MTQs, a maximal disturbance torque of 6.147×10^{-5} N · m is considered (Table 4.1). This torque corresponds to a drag coefficient C_D of 2.5, an h of 500 km and a high shot-term solar activity. The disturbance torque is then substituted in equation 4.3 as

$$\begin{aligned} D_{dist} &= \frac{6.147 \times 10^{-5}\,\mathrm{N \cdot m}}{(25\,000\,\mathrm{nT})\,\sin(30°)}, \\ &= 4.9176\,\mathrm{A \cdot m^2}. \end{aligned}$$

Dynamical modelling

The torque produced by a MTQ can be easily modelled using the methodology of Wertz [51], which is

$$^{b}\vec{\boldsymbol{\tau}}_{MTQ} = {}^{b}\vec{\boldsymbol{D}}_{MTQ} \times {}^{b}\vec{\boldsymbol{B}}_{earth}, \tag{4.4}$$

and the corresponding transfer function between the commanded and the achieved magnetic dipole can be defined as a simple first order system

$$\mathcal{G}(s) = \frac{1}{1 + T_{MTQ}\, s}, \tag{4.5}$$

where T_{MTQ} is the time constant of the magnetic torquer.

The magnitude of previous transfer function is then

$$|\mathcal{G}(j\omega)| = \frac{1}{\sqrt{{T_{MTQ}}^2\, \omega_{co}^2 + 1}}, \tag{4.6}$$

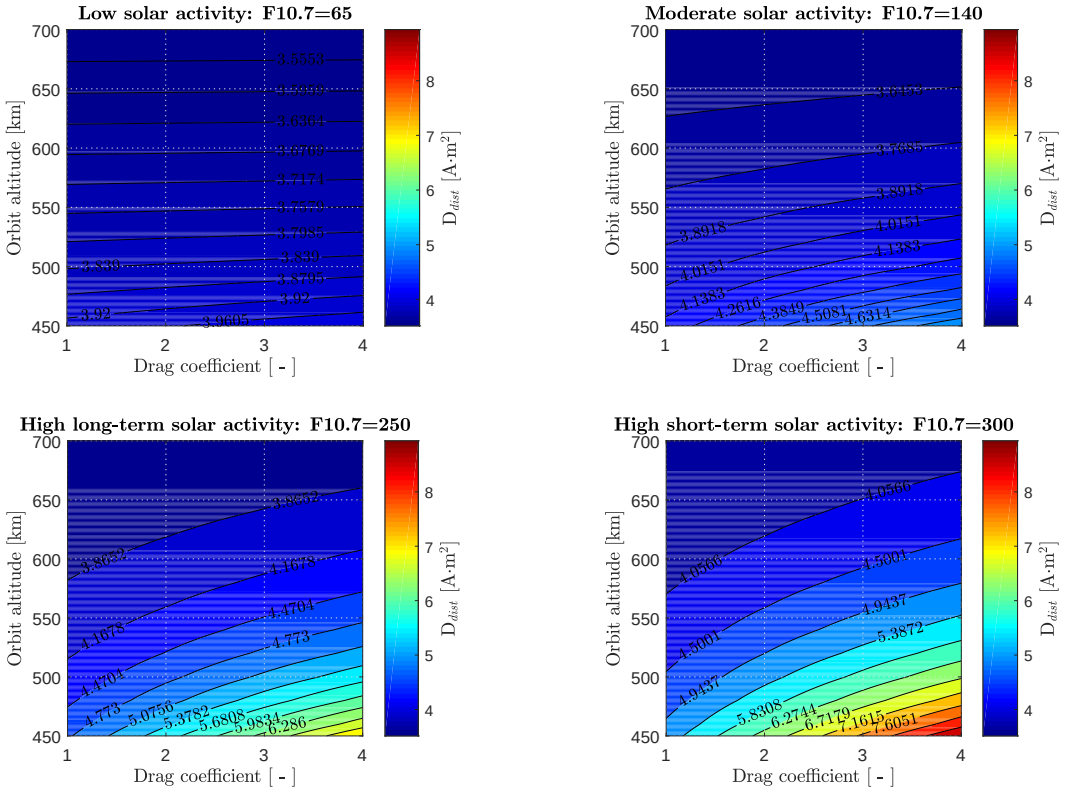

Figure 4.2: Required dipole for disturbance rejection in terms of h, C_D and the solar activity.

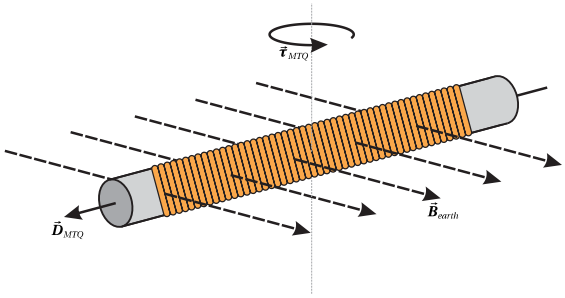

Figure 4.3: Magnetic torquer.

where ω_{co} stands for the cut-off frequency. If the elements of this equation are re-arranged as

$$T_{MTQ} = \sqrt{\left(\frac{1}{|\mathcal{G}(j\omega)|^2} - 1\right)\frac{1}{{\omega_{co}}^2}}, \tag{4.7}$$

the time response can be then calculated in terms of the cut-off frequency and maximal allowed signal attenuation. As baseline design, a maximal attenuation of $\mathcal{G}_{MTQ} = -3$ dB two decades after the maximal spinning rate is considered as baseline design, the cut-off frequency is therefore

defined as

$$\begin{aligned} \omega_{co} &= 10^2\, \omega_{max}\,, \\ &= 17.453\ \text{rad}\cdot\text{s}^{-1}\,, \end{aligned} \tag{4.8}$$

thus, the minimal time constant for the magnetic torquer evaluated in equation 4.7 should be

$$T_{MTQ} \leq 0.057\ \text{s}.$$

MT10-2-H magnetic torquer

The current baseline design are three magnetic torquers MT-10-2-H placed in every axis of the body frame, they will be provided by ZARM Technik AG which is located in Bremen, Germany [53]. Those torquers are capable of providing a maximal magnetic dipole of 10 A·m^2, with a time constant of 15 ms, other important characteristics are presented in Table 4.3. The same brand of MTQs (but 30 A $\cdot$ m^2) were used for the previous compact satellite, and to the date they have not been tested in space since *Eu:CROPIS* is still waiting to be launched. From [20], the only constraint is that MTQs shall be placed away from any magnetic material, otherwise they might induce some non-modelled parasitic torques.

Characteristic	Specification	Units
Lineal dipole range	10	A $\cdot$ m^2
Time response	15	ms
Supply voltage	10	V
Power consumption	1	W
Mass	300	g
Number of units	3	-

Table 4.3: Characteristics of the *MT-10-2-H* magnetic torquer.

4.1.2. Reaction wheel

In previous section, it was stated that most of the torque for the control loop will be provided by the MTQs. Therefore, the reaction wheels are used as secondary actuators for the fine pointing manoeuvres, this means, RWs will only be sized for NOM, as shown in Table 4.4.

Operational mode	Sizing considerations	Size of RW
DTM	-	-
CAM	-	-
NOM	$H_{RW} = H_{dist}$	61.7 mN·m·s
SFM	-	-

Table 4.4: Sizing scenarios for the reaction wheels

Wertz and Larson [52] proposed the following formula

$$H_{RW} = \tau_{dist}\, \frac{1}{\sqrt{2}}\, \frac{T_{orbit}}{4}\,, \tag{4.9}$$

which allows the calculation of the required RWs angular momentum for disturbance rejection, where T_{orbit} is the orbital period and $1/\sqrt{2}$ stands for the RMS average of a sinusoidal function. For this analysis it is assumed that the wheels are saturated at 1/4 of the orbit. Following the

same design procedure as for the MTQs, the results depicted in Fig. 4.4 represent the ideal wheel size for different values of drag coefficient, altitude and solar activity.

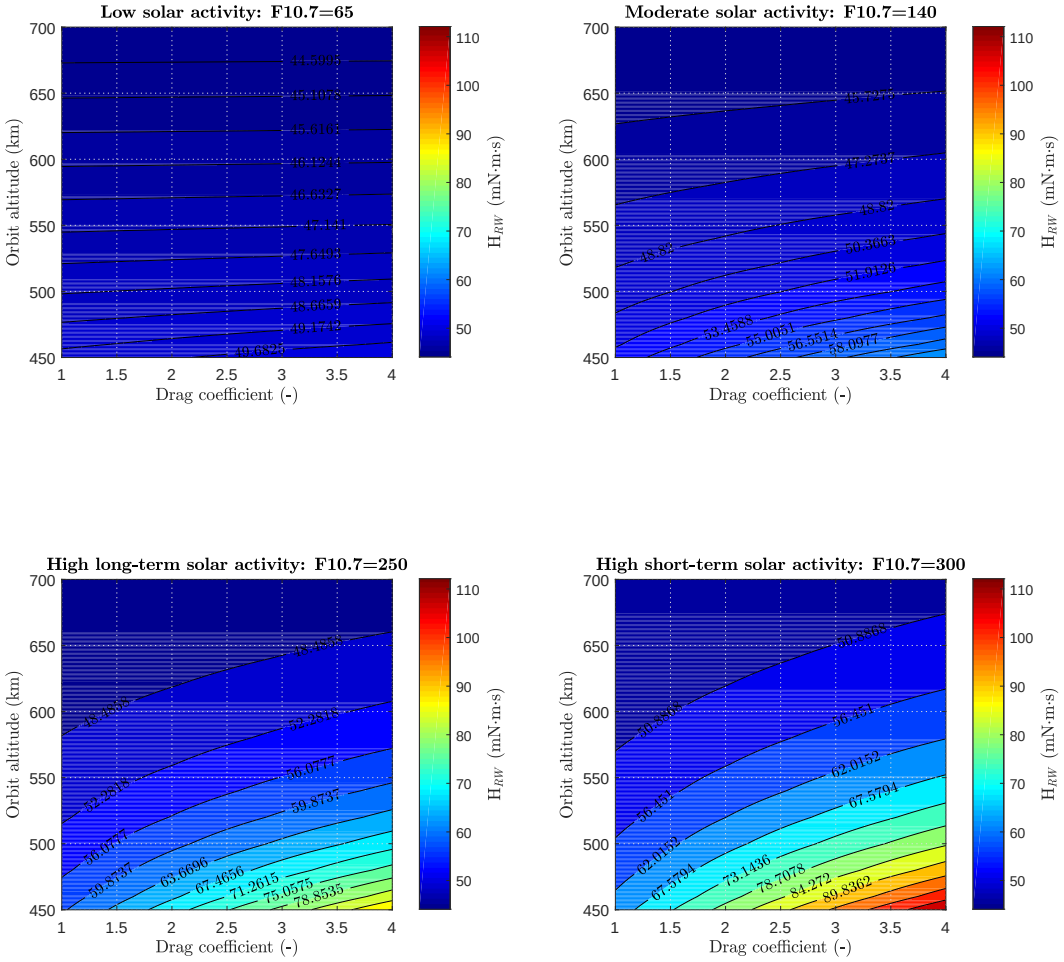

Figure 4.4: RW size in terms of h, C_D and the solar activity.

For an orbit of 500 km, C_D of 2.5 and high-short term solar activity the ideal size of the reaction wheel for disturbance rejection would be approximately

$$H_{RW} = \left(6.147 \times 10^{-5}\,\mathrm{N\cdot m}\right) 0.7071 \left(\frac{5676.97\,\mathrm{s}}{4}\right),$$
$$= 61.7\,\mathrm{mN\cdot m\cdot s}.$$

Previous results are also complying with the estimations from Section 3.3, and since most of the manoeuvres for NOM are considered to be slow (<1 deg·s), no further restrictions on this actuator will be given.

Dynamical modelling

A reaction wheel can be modelled following the methodology proposed by Sidi [42], where the model can be deduced from a separated modelling of the mechanical and electrical parts. The

equivalent electric circuit is observed in Fig. 4.5 and its corresponding mathematical representation is easily inferred by using Kirchoff's voltage law, or

$$L_a \frac{di_a}{dt} = u_a - R_a\, i_a - e_a\,, \tag{4.10}$$

where L_a is the armature inductance, R_a is the armature resistance, i_a the electrical current, u_a the excitation voltage, and e_a is the back electromotive force, which is defined as

$$e_a = K_v\, \omega_m\,; \tag{4.11}$$

K_v is known as voltage constant.

In the same manner, the model of the mechanical part is deduced from Newton's second law, or

$$J_m \frac{d\omega_m}{dt} = \tau_m - b_m\, \omega_m\,, \tag{4.12}$$

where J_m is the rotor's moment of inertia, b_m is the rotor's viscous friction coefficient and the mechanical torque τ_m is linked to the armature current by means of

$$\tau_m = K_\tau\, i_a\,; \tag{4.13}$$

K_τ is known as torque constant.

If equations 4.11 and 4.13 are substituted into equations 4.10 and 4.12, respectively, and then the Laplace transformation is applied to both equations, the result will be

$$(J_m\, s + b_m)\, \omega(s) = K_\tau\, i_a(s)\,, \tag{4.14}$$

$$(L_a\, s + R_a)\, i_a(s) = u_a - K_v\, \omega_m(s)\,, \tag{4.15}$$

if then both equations are merged considering u_a as the system input and ω_m as the system output, the resulting transfer function will be

$$\frac{\omega(s)}{u_a(s)} = \frac{K_\tau}{(J_m\, s + b_m)(L_a\, s + R_a) + K_\tau\, K_v}, \tag{4.16}$$

this equation can be rewritten in terms of the produced torque as

$$\frac{\tau_{RW}(s)}{u_a(s)} = \frac{J_m\, K_\tau\, s}{(J_m\, s + b_m)(L_a\, s + R_a) + K_\tau\, K_v}\,. \tag{4.17}$$

Previous transfer function allows to calculate the torque produced by a reaction wheel in terms of the excitation voltage. However, one of the design requirements for the RW model was to obtain the produced torque in terms of the commanded torque τ_{com}. For this purpose, equation 4.17 is used to obtain a reference armature current $i_{a_{com}}$, then the loop is closed with the real i_a and therefore a constant T_{RW} (time constant of the wheel) is introduced to the model using the methodology described by Sidi [42] . This modification yields to a new transfer function of the form

$$\frac{\tau_{RW}(s)}{\tau_{com}(s)} = \frac{R_a\, J_m}{T_{RW}(J_m\, s + b_m)(L_a\, s + R_a) + T_{RW}\, K_\tau\, K_v + R_a\, J_m}, \tag{4.18}$$

A second requirement in the RW was provided by the EPS system; the electrical power bleed by one single RW when switching to nominal mode shall be measured. This requirement is easily achieved by computing product of the armature voltage u_a times the current i_a, or

$$P_{RW} = u_a\, i_a\,. \tag{4.19}$$

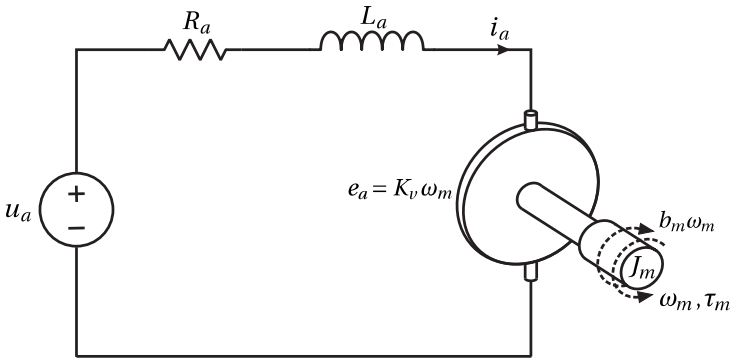

Figure 4.5: Reaction wheel dynamical model

RW3-0.060 reaction wheel

The preliminary design includes three reaction wheels located in each of the axis of the body frame. The provider is Sinclair Interplanetary which is based in Toronto, Canada. Those wheels have a nominal capacity of 60 mN · m · s, which fulfils the requirements of previous section. However, and if required, those wheels can provide up to 180 mN · m · s by changing the input voltage[43], the characteristics can be seen in Table 4.5.

Characteristic	**Specifications (nominal/maximal)**	**Units**
Angular momentum	60/180 @28 V	mN · m · s
Torque	±20 @ 0.12 N·m·s, 28 V	N · m
Moment of inertia of the rotor	86.6×10^{-6}	kg · s
Supply voltage	7.5-34/50	V
Power consumption	23.4 @ 0.12 N·m·s, 10 mN·m	W
Mass	226	g
Number of units	3	-

Table 4.5: Characteristics of the *RW3-0.060* reaction wheel.

4.2. SENSORS

Since different measurements are required for every mode, an analysis concerning the minimal requirements for each sensor is studied in this section. The following sensors are foreseen as baseline design for S2TEP:

4.2.1. Gyroscope

The angular rates are one of the most important measurements; therefore, some minimal requirements for the hardware acquisition shall be given.

The bandwidth of the gyroscope is desired to be at least ten times bigger than minimal control frequency, that is

$$\begin{aligned} BW_{GYR} &\geq 10\, f_{ctrl}, \\ &\geq 3\,\text{Hz}, \end{aligned}$$

and a the maximal noise level is selected to be

$$\eta_{GYR} \leq 0.3 \, \text{deg} \cdot \text{h}^{-1} .$$

using the reference value from *Eu:CROPIS* [20].

The gyroscopes are the main source of angular rate measurements, therefore they should at least be able to provide a measurement of the maximal spin rate

$$\begin{aligned} range_{GYR} &\geq \omega_{max} , \\ &\geq 10 \, \text{deg} \cdot \text{s}^{-1} , \end{aligned}$$

regarding the minimal resolution of the gyroscope, it is selected to be

$$\begin{aligned} res_{GYR} &\leq 10 \times 10^{-3} \, \text{deg} \cdot \text{s}^{-1} , \\ &\leq 36 \, \text{deg} \cdot \text{h}^{-1} , \end{aligned}$$

according to the requirements of Table 2.1. In addition, the drift or bias should carefully be taken into account since the gyroscope is the main source of information for attitude estimation during eclipse for SFM and CAM. Therefore, the maximal deviation is considered to be 5°, or

$$\begin{aligned} bias_{GYR} &\leq \frac{5 \, \text{deg}}{47.3 \, \text{min}} , \\ &\leq 6.34 \, \text{deg} \cdot \text{h}^{-1} , \end{aligned}$$

if a maximal eclipse time of $\frac{T_{orbit}}{2} \approx 47.3$ min is considered.

The parameters calculated in the previous paragraphs were used for the selection of the final gyroscope for the mission, the model is *STIM300* IMU and it is manufactured by Sensonor, which is located in Spain. The main characteristics[41] of this sensor are shown in Table 4.6.

Characteristic	**Specification**	**Units**
Range	± 400	$\text{deg} \cdot \text{s}^{-1}$
Resolution	0.22	$\text{deg} \cdot \text{h}^{-1}$
Bias	± 250	$\text{deg} \cdot \text{h}^{-1}$
Bias run-run	± 4	$\text{deg} \cdot \text{h}^{-1}$
Random walk	0.15	$\text{deg} \cdot \text{h}^{1/2}$
Supply voltage	5	V
Power consumption	1.5 / 2	W
Mass	55	g
Number of units	1	–

Table 4.6: Characteristics of the *STIM300* IMU

It shall be remarked that even though the bias of the baseline gyroscope is bigger than the one calculated as requirement, this IMU can still be used for the final implementation since an in-orbit calibration can be performed. The value of the bias due to switching off and on (bias run -run) is now considered as specification, and given that the value of the IMU smaller than the requirements, there was no necessity of selecting a new sensor.

4.2.2. Magnetometer

The magnetometer should provide information regarding the evolution of the Earth's magnetic field at any point in the orbit. According to Thébault et al. [49] the value of this field for a typical

LEO satellite varies from 25000 to 60000 nT; hence, the range of the magnetometer should at least be equal to the maximal value of the geomagnetic field

$$range_{MAG} \geq 60\,000\,\text{nT},$$

regarding its minimal resolution, the magnetometer should be able to at least provide a measurement of 0.1° for the nominal modes and minimal magnetic field

$$\begin{aligned} res_{MAG} &\leq \arctan\left(0.1^\circ\right) \frac{1}{25\,000}\,\text{nT}, \\ &\leq 69.81\,\text{nT}, \end{aligned}$$

the bandwidth is directly related to the control frequency and it is set to be at least ten times bigger

$$BW_{MAG} \geq 3\,\text{Hz}.$$

The current choice for the magnetometer is the model *AMR digital*, it is provided by ZARM Technik AG which is located in Bremen, Germany. The characteristics [54] of this sensor are shown in Table 4.7.

Characteristic	**Specifications (nominal/maximal)**	**Units**
Range	±250	μT
Resolution	10	nT
Accuracy	< ± 2.5	μT
Bandwidth	50 - 240	Hz
Supply voltage	5 - 16	V
Power consumption	< 0.6 @ 15 V	W
Mass	55	g
Number of units	1	-

Table 4.7: Characteristics of *AMR digital* magnetometer.

4.2.3. Sun sensor

The Sun sensors are one of the most important information sources since its measurement will be used during the early-orbit modes to orient the satellite towards the Sun direction. Therefore, the position of the Sun should be available all the time (except for eclipse). The calculation of the number of sensors required for the mission will depend on the shape of the satellite and the field of view of the selected model. A typical FoV in the market is 120 ° and knowing that S2TEP is roughly a cube, the minimal number of sensors should be at least 12 or 6 (one or two per face if the sensor has a linear or squared FoV, respectively)

$$FoV_{SS} \geq 120^\circ,$$

The requirements presented in Table 2.1 show that the Sun sensor will be used for a pointing accuracy of at most 1 ° during SFM and CAM, therefore the minimal accuracy of this sensor should be

$$res_{SS} \leq 0.1^\circ.$$

The restrictions in the bandwidth are again provided by the control frequency, a minimal

bandwidth of 10 times the control frequency

$$BW_{SS} \geq 3\ Hz.$$

S2TEP will likely have the same sensor configuration as *Eu:CROPIS*; in that case, only 6 sensors will be required given that this sensor has a square FoV. The current provider is Solar MEMS and the model of the sensor is the *SSOC-D60* [45], whose principal characteristics are observed in Table 4.8.

Characteristic	**Specification**	**Units**
Field of view	± 60	deg
Accuracy	< 0.03 (3σ)	deg
Precision	< 0.05	deg
Update rate	> 10	Hz
Supply voltage	5	V
Power consumption	0.35	W
Mass	35	g
Number of units	6	-

Table 4.8: Characteristics of the *SSOC-D60* Sun sensor.

4.2.4. Star tracker

One of the most accurate sensors for attitude determination is the start tracker. Since stars are inertially fixed bodies in the deep space and its size is very small when seen from the solar system, accuracy of the order of few arc-seconds can be reached with this kind of sensors. For S2TEP, an star tracker was considered in order to accomplish the attitude determination requirements for NOM.

Regarding the selection parameters, the smaller the FoV, the better the accuracy. According to Table 2.1 , the minimal required accuracy for attitude determination in NOM is 0.1°, therefore

$$accu_{ST} \leq 0.1^{\circ},$$

in addition, strictly speaking (assuming that the STR would be the only sensor providing attitude determination for NOM) its minimal update shall be at least three times bigger than the control frequency

$$rate_{ST} \geq 3\,\mathrm{Hz},$$

in reality however, this does not happen. The measurements of this sensor will be combined with all other sensor measurements in a Kalman filter, and therefore a smaller update rate can be allowed.

The star trackers are often limited by a slew rate, as this sensor will be used in this mission only for fine pointing, that means during NOM. If a maximal angular rate of 1 deg $\cdot\,\mathrm{s}^{-1}$ is hence considered for this mode, that means 3 minutes for a 180° turn, the slew rate will be

$$SR_{ST} \leq 1\ \mathrm{deg}\cdot\mathrm{s}^{-1}. \tag{4.20}$$

The current provider is Berlin Space Technologies and the model of the sensor is *ST-200*, located in Berlin, Germany. The characteristics are shown in Table 4.9[6].

Characteristic	Specification	Units
Accuracy	30 (3σ)	arcsec
Update rate	1	Hz
Slew rate	< 1	$\deg \cdot s^{-1}$
Power consumption	220 / 650	mW
Supply voltage	3.5 - 5	V
Mass	50	g
Number of units	1	-

Table 4.9: Characteristics of the *ST-200* star tracker.

4.2.5. GPS

The information about the position of the satellite in the inertial frame is not only important for the ADCS (this measurement is used for the computation of the orbital velocity and position vectors) but also for the on-board computer and the flight dynamics subsystem. Therefore, the restrictions for the GPS will not be given by the ADCS team.

The current solution is provided by DLR itself, and is a set of an antenna, amplifier and the *Phoenix* receiver, for which the main characteristics[9] are outline in Table 4.10 .

Characteristic	Specification	Units
Update rate	1 - 5	Hz
Supply voltage	5	
Power consumption	0.85	W
Mass	20	g
Number of units	1	-

Table 4.10: Characteristics of the *Phoenix* GPS.

5

SATELLITE DYNAMICS AND CONTROL

In this chapter, the mathematical derivation of the position and attitude dynamics is obtained. Furthermore, the formulation of the control algorithms, stability proofs, as well as the final feedback gains selected for each of the different pointing modes are explained in detail.

5.1. SATELLITE DYNAMICS

5.1.1. Position dynamics

The position dynamics can be easily modelled by using the Newton's second law

$$ {}^{i}\vec{\boldsymbol{f}} = m_{sat}\frac{d}{dt}({}^{i}\vec{\boldsymbol{v}}), \tag{5.1} $$

where ${}^{i}\vec{\boldsymbol{v}}$ is the orbital velocity represented in the inertial frame and ${}^{i}\vec{\boldsymbol{f}}$ is the sum of all the external forces acting on the satellite, which for this analysis are

$$ {}^{i}\vec{\boldsymbol{f}} = {}^{i}\vec{\boldsymbol{f}}_{ctrl} + {}^{i}\vec{\boldsymbol{f}}_{gg} + {}^{i}\vec{\boldsymbol{f}}_{srp} + {}^{i}\vec{\boldsymbol{f}}_{atm}, \tag{5.2} $$

note that the environmental forces can also be unified in a single vector as

$$ {}^{i}\vec{\boldsymbol{f}}_{dist} = {}^{i}\vec{\boldsymbol{f}}_{gg} + {}^{i}\vec{\boldsymbol{f}}_{srp} + {}^{i}\vec{\boldsymbol{f}}_{atm}, \tag{5.3} $$

Thus, equation 5.1 can be rewritten as

$$ m_{sat}\,{}^{i}\ddot{\vec{\boldsymbol{r}}} = {}^{i}\vec{\boldsymbol{f}}_{ctrl} + {}^{i}\vec{\boldsymbol{f}}_{dist}, \tag{5.4} $$

or

$$ {}^{i}\ddot{\vec{\boldsymbol{r}}} = \frac{1}{m_{sat}}\left({}^{i}\vec{\boldsymbol{f}}_{ctrl} + {}^{i}\vec{\boldsymbol{f}}_{dist}\right). \tag{5.5} $$

for the simulation model.

At this moment, S2TEP is not planned to have the capability to perform orbital manoeuvres (${}^{i}\vec{\boldsymbol{f}}_{ctrl} = 0$). However, the equations previously presented can still be used for the estimation of the position and orbit velocity of the satellite w.r.t. to the Earth.

A more detailed analysis of the orbital mechanics is presented in Appendix B.

5.1.2. Attitude dynamics

The attitude dynamics of a satellite has been widely studied by many authors [24, 51, 30, 42, 39] in the previous years. The most common method to model the attitude dynamics of satellite without flexible appendages is by means of the Euler's equations of rotational motion. For that,

Markley and Crassidis [30] define the angular momentum of a spinning satellite as

$$^{b}\vec{\boldsymbol{H}}_{sat} = \boldsymbol{J}_{sat}\,{}^{b}\vec{\boldsymbol{\omega}}_{sat}\,, \tag{5.6}$$

where $^{b}\vec{\boldsymbol{\omega}}_{sat}$ is the angular velocity of the satellite with respect to the inertial frame, represented in the body frame. The relationship between the torque and the angular momentum is defined as

$$^{b}\vec{\boldsymbol{\tau}} = \frac{d}{dt}\left(^{b}\vec{\boldsymbol{H}}_{sat}\right), \tag{5.7}$$

where $^{b}\vec{\boldsymbol{\tau}}$ is the sum of all the internal and external torques acting on the satellite, which for this mission are

$$^{b}\vec{\boldsymbol{\tau}} = {}^{b}\vec{\boldsymbol{\tau}}_{ctrl} + {}^{b}\vec{\boldsymbol{\tau}}_{gg} + {}^{b}\vec{\boldsymbol{\tau}}_{srp} + {}^{b}\vec{\boldsymbol{\tau}}_{mag} + {}^{b}\vec{\boldsymbol{\tau}}_{atm}\,, \tag{5.8}$$

in the same ways as for the external forces, the external torques can be unified in a single vector as

$$^{b}\vec{\boldsymbol{\tau}}_{dist} = {}^{b}\vec{\boldsymbol{\tau}}_{gg} + {}^{b}\vec{\boldsymbol{\tau}}_{srp} + {}^{b}\vec{\boldsymbol{\tau}}_{mag} + {}^{b}\vec{\boldsymbol{\tau}}_{atm}\,. \tag{5.9}$$

If equation 5.7 is represented in the inertial frame by using the corresponding rotation matrix

$$^{b}\vec{\boldsymbol{\tau}} = \frac{d}{dt}\left(^{b}\boldsymbol{R}_{i}\,{}^{i}\vec{\boldsymbol{H}}_{sat}\right), \tag{5.10}$$

and the derivation of the product is performed by using the definition of the derivative of a rotation matrix of section A.3 as

$$^{b}\vec{\boldsymbol{\tau}} = {}^{b}\dot{\boldsymbol{R}}_{i}\,{}^{i}\vec{\boldsymbol{H}}_{sat} + {}^{b}\boldsymbol{R}_{i}\,{}^{i}\dot{\vec{\boldsymbol{H}}}_{sat}\,, \tag{5.11}$$

this results in

$$\begin{aligned} ^{b}\vec{\boldsymbol{\tau}} &= {}^{b}\vec{\boldsymbol{\omega}}_{sat} \times {}^{b}\boldsymbol{R}_{i}\,{}^{i}\vec{\boldsymbol{H}}_{sat} + {}^{b}\boldsymbol{R}_{i}\,{}^{i}\dot{\vec{\boldsymbol{H}}}_{sat}\,, \\ &= {}^{b}\vec{\boldsymbol{\omega}}_{sat} \times {}^{b}\vec{\boldsymbol{H}}_{sat} + {}^{b}\dot{\vec{\boldsymbol{H}}}_{sat}\,. \end{aligned} \tag{5.12}$$

If definition 5.6 is the substituted into equation 5.12, this leads to

$$^{b}\vec{\boldsymbol{\tau}} = \boldsymbol{J}_{sat}\,{}^{b}\dot{\vec{\boldsymbol{\omega}}}_{sat} + {}^{b}\vec{\boldsymbol{\omega}}_{sat} \times \left(\boldsymbol{J}_{sat}\,{}^{b}\vec{\boldsymbol{\omega}}_{sat}\right), \tag{5.13}$$

and for the simulator

$$^{b}\dot{\vec{\boldsymbol{\omega}}}_{sat} = \boldsymbol{J}_{sat}{}^{-1}\left(-{}^{b}\vec{\boldsymbol{\omega}}_{sat} \times \left(\boldsymbol{J}_{sat}\,{}^{b}\vec{\boldsymbol{\omega}}_{sat}\right) + \vec{\boldsymbol{\tau}}_{ctrl} + \vec{\boldsymbol{\tau}}_{dist}\right). \tag{5.14}$$

For NOM the cross-coupling effects of the reaction wheels were also added to the simulation model as disturbances

$$\vec{\boldsymbol{\tau}}_{dist} = \vec{\boldsymbol{\tau}}_{dist} + -{}^{b}\vec{\boldsymbol{\omega}}_{sat} \times \vec{\boldsymbol{H}}_{RW}\,. \tag{5.15}$$

The attitude of the satellite will be represented by using quaternions (see Appendix A), the equation that relates angular velocity and the derivative of a quaternion can be obtained using the definition A.29

$$^{b}\dot{\mathbf{q}}_{i} = \frac{1}{2}\,{}^{b}\boldsymbol{\Omega}'\,{}^{b}\mathbf{q}_{i}\,. \tag{5.16}$$

If a diagonal MoI matrix is assumed, the elements of equations 5.14 and 5.16 will be

$$\begin{aligned}
\dot{\omega}_x &= \left(\frac{J_y - J_z}{J_x}\right)\omega_y\,\omega_z + \frac{\tau_x}{J_x}, \\
\dot{\omega}_y &= \left(\frac{J_z - J_x}{J_y}\right)\omega_z\,\omega_x + \frac{\tau_y}{J_y}, \\
\dot{\omega}_z &= \left(\frac{J_x - J_y}{J_z}\right)\omega_x\,\omega_y + \frac{\tau_z}{J_z},
\end{aligned} \tag{5.17}$$

and

$$\begin{aligned}
\dot{q}_1 &= \frac{\omega_x\,q_4 - \omega_y\,q_3 + \omega_z\,q_2}{2}, \\
\dot{q}_2 &= \frac{\omega_x\,q_3 + \omega_y\,q_4 - \omega_z\,q_1}{2}, \\
\dot{q}_3 &= \frac{-\omega_x\,q_2 + \omega_y\,q_1 + \omega_z\,q_4}{2}, \\
\dot{q}_4 &= \frac{-\omega_x\,q_1 - \omega_y\,q_2 - \omega_z\,q_3}{2},
\end{aligned} \tag{5.18}$$

they both were used for the development of the controllers of the next sections, while equations 5.16 and 5.14 were used for the simulation of the attitude dynamics.

5.2. CONTROL

In order to achieve the pointing performance for the different modes, different controllers must be defined within each mode. All the controllers selected for the S2TEP mission are summarized in Table 5.1.

Mode	Control algorithms	Restrictions
DTM	B-dot control	$\Delta t \leq 4\,\text{h}$
CAM	Spin control Precession control Nutation control	$\gamma \leq 5°$
NOM	Linear Quadratic Regulator Magnetic unloading of the RWs	$\phi \leq 1°$ $\theta \leq 1°$ $\psi \leq 1°$
SFM	Same as for CAM	$\gamma \leq 5°$

Table 5.1: Selected control algorithm for each ADCS mode.

5.2.1. Control frequency

The minimal control frequency is directly related to the maximal angular rate that the satellite can support by design. Its value should at least allow the control system to perform 10 commands within one revolution at the maximal rate $\left(\omega_{max} = 10\,\text{deg}\cdot\text{s}^{-1} = 0.1745\,\text{rad}\cdot\text{s}^{-1}\right)$

$$f_{ctrl} = 10\,\omega_{max}\left(\frac{1}{2\pi}\right), \tag{5.19}$$

$$= 0.277\,\text{Hz}, \tag{5.20}$$

$$\approx 0.3\,\text{Hz}.$$

5.2.2. B-dot controller

The B-dot control algorithm has widely been used in the previous years as the best alternative to detumble satellites with solely magnetic actuation [15, 5, 40, 2], this also includes last satellites built and launched by DLR [21, 19]. Given the simplicity of the mathematical definition and implementation, this algorithm has been chosen to damp the satellite's angular rate after the separation from the launcher.

The most typical formulation of the B-dot controller consist on measuring the direction of the geomagnetic field, and then a torque, with the maximal magnetic dipole, in the opposite direction is applied to decrease the angular rate, or

$$^{b}\vec{\boldsymbol{D}}_{ctrl} = -D_{max}\, sgn\left(^{b}\dot{\vec{\boldsymbol{B}}}_{earth}\right), \tag{5.21}$$

where D_{max} is the maximal dipole that a single magnetic torquer can provide.

In recent years, a new formulation of the B-dot algorithm has been proposed in order to improve the performance by reducing the time for detumbling, this new definition uses the measurements of the angular rates and magnitude of the geomagnetic field to perform the correction manoeuvres. From equation

$$^{b}\vec{\boldsymbol{D}}_{ctrl} = -K_{DTM}\, ^{b}\dot{\vec{\boldsymbol{B}}}_{earth}, \tag{5.22}$$

Avanzini and Giulietti [5] outlines that the derivative of the geomagnetic field can be approached by the cross product of the angular rate times the magnetic field, or

$$^{b}\vec{\boldsymbol{D}}_{ctrl} = \frac{-K_{DTM}}{\|^{b}\vec{\boldsymbol{B}}_{earth}\|^{2}}\left(^{b}\vec{\boldsymbol{B}}_{earth} \times\, ^{b}\vec{\boldsymbol{\omega}}_{sat}\right). \tag{5.23}$$

For experimental purposes, previous definition was considered as baseline design for the detumbling mode, for which a feedback gain of

$$K_{DTM} = 5 \times 10^{-3}. \tag{5.24}$$

was chosen by "trial-and-error".

As result of this analysis, two baseline solutions were implemented in the simulator:

- The controller from equation 5.21 for high angular rates and the controller from 5.22 for low angular rates.
- Controller from equation 5.23 for the whole detumbling phase.

Although both solutions are able to detumble the satellite within the requirements provided by the EPS, the second baseline solution was chosen given its better performance under the same simulation conditions.

Stability proof

The following Lyapunov function is proposed

$$V = \frac{1}{2}\vec{\boldsymbol{\omega}}_{sat}^{T}\, \boldsymbol{J}_{sat}\, \vec{\boldsymbol{\omega}}_{sat}, \tag{5.25}$$

and its corresponding time derivative is

$$\dot{V} = \vec{\boldsymbol{\omega}}_{sat}^{T}\, \boldsymbol{J}_{sat}\, \dot{\vec{\boldsymbol{\omega}}}_{sat}. \tag{5.26}$$

By substituting equation 5.14 on previous equation, it becomes

$$\dot{V} = \vec{\boldsymbol{\omega}}_{sat}^{T}\left(-\vec{\boldsymbol{\omega}}_{sat} \times (\boldsymbol{J}_{sat}\,\vec{\boldsymbol{\omega}}_{sat}) + \vec{\boldsymbol{\tau}}_{ctrl} + \vec{\boldsymbol{\tau}}_{dist}\right), \tag{5.27}$$

then by calculating the control torque as

$$\begin{aligned} \vec{\boldsymbol{\tau}}_{ctrl} &= \vec{\boldsymbol{D}}_{ctrl} \times \vec{\boldsymbol{B}}_{earth}, \\ &= \left(-K_{DTM}\,\dot{\vec{\boldsymbol{B}}}_{earth}\right) \times \vec{\boldsymbol{B}}_{earth}, \end{aligned} \tag{5.28}$$

the equation now becomes

$$\dot{V} = \vec{\boldsymbol{\omega}}_{sat}^{T}\left(-\vec{\boldsymbol{\omega}}_{sat} \times (\boldsymbol{J}_{sat}\,\vec{\boldsymbol{\omega}}_{sat}) + \left(-K_{DTM}\,\dot{\vec{\boldsymbol{B}}}_{earth}\right) \times \vec{\boldsymbol{B}}_{earth} + \vec{\boldsymbol{\tau}}_{dist}\right), \tag{5.29}$$

and by knowing that

$$\begin{aligned} \vec{\boldsymbol{\omega}}_{sat}^{T}\left[\left(-K_{DTM}\,\dot{\vec{\boldsymbol{B}}}_{earth}\right) \times \vec{\boldsymbol{B}}_{earth}\right] &= K_{DTM}\,\vec{\boldsymbol{\omega}}_{sat}^{T}\left(\vec{\boldsymbol{B}}_{earth} \times \dot{\vec{\boldsymbol{B}}}_{earth}\right), \\ &= K_{DTM}\left(\vec{\boldsymbol{\omega}}_{sat} \times \vec{\boldsymbol{B}}_{earth}\right)^{T}\dot{\vec{\boldsymbol{B}}}_{earth} \\ &= K_{DTM}\left(-\dot{\vec{\boldsymbol{B}}}_{earth}\right)^{T}\dot{\vec{\boldsymbol{B}}}_{earth}, \\ &= -K_{DTM}\|\dot{\vec{\boldsymbol{B}}}_{earth}\|^{2}, \end{aligned} \tag{5.30}$$

the final equation will be

$$\dot{V} = -K_{DTM}\|\dot{\vec{\boldsymbol{B}}}_{earth}\|^{2} + \vec{\boldsymbol{\omega}}_{sat}^{T}\vec{\boldsymbol{\tau}}_{dist}. \tag{5.31}$$

If the geomagnetic field in the inertial frame is assumed to be bounded $B_1 < \|\vec{\boldsymbol{B}}_{earth}\| < B_2$, with the proper choice of K_{DTM}, the previous equation can be made negative definite.

For the enhanced version of the controller, the stability proof is made in a quite straight forward way.

5.2.3. Spin, precession and nutation control

Let $\vec{\boldsymbol{N}}_{orbit}$ be the orbit normal vector in the direction of the Sun, which is fixed in the inertial frame, the goal of this control formulation is to align satellite's $\boldsymbol{Z}_{\mathcal{b}}$-axis with the orbit normal vector while spinning at a constant rate. For the development of this controller the following is assumed:

- The maximal MoI is placed in $\boldsymbol{Z}_{\mathcal{b}}$-axis.
- There are no off-diagonal elements (no disablements of the body frame axes).
- Components J_x and J_y are equal.

The following MoI matrix is hence proposed for the derivation of the CAM controller:

$$\boldsymbol{J}_{sat_{CAM}} = \begin{bmatrix} 1.5818 & 0 & 0 \\ 0 & 1.5818 & 0 \\ 0 & 0 & 1.68138 \end{bmatrix} \mathrm{kg \cdot m^{-1}}. \tag{5.32}$$

The desired angular momentum vector represented in the body frame is defined by de Ruiter [8] as

$${}^{\mathcal{b}}\vec{\boldsymbol{H}}_{des} = \boldsymbol{J}_{sat}\,{}^{\mathcal{b}}\vec{\boldsymbol{\omega}}_{des}, \tag{5.33}$$

where $\vec{\boldsymbol{\omega}}_{des} = \begin{bmatrix} \omega_{des_x} & \omega_{des_y} & \omega_{des_z} \end{bmatrix}^T$ is the desired spinning rate.

By using equation 5.6, the angular momentum error vector can be specified as

$$\vec{\boldsymbol{\varepsilon}}_H = {}^b\vec{\boldsymbol{H}}_{sat} - \|{}^b\vec{\boldsymbol{H}}_{des}\|\,{}^b\vec{\boldsymbol{N}}_{orbit}\,, \tag{5.34}$$

the angular momentum error around $\boldsymbol{Z}_b$-axis is modelled as

$$\varepsilon_{h_z} = H_{sat_z} - H_{des_z}\,, \tag{5.35}$$

and the angular rates error vector as

$$\vec{\boldsymbol{\varepsilon}}_\omega = \vec{\boldsymbol{\omega}}_{sat} - \vec{\boldsymbol{\omega}}_{des}\,. \tag{5.36}$$

The alignment of the angular momentum and orbit normal vectors can be achieved by first, $\vec{\boldsymbol{\varepsilon}}_H = \vec{\boldsymbol{0}}$, and second, $\varepsilon_{h_z} = 0$. The controller's performance can be improved if the redundant requirement $\varepsilon_{\omega_x} = \varepsilon_{\omega_y} = 0$ is added to the definition.

The final controller will have the form

$$\vec{\boldsymbol{D}}_{ctrl} = sat\left(-\frac{1}{\|{}^b\vec{\boldsymbol{B}}_{earth}\|^2}\vec{\mathcal{A}},\ D_{max}\right), \tag{5.37}$$

where

$$\vec{\mathcal{A}} = \vec{\boldsymbol{B}}_{earth} \times \left(\underbrace{K_{prec}\,\vec{\boldsymbol{\varepsilon}}_H}_{precession} + \underbrace{K_{spin}\,\varepsilon_{h_z}\begin{bmatrix}0\\0\\1\end{bmatrix}}_{spin} + \underbrace{K_{nut}\begin{bmatrix}1&0&0\\0&1&0\\0&0&0\end{bmatrix}\vec{\boldsymbol{\varepsilon}}_\omega}_{nutation} \right), \tag{5.38}$$

and K_α are positive feedback gains. For the experimental set-up the following feedback gains were chosen:

$$K_{prec} = 16 \times 10^{-3}\,, \tag{5.39}$$

$$K_{spin} = 2 \times 10^{-4}\,, \tag{5.40}$$

$$K_{nut} = 8 \times 10^{-3}\,. \tag{5.41}$$

Stability proof

By proposing the following Lyapunov function

$$V = \frac{1}{2}\left(K_{precc}\,\vec{\boldsymbol{\varepsilon}}_H^T\,\vec{\boldsymbol{\varepsilon}}_H + K_{spin}\,\varepsilon_{h_z}^2 + K_{nut}\,\vec{\boldsymbol{\varepsilon}}_\omega^T \begin{bmatrix}1&0&0\\0&1&0\\0&0&0\end{bmatrix}\vec{\boldsymbol{\varepsilon}}_\omega \right) \tag{5.42}$$

which is positive definite since $K_{precc} > 0$, $K_{spin} > 0$, $K_{nut} > 0$. The time derivative of V is approached by de Ruiter [8] as

$$\begin{aligned} \dot{V} &= \left(K_{precc}\,\vec{\boldsymbol{\varepsilon}}_H^T + K_{spin}\,\varepsilon_{h_z}\begin{bmatrix}0&0&1\end{bmatrix} + K_{nut}\,\vec{\boldsymbol{\varepsilon}}_\omega^T \begin{bmatrix}1&0&0\\0&1&0\\0&0&0\end{bmatrix}\right)\vec{\boldsymbol{\tau}}_{ctrl}\,, \\ &= \vec{\mathcal{A}}^T\,\vec{\boldsymbol{\tau}}_{ctrl}\,, \end{aligned} \tag{5.43}$$

and by substituting equation 5.37 in previous equation, it becomes

$$\begin{aligned}\dot{V} &= \vec{\mathcal{A}}^T\left(-\frac{1}{\|{}^b\vec{\boldsymbol{B}}_{earth}\|^2}\vec{\mathcal{A}}\right),\\ &= -\frac{1}{\|{}^b\vec{\boldsymbol{B}}_{earth}\|^2}\vec{\mathcal{A}}^T\vec{\mathcal{A}}.\end{aligned} \tag{5.44}$$

which under assumption of a bounded geomagnetic field; $B_1 < \|\vec{\boldsymbol{B}}_{earth}\| < B_2$, is negative semi-definite.

Minimal rotation rate

An important characteristic of this controller is the fact that a minimal rotation rate is required in order to achieve stability. Since the current baseline MoI has some issues that will be later addressed in the Chapter 6, this value was estimated by means of simulations

$$\omega_{CAM_{min}} \approx 3 \text{ deg}\cdot\text{s}^{-1}, \tag{5.45}$$

After that, an angular rate was also required as reference for NOM & CAM, the only restriction for the selection of this value is that ω_{CAM} must be always bigger that $\omega_{CAM_{min}}$. During the preliminary tests, this value was set to be

$$\omega_{CAM} = 10 \text{ deg}\cdot\text{s}^{-1}. \tag{5.46}$$

5.2.4. Linear Quadratic Regulator

By using the definition about the Linear Quadratic Regulator presented in Appendix C.3 on the linearised system obtained of Appendix C.1, the resulting feedback matrix

$$\mathbf{K}_{NOM} = \begin{bmatrix} 0.0236 & -0.0001 & -0.0001 & 1.5069 & -0.0033 & -0.0057 \\ -0.0001 & 0.0238 & 0.0001 & -0.0033 & 1.5156 & 0.0034 \\ -0.0001 & 0.0001 & 0.0240 & -0.0057 & 0.0034 & 1.5326 \end{bmatrix}, \tag{5.47}$$

was obtained, for which

$$\mathbf{Q} = diag\left([1,\ 1,\ 1,\ 4000,\ 4000,\ 4000]^T\right), \tag{5.48}$$

$$\mathbf{R} = diag\left([1000,\ 1000,\ 1000]^T\right), \tag{5.49}$$

where used as tuning matrices. It shall be stress out that the first guess for these tuning parameters was obtained by means of the well-known Bryson rule considering a maximal variation for each parameter of $Q_{1:3} = \frac{1}{{q_i}_{max}{}^2} = 1, Q_{4:6} = \frac{1}{{\omega_{max}}^2} = \frac{1}{0.0174^2} \approx 3282$ and $R_{1:3} = \frac{1}{{\tau_{RW}}_{max}{}^2} = \frac{1}{0.0119^2} \approx 6984$. After that, the weight of $\mathbf{R}$ matrix was reduced in order not to saturate the wheels.

The stability proof, and stability margins are described in Appendix C.3.1.

5.2.5. Magnetic unloading of the reaction wheels

The external disturbances analysed in Chapter 3 induce an accumulation of angular momentum in the reaction wheels along the orbit. This accumulation can cause instability of the satellite when performing attitude manoeuvres, therefore the wheels shall be constantly unloaded to avoid this issue.

For this mission the magnetic torquers can be used to remove the excess of angular momentum, using the formulation proposed by Sidi [42], which is

$$\vec{\boldsymbol{\tau}} = -K_{unload}\left(\vec{\boldsymbol{H}}_{RW} - \vec{\boldsymbol{H}}_{nom}\right) = -K_{unload}\,\Delta\vec{\boldsymbol{H}} \tag{5.50}$$

where $\vec{\boldsymbol{H}}_{RW}$ is the wheel's momentum vector and $\vec{\boldsymbol{H}}_{nom}$ is the wheel's nominal momentum vec-

tor; thus, $\Delta\vec{\boldsymbol{H}}$ can be seen as the excess of momentum to be removed. If equation 4.4 is then substituted into equation 5.50, this yields to

$$-K_{unload}\,\Delta\vec{\boldsymbol{H}} = \vec{\boldsymbol{D}}_{ctrl} \times \vec{\boldsymbol{B}}_{earth}\,, \tag{5.51}$$

and by pre-multiplying both sides by $\vec{\boldsymbol{B}}_{earth}$ using cross product, it becomes

$$\vec{\boldsymbol{B}}_{earth} \times \left(-K_{unload}\,\Delta\vec{\boldsymbol{H}}\right) = \vec{\boldsymbol{B}}_{earth} \times \left(\vec{\boldsymbol{D}}_{ctrl} \times \vec{\boldsymbol{B}}_{earth}\right), \tag{5.52}$$

$$= B_{earth}^2\,\vec{\boldsymbol{D}}_{ctrl} - \vec{\boldsymbol{B}}_{earth}(\vec{\boldsymbol{D}}_{ctrl} \cdot \vec{\boldsymbol{B}}_{earth})\,. \tag{5.53}$$

If in equation 5.52 it is assumed that control dipole $\vec{\boldsymbol{D}}_{ctrl}$ is perpendicular to the earth's magnetic field $\vec{\boldsymbol{B}}_{earth}$, the dot product $\vec{\boldsymbol{D}}_{ctrl} \cdot \vec{\boldsymbol{B}}_{earth}$ is zeroed, therefore this results in

$$\vec{\boldsymbol{D}}_{ctrl} = -\frac{K_{unload}}{\|^b\vec{\boldsymbol{B}}_{earth}\|^2}\left(\vec{\boldsymbol{B}}_{earth} \times \Delta\vec{\boldsymbol{H}}\right). \tag{5.54}$$

or a more explicit form

$$\begin{bmatrix} D_{ctrl_x} \\ D_{ctrl_y} \\ D_{ctrl_z} \end{bmatrix} = -\frac{K_{unload}}{\|^b\vec{\boldsymbol{B}}_{earth}\|^2} \begin{bmatrix} B_{earth_y}\,\Delta H_z - B_{earth_z}\,\Delta H_y \\ B_{earth_z}\,\Delta H_x - B_{earth_x}\,\Delta H_z \\ B_{earth_x}\,\Delta H_y - B_{earth_y}\,\Delta H_x \end{bmatrix}. \tag{5.55}$$

From previous equation, if the angular momentum vector to be dumped is parallel to the Earth's magnetic field, no torque can be produced to counteract it. This fact would be a problem for equatorial orbits, but since the orbit envelope of this project is a near-polar orbit, the validity of this control law can be applied to S2TEP.

The value of the unloading gain K_{unload} is usually determined by the "trial-and-error" method [42]. For application purposes of this work, the nominal angular momentum or the RWs was chosen to be zero ($\vec{\boldsymbol{H}}_{nom} = \begin{bmatrix}0 & 0 & 0\end{bmatrix}^T$) and the corresponding feedback gain is

$$K_{unload} = 0.07\,. \tag{5.56}$$

6

SIMULATIONS AND RESULTS

A general overview of the simulation model is given to the reader in this chapter; this includes a brief introduction to every function employed for the simulation of the ADCS components. Subsequently, some simulation scenarios were defined given its importance for the study of the modes performance. For every scenario, different parameters are varied in order to study the impact they may have in the overall performance of control system. At the end, some results are given for nominal and non-nominal condition, from which some design issues will be clarified.

6.1. SIMULATION MODEL

Following the design methodology presented at the beginning of this work (see Fig. 1.2), the resulting simulation model, after the implementation of the analytical definitions described along this thesis, is shown in Fig. 6.1. The model was constructed in a *Matlab-Simulink* environment.

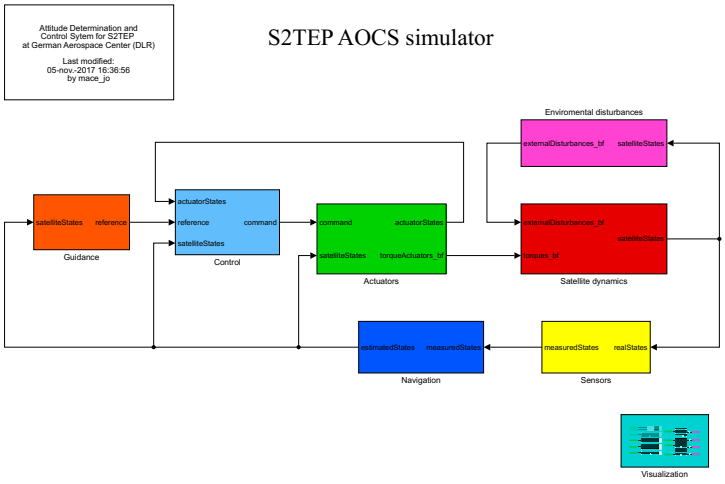

Figure 6.1: *Simulink* model (upper level).

Fig. 6.1 displays the upper level of the simulator, which is organized in the following order:

- `Guidance`: This block includes three main functions:

  - `DCM generation`: The reference attitude DCM is generated by means of the definitions presented in Section 2.2. The orbital velocity, Nadir and Sun vectors are required as inputs here.
  - `Quaternion calculation`: By employing the attitude DCM and the definitions from Section A.3, the reference attitude quaternion is generated here. The original script used for this transformation induced a singularity for rotations at -90° and 270°; therefore, it was modified to cope with rotations between -360° and 360° (the formal analytical definition of a quaternion lies within these limits).
  - `Angular rates calculation`: By using the attitude quaternion and its derivative, the reference angular rates are calculate by this function (see definition A.23).
  - `Mode selection`: This block uses as inputs the angular rates, the orbit normal vector and the attitude quaternion for the calculation of the switching commands between modes. As result it produces a selected pointing mode and a reference trajectory for SFM & CAM. The data from Table 2.1 is important for the understanding of these autonomous transitions.

- `Control`: This block includes three main sub-components:
  - `DTM controller`: This model contains the definitions for the detumbling controllers from Section 5.2.2. The magnitude and direction of the magnetic field is required for the calculations, while a commanded magnetic dipole is obtained as output.
  - `CAM & SFM controller`: The spin, precession and nutation controller from Section 5.2.3 is coded within this block. The satellite's angular rate, magnetic field and orbit normal vectors are the required inputs for the calculation of a commanded dipole.
  - `NOM controller`: This script contains the definitions for the nominal pointing mode controllers, which are:
    - `LQR controller`: The LQR controller from Sections 5.2.4 and C.3. It uses the attitude quaternion and angular rates from both the `Navigation` and `Guidance` blocks, which are the real values and the reference signal, respectively. These values are used for the calculation of the system errors and then they are multiplied by the feedback gain in order to obtain the commanded RWs torque.
    - `Magnetic unloading`: The angular momentum unloading controller from Section 5.2.5 is embedded here, for which the magnetic field vector and the current RWs angular momentum are the sources of information, as result it provides a commanded magnetic dipole.

- `Actuators`: Three main sub-block are modelled in this part:
  - `Reaction wheel triad`: This block contains an array of three reaction wheels located in every principal axis of the body frame. Each of these wheels uses a commanded torque as reference, and it provides an achieved torque as result. The formulation from Section 4.1.2 was coded here with the aim of modelling the RW dynamics, and some important parameters like angular momentum, angular rate, armature voltage and current, and electrical power are stored in real time for its subsequent analysis. The real characteristics of rhe wheels can be retrieved from Table 4.5.
  - `Magnetic torquer triad`: An array of three magnetic torquers is constructed within this block by employing the definitions from Section 4.1.1 and the parameters from Table 4.3. It receives a commanded dipole and the geomagnetic field vector as inputs, and provides an achieved torque as result. The duty cycle of the MTQ can be also be modified within this block.

  - `Internal disturbances`: At this moment, no internal disturbances have been considered for the ADCS design; however, if they want to be added in the future, they will be located in this part.

- `Satellite dynamics`: Two functions are contained within this block:
  - `Attitude dynamics`: This block uses as input the RWs commanded torques, the external torques generated by the environmental models and the physical parameters of the satellite for the calculation of the current attitude quaternion and angular rates from equations presented in Section 5.1.2.
  - `Orbit dynamics`: This block uses commanded force (not included in this satellite), disturbance forces, the satellite parameters and the attitude quaternion for the calculation of the position and orbital velocity from formulation 5.1.1.
- `Environmental disturbances`: All the disturbance torques and forces are calculated within this block, for which four main sources are studied:
  - `Gravity gradient`: The disturbance torque produced by the gravity gradient is calculated from the model presented in Section 3.1.1. The position of the satellite is the only required input for this purpose.
  - `Magnetic field`: The torque produced by the magnetic field is estimated within this block by evaluating the satellite position in equations from Section 3.1.2.
  - `Solar radiation pressure`: The estimation of the solar disturbances is obtained from the Sun vector, the eclipse flag and the definitions from Section 3.1.3.
  - `Atmospheric drag`: By using the orbit velocity, atmospheric density and the models from Section 3.1.4, the value of the atmospheric disturbances is computed in this part of the model.
- `Sensors`: In order to model the behaviour of the attitude determination hardware, this model was divided into two different functions:
  - `Real measurements`: Additionally to the states vector produced by the *Satellite dynamics* block, the magnetic field and Sun vectors are also calculated within this block. Firstly, the current Julian and Modified Julian dates were obtained using definitions from Appendix B, secondly, the magnetic field vector is obtained by applying definition 3.4, thirdly, the Sun is obtained from the satellite position and the position of the Earth with respect to the Sun (see B.4).
  - `Sensors effects`: Some effects were modelled for each of the sensor presented in Chapter 4. They are:
    - `GPS`: Bias and noise using the real position and orbit velocity and the parameters from Table 4.10.
    - `Star tracker`: Bias and noise using the real attitude quaternion and the parameters from Table 4.9.
    - `Gyroscope`: Random walk and noise using the real angular rate and the parameters from Table 4.6.
    - `Sun sensor`:Bias and noise using the real Sun vector and the parameters from Table 4.8.
    - `Magnetometer`: Bias and noise using the real geomagnetic field and the parameters from table 4.7.

- `Navigation`: Two functions were created within this block.
  - `Kalman filter`: At this point of the project the behaviour of a Kalman filter is only simulated by amplifying the attitude error for SFM and CAM (since STR is not available for these modes).
  - `Attitude transformations`: Some useful attitude transformations are computed within this block, which are mainly employed to change the measurements from body to inertial coordinates or vice versa, other parameters are also calculated in real time, like:
    - Eclipse flag
    - Nadir vector
    - Orbit normal vector

6.2. MONTE-CARLO CAMPAIGN

Since S2TEP is currently at the middle of phase B, several parameters of the satellite cannot be fully determined until some some validation tests are performed before launch. For that reason, it is important to define some boundaries for which the pointing accuracy of the ADCS is not compromised.

For the validation of baseline ADCS, the so-called Monte-Carlo method was chosen because it allows to study the behaviour of a simulation model under different initial conditions. Hence, for every pointing mode, the controller robustness will be assessed by both adding uncertainties to the most critical parameters of the satellite and simulating different environmental conditions. Four main simulation scenarios have been established for each of the pointing modes from Section 2. The critical parameters to be studied in every simulation scenario will be explained in the subsequent paragraphs.

For every simulation scenario, the MoI matrix will be varied, an uncertainty in this parameter is particularity interesting since it directly modifies the dynamics of the satellite, and given that this parameter was used for the analytical definitions of the control laws and consequently for the calculation of the feedback gains, it is important to study how much a variation will degrade (or improve) the overall performance of the ADCS.

The magnitude and direction of the magnetic dipole cannot be known before the satellite is built, and since a worst-case scenario was defined in Chapter 3, it is only interesting to study the impact of a change in the direction.

The position of the CoG plays a very important role in the estimation of the atmospheric drag torque. A deviation in this parameter will affect the magnitude of the atmospheric torque in every axis.

Given that the geomagnetic field has a non-linear distribution according to the satellite's position in the orbit, as well as its important role for the generation of the command torques during the correction manoeuvres, different rotations of the ECEF frame w.r.t. the ECI frame will be simulated by modifying initial date.

A randomly-generated true anomaly value allows to study different phenomena according to the simulation scenario:

- 1. It simulates different injection points in the orbit for DTM.
- 2. For CAM, it simulates different points where the transition from detumbling is triggered.
- 3. Similarly, for NOM it allows to simulate the transition anywhere in the orbit, as well as different initial reference quaternions for the sub-modes (NPM, SPM, IPM or GPT).

- 4. For SFM, it allows to simulate a failure occurrence at any point in the orbit.

The variation ranges and its respective variation ranges, as well as some other remarks are presented in Table 6.1.

Parameter	Variation range	Distribution	Remarks
Moment of inertia matrix	$\Delta \boldsymbol{J}_{sat} \in [-20,\ 20]\,\%$	Gaussian	Including off-diagonal elements
Satellite magnetic dipole	$D_{sat_x} \in [-1,\ 1]$ $D_{sat_y} \in [-1,\ 1]$ $D_{sat_z} \in [-1,\ 1]$	Uniform	$\vec{\boldsymbol{D}}_{sat}$ is normalized and multiplied by 1 A$\cdot$ m^2 since only a random direction is required
center of gravity	$\Delta \mathrm{CoG} \in [-20,\ 20]\,\%$	Uniform	–
Rotation of ECEF w.r.t. ECI	$\Delta t \in [0,\ 24]$hours	Uniform	Random minutes and seconds are also included.
True anomaly	$\nu \in [0,\ 360]$ deg	Uniform	–

Table 6.1: Simulation parameters to be varied for every simulation scenario.

In the following sections, other particular simulation considerations will be pointed out for every simulation mode.

Scenario 1 (DTM): This scenario simulates the initialization of the ADCS after the separation from the launcher. Since the worst-case scenario separation rate is known, only a variation in the direction will be set as initial condition. The result from the MC campaign will hence allow the EPS team to have a worst-case estimation for the detumbling time.

Parameter	Variation range	Distribution	Remarks
Launcher separation rate	$\omega_{0_x} \in [-1,\ 1]$ $\omega_{0_y} \in [-1,\ 1]$ $\omega_{0_z} \in [-1,\ 1]$	Uniform	$\vec{\boldsymbol{\omega}}_0$ is normalized and multiplied by 10 deg$\cdot$s^{-1} since only a random direction is required

Table 6.2: Simulation parameters to be varied for DTM.

Scenario 2 (CAM): This simulation scenario allows to study the transition from DTM and the performance of CAM during early orbit phase. For this analysis, the worst-case scenario angular rate from Table 2.1 is simulated for different directions. From this MC scenario, the required time for reorienting the angular momentum can be analysed by the TCS team in order to know if the radiators will have enough time to dissipate the heat generated by the satellite.

Parameter	Variation range	Distribution	Remarks
Initial angular rate	$\omega_{0_x} \in [-1,\ 1]$ $\omega_{0_y} \in [-1,\ 1]$ $\omega_{0_z} \in [-1,\ 1]$	Uniform	$\vec{\boldsymbol{\omega}}_0$ is normalized and multiplied by $2\omega_{orbit}$ since only a random direction is required

Table 6.3: Simulation parameters to be varied for CAM.

Scenario 3 (NOM): Since this is perhaps the most interesting mode for the payload activities, a detailed analysis of the pointing performance shall be retrieved from this simulation. For this

scenario, the initial attitude quaternion will formulated in terms of randomly generated Euler angles. In addition that, the initial angular rate will be always initialized with the maximal allowed value proposed in Table 2.1 and random directions.

Not only the pointing accuracy is important for this mode but also the power demanded by the wheels at the beginning of the re-orientation manoeuvres. The maximal angular momentum stored by the wheels can also be retrieved from this analysis.

Parameter	Variation range	Distribution	Remarks
Initial quaternion	$\phi_0 \in [-360, 360]$ deg $\theta_0 \in [-360, 360]$ deg $\psi_0 \in [-360, 360]$ deg	Uniform	ϕ_0, θ_0 and ψ_0 random values are used to calculate $\mathbf{q}_0$
Initial angular rate	$\omega_{0_x} \in [-1, 1]$ $\omega_{0_y} \in [-1, 1]$ $\omega_{0_z} \in [-1, 1]$	Uniform	$\vec{\omega}_0$ is normalized and multiplied by $2\omega_{orbit}$ since only a random direction is required

Table 6.4: Simulation parameters to be varied for NOM.

Scenario 4 (SFM): Strictly speaking, SFM has the same formulation for both control laws and hardware requirements; as for CAM. The main difference lies however in the fact that both modes are modelling two completely different scenarios. SFM's primary goal is to stabilize the satellite under any initial conditions; this means, it covers the requirements of all three previous modes (see Table 6.5). They are, the initial quaternion (transition from any mode), the initial angular rate with a maximal magnitude of 10 deg$\cdot$s^{-1} and random direction (simulating a transition from any mode) and different values stored angular momentum in the wheels (transition from NOM).

From this simulation, the maximal precession angle, as well as the angular rate norm will be retrieved after the Monte-Carlo campaign.

Parameter	Variation range	Distribution	Remarks
Initial quaternion	$\phi_0 \in [-360, 360]$ deg $\theta_0 \in [-360, 360]$ deg $\psi_0 \in [-360, 360]$ deg	Uniform	ϕ_0, θ_0 and ψ_0 random values are used to calculate $\mathbf{q}_0$
Initial angular rate	$\omega_{0_x} \in [-1, 1]$ $\omega_{0_y} \in [-1, 1]$ $\omega_{0_z} \in [-1, 1]$	Uniform	$\vec{\omega}_0$ is normalized and multiplied by 10 deg$\cdot$s^{-1} since only a random direction is required
Angular momentum of the wheels	$H_{RW_x} \in [-60, 60]$ mN$\cdot$m$\cdot$s $H_{RW_y} \in [-60, 60]$ mN$\cdot$m$\cdot$s $H_{RW_z} \in [-60, 60]$ mN$\cdot$m$\cdot$s	Uniform	–

Table 6.5: Simulation parameters to be varied for NOM.

Besides the simulation scenarios, other parameters can be varied for any Monte-Carlo run, such as:

- Number of runs.
- Initial set (in case a failed simulation is desired to be reproduced again).
- Used states:

  - Real states (as extracted from the `Satellite dynamics` block).
  - Estimated states (with the all the effects produced by the sensors).
- Error types:
  - Nominal case (parameter used for the sizing procedures).
  - Worst case (using the worst-case uncertainty).
  - Random (generated using the uncertainties ranges).
- Seeds for the noise generation:
  - Predefined (these seeds will always produce the same noise profile).
  - Randomly generated (the seeds will be generated using the computer's current date and hour; therefore, the noise profile will always be different from one simulation to another).

6.3. RESULTS ANALYSIS

The results were grouped into two sections. First, those for every pointing mode under nominal conditions, which are presented in the next subsection. And secondly, those obtained from the MC campaign for 100 runs (using a variation in the nominal parameters as previously explained) are gathered together in a single plot for every simulation scenario.

It shall be remarked that during the second half of September 2017, there was a second update in the satellite and orbit parameters, consequently these parameters are shown in Table 6.6.

Parameter	**Value**	**Units**
	SATELLITE	
Mass (m_{sat})	25.878	kg
Moment of inertia ($\boldsymbol{J}_{sat}$)	$\begin{bmatrix} 1.673 & 0.014 & -0.023 \\ 0.014 & 1.603 & -0.013 \\ -0.023 & -0.013 & 1.569 \end{bmatrix}$	$\mathrm{kg \cdot m^{-1}}$
Drag coefficient (C_D)	2.5	-
Magnetic dipole (D_{sat})	1	$\mathrm{A \cdot m^2}$
Dimensions	$0.6 \times 0.6 \times 0.6$	m
Center of gravity (w.r.t. MCF)	$\begin{bmatrix} 0.3 & 0.3 & 0.182 \end{bmatrix}^T$	m
	ENVIRONMENT	
Atmospheric density (ρ_{atm})	3.04×10^{-12}	$\mathrm{kg \cdot m^{-3}}$
Solar activity (JB2006 model)	F10.7 = 250 (High-long term)	-
	ORBIT (SS-LEO)	
Altitude (h)	500	km
Eccentricity (e)	0	deg
Inclination (i)	97.39	deg
RAAN (Ω)	190	deg
Argument of perigee (ω)	0	deg

Table 6.6: Parameters used as nominal scenario.

6.3.1. Nominal scenario

DTM: The trajectory of the angular rates during the detumbling phase under nominal conditions is depicted in Fig. 6.2, and consequently the required magnetic dipole for this mode is presented in Fig. D.1. For a nominal scenario, the detumbling phase would take around half an orbit to reach the requirements defined in Table 2.1.

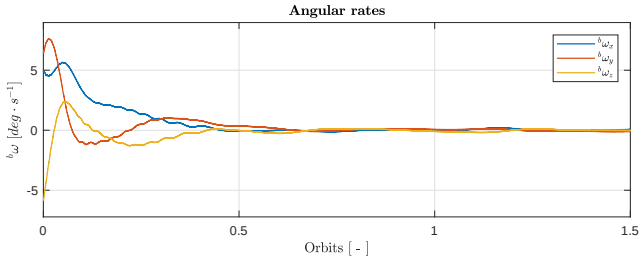

Figure 6.2: DTM: States in nominal conditions.

CAM: According to Sidi [42], any spin-stabilized satellite will spin around its axis with the maximal moment of inertia. During the definition of the control law for this mode, the requirement of having the maximal moment of inertia around the $\vec{Z}_b$-axis was imposed to the structural designers. It should be pointed out that this requirement has not yet been taken into account (as seen in Table 6.6) for the distribution of the internal components of the satellite.

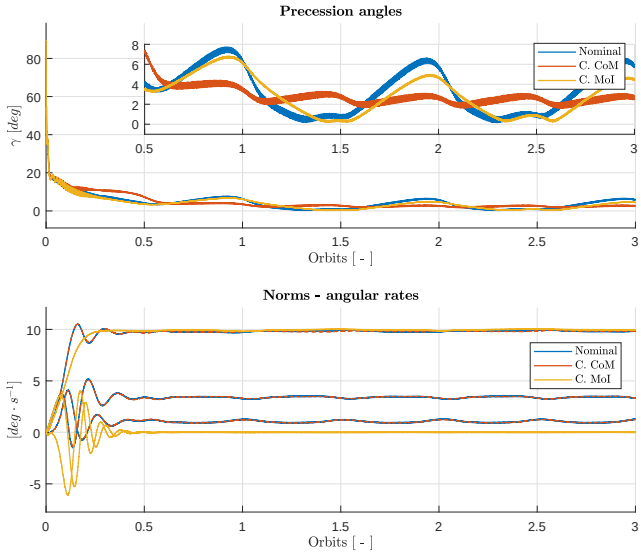

Figure 6.3: CAM: States in nominal conditions.

The results from three simulations with different considerations are depicted in Fig. 6.3. The considerations are:

- **Blue**: The nominal parameters of Table 6.6 were used for this first simulation. Since the pointing accuracy did not accomplish the requirements (given that ε_γ> 5 deg, ε_{ω_x} > 0.1 deg · s^{-1} and ε_{ω_y} > 0.1 deg · s^{-1}), an analysis to determine the causes of this issue was conducted. The respective MTQs response is presented in Fig. D.3.

- **Yellow:** For this new simulation, the MoI matrix in principal coordinates was calculated by employing the procedure presented in Section B.5.1, which is

$$\boldsymbol{J}_{sat} = \begin{bmatrix} 1.5545 & 0 & 0 \\ 0 & 1.60205 & 0 \\ 0 & 0 & 1.68138 \end{bmatrix} \text{kg}\cdot\text{m}^{-1}. \tag{6.1}$$

  Now, by assuming that this matrix was the real MoI of the satellite (which would mean that the principal axes were aligned with the body frame axes), the results presented in yellow lines were obtained; which allows to state some conclusions for the further development of the mission. Unless the maximal MoI is placed in the $\boldsymbol{Z}_{\mathcal{B}}$-axis and the off-diagonal terms are keep as close as possible to zero, the components ε_{ω_x} and ε_{ω_y} will not be zeroed. Under this assumption the precession error still does not accomplish the pointing requirements.

- **Dashed-orange:** For this new simulation all nominal parameters from Table 6.3 and a CoG located at the geometrical center of the satellite

$$\text{CoG} = \begin{bmatrix} 0.3 & 0.3 & 0.3 \end{bmatrix}^T \text{m}, \tag{6.2}$$

  is assumed; the obtained results are shown in dashed-orange lines. Now, it can be proved that the precession angle slowly tends to zero even if the MoI is not the required one (still the spinning dynamics issue should be solved with the MoI considerations of previous analysis). Since the current CoG in $\boldsymbol{Z}_{\mathcal{B}}$-axis is located 8.1 cm below the geometrical center, the precession error is highly influenced by the disturbance torques. For further development of the mission, the CoG should be keep as close as possible to the geometrical center. Otherwise, a RW should be used to reorient the angular momentum vector since the pointing accuracy cannot be achieved with the current parameters and baseline control law.

NOM: The selected sub-mode for this simulation was NPM. The attitude quaternion, as well as the angular rates, represented in the body frame are depicted in Fig. 6.4, while the MTQs dipole and RWs angular momentum associated to this simulation are presented in Fig. D.2. For nominal conditions, the pointing accuracy was always kept below 0.2 deg, while the wheels are running around one third of its total angular momentum capacity. Which indeed, accomplishes the requirements.

SFM: The same procedure presented for CAM is assumed for the SFM simulations. Consequently, the results are shown in Fig. 6.5, and the respective control dipole, as well as the evolution of the stored RWs' angular momentum for nominal conditions (using parameters of Table 6.6) are shown in Fig. D.4.

6.3.2. Monte-Carlo campaign

In order to have a representative set of results out of the simulations, 100 runs were considered for every scenario. Consequently, uncertainties were introduced in the satellite parameters according to the specification of Tables 6.1, 6.2, 6.3, 6.4 and 6.5.

Trajectories observed in Fig. 6.6 represent the evolution of the angular rates norms during the detumbling phase. Base on this information, it is possible to conclude that for the current baseline design ($D_{MTQ} = 10\text{A}\cdot\text{m}^2$ and control law 5.23) the fully de-spin can be achieved at around 0.5 orbits ($\approx$ 47 min). Therefore, the requirements of the EPS are fully accomplished. In terms of stability, and as proven in the respective section (5.2.2), no unstable configuration has been observed.

For the MC campaign in CAM, the MoI of equation 6.1 and the CoG of equation 6.2 are now

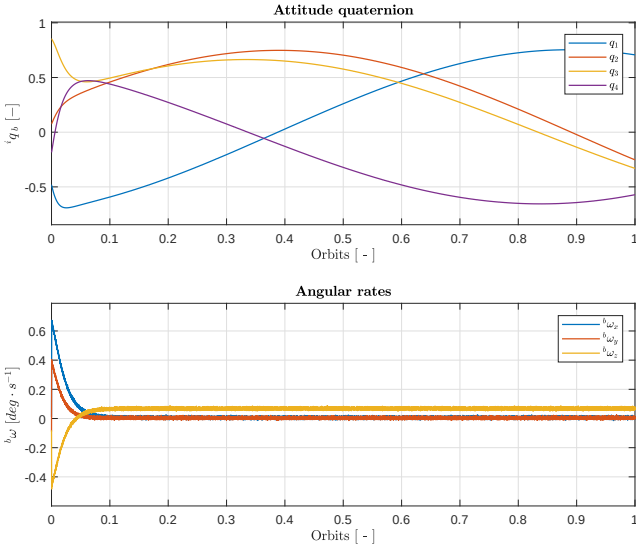

Figure 6.4: NOM: States in nominal conditions.

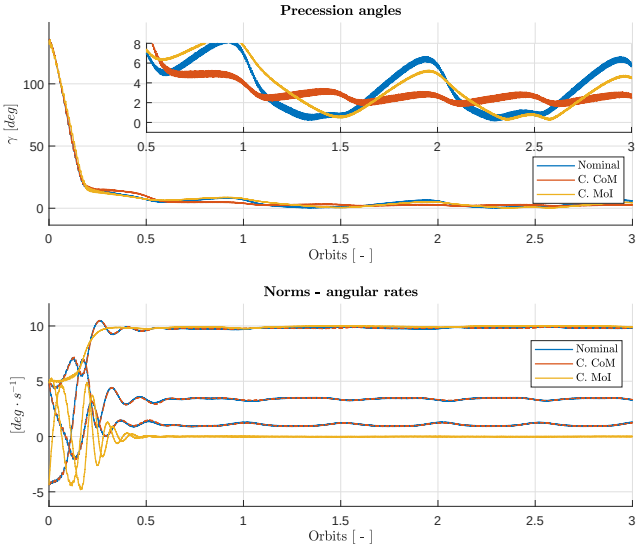

Figure 6.5: SFM: States in nominal conditions.

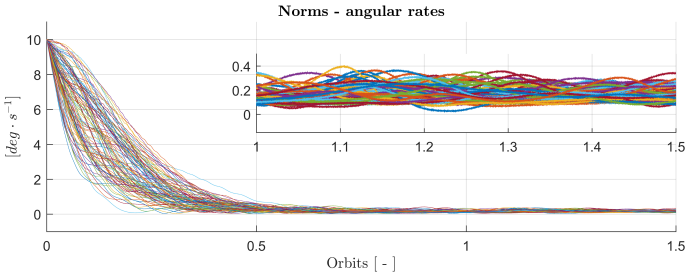

Figure 6.6: Monte-Carlo simulation for 100 runs: DTM.

considered as baseline parameters. The addition of uncertainties is considered as presented in Table 6.1, the MoI in J_z was constrained to be always the maximal one independently of the value of J_x and J_x, and the uncertainties in the off-diagonal elements were considered to have a variation of 2% at most (w.r.t the maximal MoI). The results are consequently shown in Fig. 6.7, regarding the precession angle, the requirements are accomplished for 97% of the cases, the cases for which the pointing error was bigger that 5 deg were those where the CoG in $\boldsymbol{Z}_b$ was deviated almost 6 cm from the geometrical center. Not further conclusions can be given about the spinning control since the dynamics of this controller are highly dependent on the MoI. It shall however be remarked, that a specific tuning might solve this issue.

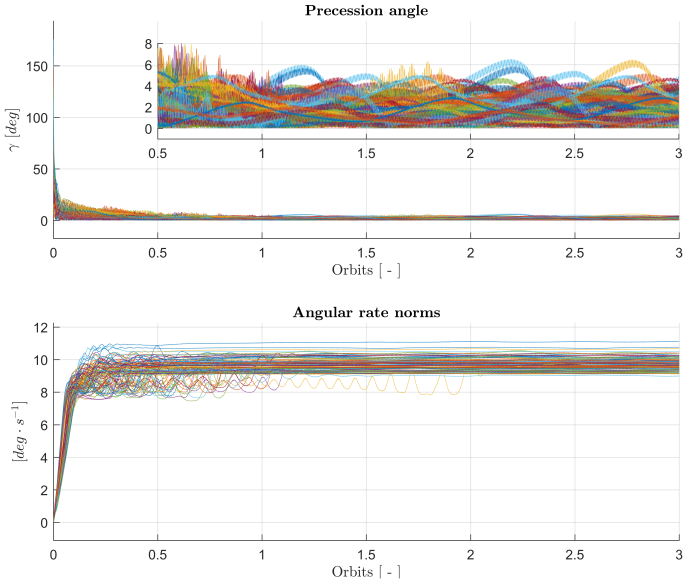

Figure 6.7: Monte-Carlo simulation for 100 runs: CAM.

For NOM, the pointing performance retrieved from the Monte-Carlo simulations is plot in Fig. 6.8. The upper plot contains the Euler angles errors, while the angular rates errors can be found at the bottom. The uncertainties did not affect the performance of the controller since the error is always kept below 1 deg. The plot for RWs power and angular momentum are, respectively, shown in Figs. D.5 and D.6. The required power at the beginning of the nominal pointing manoeuvres does not exceed 5 W given the limitations established by the EPS (max. 1 A). On the other hand, the RWs are working, in a worst-case scenario, at one third of its total capacity.

Finally, for SFM the precession angles and angular rates norms for every simulation are plot in Fig. 6.9. The restriction stated for CAM are taken also taken into account for this analysis. In terms of precession error, the probability of failure is also 3%, and since this mode shares the controller with CAM, the same causes were identified.

It shall only be remarked, that the evolution of the RWs angular momentum over the time does not compromise the performance of this mode, since the viscous friction coefficient slowly decelerates the rotor, the excess of angular momentum is slowly eliminated by the magnetic torquers.

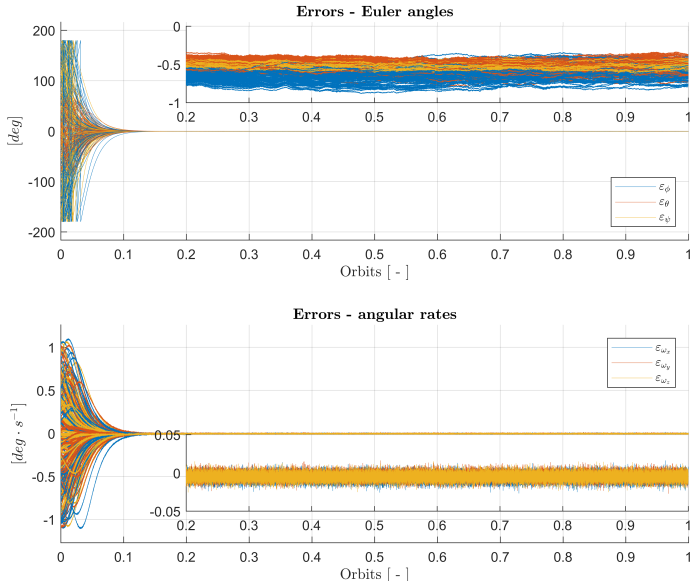

Figure 6.8: Monte-Carlo simulation for 100 runs: NOM (NPM).

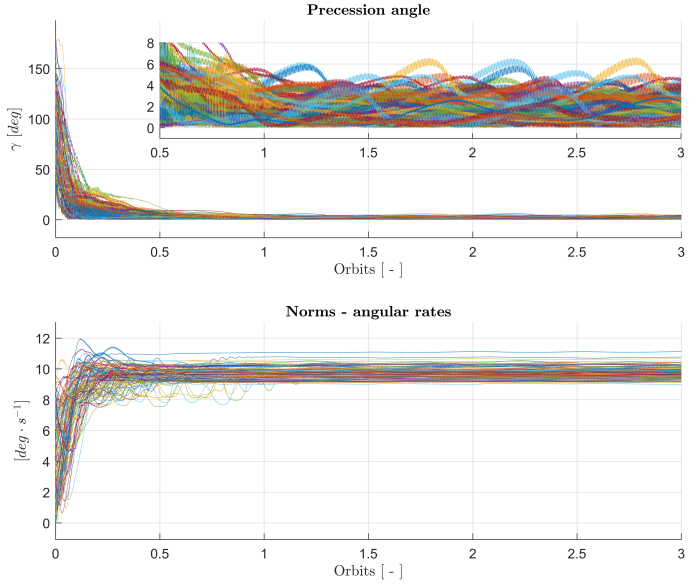

Figure 6.9: Monte-Carlo simulation for 100 runs: SFM.

7

CONCLUSION

7.1. CONCLUSION

This thesis describes the attitude control system developed for the S2TEP mission during phases A/B, which can potentially be used as final solution at the end of phase C. The baseline design presented in this work was intended to be maintained as generic as possible since many parameters of the satellite are, at this moment, not fully established; its value will be only known after performing some validation tests on the satellite before launch.

Based on the requirements collected from EPS, structure, TCS, and payload, four main pointing modes have been established in order to fulfil the mission requirements: detumbling, coarse acquisition, nominal mode and safe mode. For the nominal mode, four sub-modes have also been defined with the aim of having different pointing conditions for the scientific activities: nadir pointing, inertial pointing, Sun pointing and ground point tracking.

A detailed reconstruction of the environmental disturbance torques was performed for all the sub-modes of NOM (except for GPT since this sub-mode was not considered in the initial design) by simulating two cases at the limits of the orbit envelope (500 and 650 km). In the same way, the worst-case scenario for the whole mission (also including CAM, SFM and DTM) was calculated by means of a generalization in formulas from Chapter 3.

The attitude control hardware was sized based on the results from Chapter 3. Consequently, the minimal capabilities of both the MTQs and RWs were discussed with the procurements department, which resulted in a choice of 10 $A \cdot m^2$ and 60 $mN \cdot m \cdot s$, respectively. On the other hand, an analysis to determine the minimal requirements for the attitude determination hardware was also carried out in this work. The final choice was therefore made using the obtained results as well as the pre-launch experience from *Eu:CROPIS* [20]. For some of the selected sensors, an in orbit-calibration process is planned in order to reduce the effect of noise and bias.

In regards to the control laws, the following behaviour has been observed:

- For DTM, no issues were identified under nominal and non-nominal conditions, in both cases the pointing requirements were accomplished.
- For NOM, on the other hand, the performance was slightly compromised after the addition of uncertainties, the pointing error was 0.3 ° under nominal conditions and 0.7 ° after the addition of the uncertainties. In both cases the pointing performance requirements were accomplished.
- For CAM & SFM, under nominal conditions and with the current MoI and CoG, the requirements were not accomplished. Two main causes were identified:

- **CoG**: the current location of the center of gravity in the $\vec{Z}^{\mathcal{B}}$-axis is no very convenient for the precession dynamics (almost 30% variation w.r.t. the geometrical center). The more this parameter is deviated from the geometrical center, the less stable will the precession angle will be.
- **MoI**: For the spinning dynamics, a diagonal MoI matrix with the largest moment of inertia in $\boldsymbol{Z}_{\mathcal{B}}$ was assumed for the controller definition, and since the current MoI has its maximal value in $\boldsymbol{X}_{\mathcal{B}}$-axis, the controller does not perform as expected. After a re-definition of both the baseline MoI and CoG, the pointing performance for nominal conditions was achieved and for 97% of the cases under non-nominal conditions.

After analysing the results of the MC camping, it can be concluded that a deviation in one or more of the baseline parameters will not significantly compromise the stability of the satellite. It shall however, be mentioned that a specific tuning for every controller must be performed once the final satellite parameters are known.

The Monte-Carlo simulation allowed to understand how the addition of uncertainties in some of the parameters of the satellite affects the performance of the different control laws. Further recommendation will be hence discussed in the next section by recalling these results.

7.2. RECOMMENDATIONS

7.2.1. DTM

The only further recommendation for the DTM is whether the measurements of the gyroscope will be used for the final implementation given the capabilities of the EPS. The advantages and disadvantages of each solution are:

- The typical bang-bang B-dot formulation for high angular rates, and non-saturated B-dot controller for low angular rates was defined as first baseline solution. The main advantage is that it only requires the measurements of the geomagnetic field's magnitude and direction for the calculation of the correction commands; however, it usually requires a longer detumbling time when compared to the next solution.
- A B-dot controller with angular rate feedback is used as second baseline solution, which yields to a shorter and thus more stable detumbling phase. However, in terms of power consumption, the gyroscope is the most demanding sensor since it can drain as much power as a single magnetic torquer.

Since the available power for the detumbling phase is limited by the EPS, a trade-off between consumption and maximal detumbling time can be obtained by running many simulations using the Monte-Carlo set-up proposed in this work. Which can be used to choose the best solutions in terms of power consumption.

7.2.2. CAM/SFM

This mode is very sensitive to changes in the MoI and CoG; therefore, the following recommendations should be taken into account in phase C:

- The moment of inertia J_{zz} should be the largest in order to have stable spinning satellite. The bigger the difference when compared to J_{xx} and J_{yy}, the more accurate the spin control will be.

- The off-diagonal elements will also affect the nominal performance of this mode, therefore they should be kept as close as possible to zero. A non-zero off-diagonal (miss alignment of the body frame axes) element will induce a non-desired angular rate in $\boldsymbol{X}_{\mathcal{B}}$- and $\boldsymbol{Y}_{\mathcal{B}}$ -axes.
- The CoG should be keep as close as possible to the geometric center of the satellite. The bigger the difference, the largest the impact in the precession dynamics. This issue can also be solved by using one of the RWs for the angular momentum reorientation while the spin is controlled with solely magnetic actuation.

The orbit normal vector in the body frame is a requirement for this mode. And since it can be directly computed from the velocity and position vectors, the GPS measurements are a requirement for both CAM/SFM.

7.2.3. NOM

The results of the MC analysis are important to determine the feasibility of switching to the NOM mode right after the detumbling phase. Since now the maximal required power to reorient the satellite at the beginning of the nominal mode is know, this value can be added to the maximal estimated power consumption during DTM which will allow to determine if the EPS can provide enough power for this transition.

In order not to saturate the wheels, and therefore not to lose attitude control, when switching to this mode, the satellite's angular rate should have a small value. For an scenario where all the satellite's moment of inertia needs to be stored in a single wheel, the maximal angular rate for the saturation of the wheel was calculated to be 1.7 $\mathrm{deg}\cdot\mathrm{s}^{-1}$.

7.2.4. Hardware

- Even though, only the measurements of a gyroscope are required for the attitude determination. The selected IMU also provides acceleration and inclination. These measurements can be mixed with the lectures of other sensors to improve the attitude determination accuracy for non-nominal modes.

A

MATHEMATICS

This section contains all the mathematical definitions necessary to understand the content presented in along this work.

A.1. VECTORS

Dot product

The dot product (or also called inner product or scalar product) between two vectors is defined as

$$\vec{u}\cdot\vec{v} = \vec{v}\cdot\vec{u} = \vec{u}^T\vec{v} = \vec{v}^T\vec{u} = \sum_{i=1}^{n} u_i\, v_i\,, \tag{A.1}$$

the dot product is often used to verify the orthogonality between vectors, this means, if the result is equal to zero; the vectors are said to be orthogonal.

Norm

The norm (or length) of a vector can be obtained by means of the Euclidean norm, which is the square root of the dot product of the vector with itself, or the sum of the squared vector elements

$$\|\vec{v}\| = \sqrt{\vec{v}\cdot\vec{u}} = \left[\sum_{i=1}^{n} {v_i}^2\right]^{\frac{1}{2}}. \tag{A.2}$$

Normalization

A vector that has a norm equal to unity, is said to be a unit vector. Any non-zero vector can be represented as a unity vector by diving it by its norm

$$\hat{u} = \frac{\vec{v}}{\|\vec{v}\|} = \frac{\vec{v}}{v}\,. \tag{A.3}$$

Angle between vectors

The angle between two vectors is given by

$$\cos\theta = \frac{\vec{u}\cdot\vec{v}}{\|\vec{u}\|\,\|\vec{v}\|}\,. \tag{A.4}$$

Cross product

The cross product (or vector product) of a three-component vector in terms of its components is written as

$$\vec{\boldsymbol{u}} \times \vec{\boldsymbol{v}} = \begin{bmatrix} u_2 v_3 - u_3 v_2 \\ u_3 v_1 - u_1 v_3 \\ u_1 v_2 - u_2 v_1 \end{bmatrix} = -\vec{\boldsymbol{v}} \times \vec{\boldsymbol{u}}, \tag{A.5}$$

where the resulting vector is perpendicular to both $\vec{\boldsymbol{u}}$ and $\vec{\boldsymbol{v}}$.

Cross product matrix

The cross product operation can be rewritten in a matrix form as

$$\vec{\boldsymbol{u}} \times \vec{\boldsymbol{v}} = [\vec{\boldsymbol{u}}\times]\, \vec{\boldsymbol{v}}, \tag{A.6}$$

where $[\vec{\boldsymbol{u}}\times]$ is known as the cross product matrix and it is defined as

$$[\vec{\boldsymbol{u}}\times] \equiv \begin{bmatrix} 0 & -u_3 & u_2 \\ u_3 & 0 & -u_1 \\ -u_2 & u_1 & 0 \end{bmatrix}. \tag{A.7}$$

A.2. QUATERNIONS

Definition

A quaternion is a hyper-complex number, which can be represented as a four-component vector

$$\mathbf{q} = q_4 + i\, q_1 + j\, q_2 + k\, q_3 = q_4 + \vec{\boldsymbol{q}}, \tag{A.8}$$

where q_i are scalars, and i, j and k are operators that satisfy the following conditions:

$$\begin{aligned} i^2 &= j^2 = k^2 = -1, \\ i\,j &= -j\,i = k, \\ j\,k &= -k\,j = i, \\ k\,i &= -i\,k = j. \end{aligned}$$

The quaternion can be also represented in vector form as

$$\mathbf{q} = \begin{bmatrix} q_1 \\ q_2 \\ q_3 \\ q_4 \end{bmatrix} = \begin{bmatrix} \vec{\boldsymbol{q}} \\ q \end{bmatrix}. \tag{A.9}$$

Conjugate

As any complex number, the conjugated of a quaternion $\mathbf{q}$ is defined as

$$\mathbf{q}^* = q_4 - i\, q_1 - j\, q_2 - k\, q_3. \tag{A.10}$$

Unit quaternion

The unit quaternions are especially useful for attitude representation. The process to normalize a quaternion is thus the same as for any vector

$$\hat{\mathbf{q}} = \frac{\mathbf{q}}{\|\mathbf{q}\|} = \frac{\mathbf{q}}{\sqrt{{q_1}^2 + {q_2}^2 + {q_3}^2 + {q_4}^2}}. \tag{A.11}$$

Product

The product between two quaternions can be defined as

$$\begin{aligned}\mathbf{q}\otimes\mathbf{p} &= \left(q_4+\vec{\boldsymbol{q}}\right)\left(p_4+\vec{\boldsymbol{p}}\right),\\ &= q_4\,p_4-\vec{\boldsymbol{q}}\cdot\vec{\boldsymbol{p}}+q_4\,\vec{\boldsymbol{p}}+p_4\,\vec{\boldsymbol{q}}+\left(\vec{\boldsymbol{q}}\times\vec{\boldsymbol{p}}\right),\\ &= \begin{bmatrix} q_4\,\vec{\boldsymbol{p}}+p_4\,\vec{\boldsymbol{q}}+\left(\vec{\boldsymbol{q}}\times\vec{\boldsymbol{p}}\right)\\ q_4\,p_4-\vec{\boldsymbol{q}}\cdot\vec{\boldsymbol{p}}\end{bmatrix},\end{aligned} \tag{A.12}$$

this product can also be represented as a product matrix in the same way as for definition A.7

$$\mathbf{q}\otimes\mathbf{p}=\begin{bmatrix} q_4 & -q_3 & q_2 & q_1\\ q_3 & q_4 & -q_1 & q_2\\ -q_2 & q_1 & q_4 & q_3\\ -q_1 & -q_2 & -q_3 & q_4\end{bmatrix}\begin{bmatrix} p_1\\ p_2\\ p_3\\ p_4\end{bmatrix}, \tag{A.13}$$

or by means of the conjugate as

$$\begin{aligned}\mathbf{q}\otimes\mathbf{p} &= \mathbf{p}^{*}\otimes\mathbf{q}\\ &= \begin{bmatrix} p_4 & p_3 & -p_2 & p_1\\ -p_3 & p_4 & p_1 & p_2\\ p_2 & -p_1 & p_4 & p_3\\ -p_1 & -p_2 & -p_3 & p_4\end{bmatrix}\begin{bmatrix} q_1\\ q_2\\ q_3\\ q_4\end{bmatrix}.\end{aligned} \tag{A.14}$$

A.3. ROTATIONS AND TRANSFORMATIONS

Direction Cosine Matrix

Given an inertial frame $\mathcal{F}_i$ and a moving body frame $\mathcal{F}_b$, the transformation matrix

$${}^{b}\mathbf{R}_i=\begin{bmatrix} \boldsymbol{X}_b(1) & \boldsymbol{X}_b(2) & \boldsymbol{X}_b(3)\\ \boldsymbol{Y}_b(1) & \boldsymbol{Y}_b(2) & \boldsymbol{Y}_b(3)\\ \boldsymbol{Z}_b(1) & \boldsymbol{Z}_b(2) & \boldsymbol{Z}_b(3)\end{bmatrix} \tag{A.15}$$

has the particular property of mapping vectors from the inertial to the body frame.

DCM from a rotation angle

A rotation denoted by an angle in a given reference frame $\mathcal{F}$ is represented by means of a rotation matrix, whose elements depend on the value of the angle and the reference axis where the rotation is applied:

- A rotation ϕ around $\boldsymbol{X}$-axis:

$$\mathbf{R}_{\phi}=\begin{bmatrix} 1 & 0 & 0\\ 0 & \cos\phi & \sin\phi\\ 0 & -\sin\phi & \cos\phi\end{bmatrix}. \tag{A.16}$$

- Rotation θ around $\boldsymbol{Y}$-axis:

$$\mathbf{R}_{\theta}=\begin{bmatrix} \cos\theta & 0 & -\sin\theta\\ 0 & 1 & 0\\ \sin\theta & 0 & \cos\theta\end{bmatrix}. \tag{A.17}$$

- Rotation ψ around $\boldsymbol{Z}$-axis:

$$\mathbf{R}_{\psi} = \begin{bmatrix} \cos\psi & \sin\psi & 0 \\ -\sin\psi & \cos\psi & 0 \\ 0 & 0 & 1 \end{bmatrix}. \tag{A.18}$$

Note that the positive direction of the rotation follows the right-hand rule. In addition, the previous rotations can be unified in a single rotation matrix, this allows the attitude representation of any moving frame w.r.t. a fixed frame. The sequence of the rotation is arbitrary, however the most common used is the sequence 321 or XYZ, which is

$$\begin{aligned} \mathbf{R}_{321} &= \mathbf{R}_{\psi\theta\phi} = \mathbf{R}_{\psi}\,\mathbf{R}_{\theta}\,\mathbf{R}_{\phi} \\ &= \begin{bmatrix} c\theta\,c\psi & c\theta\,s\psi & -s\theta\,, \\ -c\phi\,s\psi + s\phi\,s\theta\,c\psi & c\phi\,c\psi + s\phi\,s\theta\,s\psi & s\phi\,c\theta \\ s\theta\,c\psi + c\phi\,s\theta\,c\psi & -s\phi\,c\psi + c\phi\,s\theta\,s\psi & c\phi\,c\theta \end{bmatrix}. \end{aligned} \tag{A.19}$$

The other possible sequences can be found in the literature (see e.g. Wertz [51], Hughes [24]).

Successive rotations

Given a rotation from frame $\mathcal{F}_a$ to frame $\mathcal{F}_c$ represented as the product of two successive intermediate rotations

$${}^{a}\mathbf{R}_{c} = {}^{a}\mathbf{R}_{b}\,{}^{b}\mathbf{R}_{c}\,, \tag{A.20}$$

the equivalent quaternion can be obtained as the product between the quaternion representing the intermediate rotation matrices as

$${}^{a}\mathbf{q}_{c} = {}^{b}\mathbf{q}_{c} \otimes {}^{a}\mathbf{q}_{b} \tag{A.21}$$

however, the order of the factors in the operation changes.

Quaternion to Direction Cosine Matrix

The representation of a DCM in terms of a quaternion is proposed by Sidi [42] as

$$\mathbf{R} = \begin{bmatrix} {q_1}^2 - {q_2}^2 - {q_3}^2 + {q_4}^2 & 2\left(q_1\,q_2 + q_3\,q_4\right) & 2\left(q_1\,q_3 - q_2\,q_4\right) \\ 2\left(q_1\,q_2 - q_3\,q_4\right) & -{q_1}^2 + {q_2}^2 - {q_3}^2 + {q_4}^2 & 2\left(q_2\,q_3 + q_1\,q_4\right) \\ 2\left(q_1\,q_3 + q_2\,q_4\right) & 2\left(q_2\,q_3 - q_1\,q_4\right) & -{q_1}^2 - {q_2}^2 + {q_3}^2 + {q_4}^2 \end{bmatrix}. \tag{A.22}$$

Direction Cosine Matrix to quaternion

Let $\mathbf{R}$ be a DCM, whose elements are denoted by $r_{i,j}$, the equivalent rotation quaternion is obtained by using the procedure defined by Klumpp [25]. For that, it is necessary to compute eight solutions of the form

$$\mathbf{q}_0 = \pm\frac{1}{2}\begin{bmatrix} (r_{23} - r_{32})\big/(1 + r_{11} + r_{22} + r_{33})^{\frac{1}{2}} \\ (r_{31} - r_{13})\big/(1 + r_{11} + r_{22} + r_{33})^{\frac{1}{2}} \\ (r_{12} - r_{21})\big/(1 + r_{11} + r_{22} + r_{33})^{\frac{1}{2}} \\ (1 + r_{11} + r_{22} + r_{33})^{\frac{1}{2}} \end{bmatrix}, \tag{A.23}$$

$$\mathbf{q}_1 = \pm\frac{1}{2}\begin{bmatrix} (1 + r_{11} - r_{22} - r_{33})^{\frac{1}{2}} \\ (r_{12} + r_{21})\big/(1 + r_{11} - r_{22} - r_{33})^{\frac{1}{2}} \\ (r_{13} + r_{31})\big/(1 + r_{11} - r_{22} - r_{33})^{\frac{1}{2}} \\ (r_{23} - r_{32})\big/(1 + r_{11} - r_{22} - r_{33})^{\frac{1}{2}} \end{bmatrix}, \tag{A.24}$$

$$\mathbf{q}_2 = \pm\frac{1}{2}\begin{bmatrix} (r_{12}+r_{21})/(1-r_{11}+r_{22}-r_{33})^{\frac{1}{2}} \\ (1-r_{11}+r_{22}-r_{33})^{\frac{1}{2}} \\ (r_{23}+r_{32})/(1-r_{11}+r_{22}-r_{33})^{\frac{1}{2}} \\ (r_{31}-r_{13})/(1-r_{11}+r_{22}-r_{33})^{\frac{1}{2}} \end{bmatrix}, \tag{A.25}$$

$$\mathbf{q}_3 = \pm\frac{1}{2}\begin{bmatrix} (r_{13}+r_{31})/(1-r_{11}-r_{22}+r_{33})^{\frac{1}{2}} \\ (r_{23}+r_{32})/(1-r_{11}-r_{22}+r_{33})^{\frac{1}{2}} \\ (1-r_{11}-r_{22}+r_{33})^{\frac{1}{2}} \\ (r_{12}-r_{21})/(1-r_{11}-r_{22}+r_{33})^{\frac{1}{2}} \end{bmatrix}. \tag{A.26}$$

Depending on the value of the elements of $\mathbf{R}$, some of previous quaternions will have a complex solution, therefore the following set of rules is defined

$$\mathbf{q}_\mathbf{R} = \begin{cases} \mathbf{q}_0 \text{ if } r_{22} > -r_{33}, \text{ AND } r_{11} > -r_{22}, \text{ AND } r_{11} > -r_{33}, \\ \mathbf{q}_1 \text{ if } r_{22} < -r_{33}, \text{ AND } r_{11} > \ r_{22}, \text{ AND } r_{11} > \ r_{33}, \\ \mathbf{q}_2 \text{ if } r_{22} > \ r_{33}, \text{ AND } r_{11} < \ r_{22}, \text{ AND } r_{11} < -r_{33}, \\ \mathbf{q}_3 \text{ if } r_{22} < \ r_{33}, \text{ AND } r_{11} < -r_{22}, \text{ AND } r_{11} < \ r_{33}, \end{cases} \tag{A.27}$$

with the aim of choosing the right quaternion. The sign of the solutions chosen in a way that q_4 is always positive.

Vector rotation by a quaternion

The rotation of a vector $\vec{\boldsymbol{v}}$ by means of a quaternion $\mathbf{q}$ is defined as

$$\vec{\boldsymbol{V}}' = \mathbf{q}^* \otimes \vec{\boldsymbol{V}} \otimes \mathbf{q} = \mathbf{q} \otimes \vec{\boldsymbol{V}}^T \otimes \mathbf{q}^* \tag{A.28}$$

where $\vec{\boldsymbol{V}} = \begin{bmatrix} \vec{\boldsymbol{v}} & 0 \end{bmatrix}^T$ and $\vec{\boldsymbol{V}}' = \begin{bmatrix} \vec{\boldsymbol{v}}' & 0 \end{bmatrix}^T$.

Time derivative of a quaternion

The calculation of the time derivative of a quaternion $\mathbf{q}$ in terms of the quaternion itself and the corresponding angular rate is defined by Kuipers [27] as

$$\dot{\mathbf{q}} = \frac{1}{2}\vec{\boldsymbol{\omega}}' \otimes \mathbf{q} = \frac{1}{2}\boldsymbol{\Omega}'(\vec{\boldsymbol{\omega}})\ \mathbf{q}, \tag{A.29}$$

or in terms of the conjugated quaternion

$$\dot{\mathbf{q}} = \frac{1}{2}\mathbf{q}^* \otimes \vec{\boldsymbol{\omega}}' = \frac{1}{2}\boldsymbol{\Xi}\big(\mathbf{q}\big)\ \vec{\boldsymbol{\omega}}', \tag{A.30}$$

where

$$\boldsymbol{\Omega}'(\vec{\boldsymbol{\omega}}) = \begin{bmatrix} 0 & \omega_z & -\omega_y & \omega_x \\ -\omega_z & 0 & \omega_x & \omega_y \\ \omega_y & -\omega_x & 0 & \omega_z \\ -\omega_x & -\omega_y & -\omega_z & 0 \end{bmatrix},\ \boldsymbol{\Xi}\big(\mathbf{q}\big) = \begin{bmatrix} q_4 & -q_3 & q_2 & q_1 \\ q_3 & q_4 & -q_1 & q_2 \\ -q_2 & q_1 & q_4 & q_3 \\ -q_1 & -q_2 & -q_3 & q_4 \end{bmatrix} \text{ and } \vec{\boldsymbol{\omega}}' = \begin{bmatrix} \vec{\boldsymbol{\omega}} \\ 0 \end{bmatrix} = \begin{bmatrix} \omega_x \\ \omega_y \\ \omega_z \\ 0 \end{bmatrix}.$$

From previous calculations, the equation for obtaining the angular rates in terms of a rotation quaternion and its derivative can be expressed as

$$\vec{\boldsymbol{\omega}}' = 2\,\dot{\mathbf{q}} \otimes \mathbf{q}^*. \tag{A.31}$$

In the same way, the second derivative of a quaternion w.r.t to time, is proposed by Kuipers

[27] as

$$\ddot{\mathbf{q}} = \frac{1}{2}\left(\dot{\vec{\omega}}' \otimes \mathbf{q} + \vec{\omega}' \otimes \dot{\mathbf{q}}\right), \tag{A.32}$$

and the corresponding angular acceleration

$$\dot{\vec{\omega}}' = 2\left(\ddot{\mathbf{q}} \otimes \mathbf{q}^* + \dot{\mathbf{q}} \otimes \dot{\mathbf{q}}^*\right). \tag{A.33}$$

Time derivative of a rotation matrix

The time derivative of a rotation matrix is defined by Diebel [10] as

$$\dot{\boldsymbol{R}} = \vec{\boldsymbol{\omega}} \times \boldsymbol{R}, \tag{A.34}$$

$$\dot{\boldsymbol{R}} = \boldsymbol{\Omega}\boldsymbol{R}, \tag{A.35}$$

where

$$\boldsymbol{\Omega}(\vec{\boldsymbol{\omega}}) = [\vec{\boldsymbol{\omega}}\times] = \begin{bmatrix} 0 & \omega_z & -\omega_y \\ -\omega_z & 0 & \omega_x \\ \omega_y & -\omega_x & 0 \end{bmatrix}.$$

B

ORBITAL MECHANICS AND REFERENCE FRAMES

This appendix contains a description about Keplerian orbits and the different parameters that characterise it, this also includes a brief description about some useful vectors and different time representations used for space applications. Later on, the reference coordinate frames used along this work are described, as well as some useful transformations used to change between coordinated frames .

B.1. KEPLERIAN ORBITS

The motion of a satellite orbiting a celestial body can be generalized, according the Kepler laws of planetary motion, as an ellipse, an example of Keplerian orbit is presented in Fig. B.1. As seen, this ellipse has two focal points (F_1 and F_2) and the Earth is located in one of them. The apogee and perigee are consequently defined as the points in the orbit where the distances between the Earth's CoM and the satellite is, respectively, the longest and the shortest. The distance between any focal point and the center of the ellipse is denoted by c.

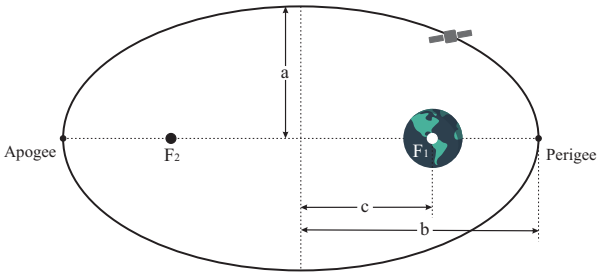

Figure B.1: Elliptical orbit.

The semi-major axis a is therefore defined as the distance between the center of the ellipse and the perigee, or

$$a = \frac{\text{apogee+perigee}}{2}, \tag{B.1}$$

in the same way, the semi-minor axis is denoted by

$$b = \frac{\text{apogee-perigee}}{2}, \tag{B.2}$$

and the eccentricity e is defined as the distance ratio between c and the semi-major axis, or

$$e = \frac{c}{a} = \frac{\sqrt{a^2 - b^2}}{a} = \sqrt{1 - \frac{b^2}{a^2}}. \tag{B.3}$$

In a Keplerian orbit, there are two points where the satellite crosses the equatorial plane (see Fig. B.2): the first one is called the descending node (N_1), in this point the satellite passes from the northern hemisphere to the southern hemisphere, the second point is called ascending node (N_2), here the satellite crosses from the southern hemisphere to the northern hemisphere [29].

The inclination i is defined as the angle between the orbital and equatorial planes, the argument of perigee ω defines the angle between the ascending node and the perigee, Ω represents the angle between the $\boldsymbol{X}_i$ and the ascending node N_2, and the true anomaly ν defines the position of the satellite along the orbit (measured from the perigee). All these parameters are illustrated in Fig. B.2.

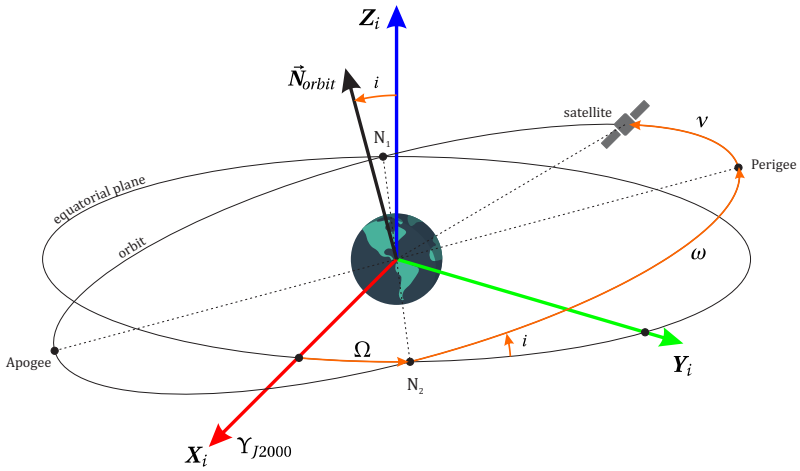

Figure B.2: Kepler parameters and ECI frame.

B.2. CONVERSION FROM $[a\ e\ i\ \Omega\ \omega\ \nu]^T$ TO $[\vec{r}\ \vec{v}]^T$

The ADCS of the S2TEP mission uses Cartesian coordinates for the representation of the position and orbital velocity vectors; therefore, a transformation from the Kepler elements to ECI coordinates must be defined in order to calculate the initial position of the satellite in the orbit. This procedure is defined by Hintz [23], and it will be explained in the following paragraphs.

The orbit semi-latus rectum p_{orbit} is calculated as

$$p_{orbit} = a\left(1 - e^2\right), \tag{B.4}$$

and the time varying magnitude of the orbital radius is defined as

$$r_{orbit} = \frac{p_{orbit}}{1 + e\cos\nu}. \tag{B.5}$$

From these two parameters the satellite position vector is defined as

$$ {}^{i}\vec{\boldsymbol{r}} = {}^{i}\mathbf{R}_{kepler} \begin{bmatrix} r_{orbit}\cos\nu \\ r_{orbit}\sin\nu \\ 0 \end{bmatrix}, \tag{B.6} $$

and the orbital velocity vector as

$$ {}^{i}\vec{\boldsymbol{v}} = {}^{i}\mathbf{R}_{kepler} \begin{bmatrix} -\sqrt{\frac{\mu}{p}}\sin\nu \\ \sqrt{\frac{\mu}{p}}\,(e-\cos\nu) \\ 0 \end{bmatrix}, \tag{B.7} $$

where

$$ {}^{i}\mathbf{R}_{kepler} = \begin{bmatrix} \mathrm{c}\omega\,\mathrm{c}\Omega - \mathrm{s}\omega\,\mathrm{c}i\,\mathrm{s}\Omega & -\mathrm{s}\omega\,\mathrm{c}\Omega - \mathrm{c}\omega\,\mathrm{c}i\,\mathrm{s}\Omega & \mathrm{s}\Omega\,\mathrm{s}i \\ \mathrm{c}\omega\,\mathrm{s}\Omega + \mathrm{s}\omega\,\mathrm{c}i\,\mathrm{c}\Omega & -\mathrm{s}\omega\,\mathrm{s}\Omega + \mathrm{c}\omega\,\mathrm{c}i\,\mathrm{c}\Omega & -\mathrm{s}i\,\mathrm{c}\Omega \\ \mathrm{s}\omega\,\mathrm{s}i & \mathrm{c}\omega\,\mathrm{c}i & \mathrm{c}i \end{bmatrix} \tag{B.8} $$

and s denotes the sine function while c denotes the cosine function.

The inverse transformation can be found at [23].

B.3. CALENDAR DATE TO JULIAN DATE

According to Capderou [7], the Julian Date (JD) was introduced in astronomy to overcome the difficulty of identifying a particular date in history without ambiguity. In Julian date, the days are the basic measurement units and fractions of it represent the current time.

Given that the reference point of the Julian Date is quite far in the past (January 1, 4713 BC), the Modified Julian Date (MJD) was also introduced to solve this issue, this new reference is defined at noon January 1, 2000; and it is calculated from the Julian Date as

$$ MJD = JD - 2\,400\,000.5\,. \tag{B.9} $$

Montenbruck and Gill [32] define the procedure to obtain the MJD from a given date expressed in calendar date (represented in year Y_{CD}, month M_{CD} and day D_{CD}).

Let

$$ y_{MJD} = \begin{cases} Y_{CD} - 1 & \text{if } M_{CD} \leq 2\,, \\ Y_{CD} & \text{otherwise}\,, \end{cases} \tag{B.10} $$

and

$$ m_{MJD} = \begin{cases} M_{CD} + 12 & \text{if } M_{CD} \leq 2\,, \\ M_{CD} & \text{otherwise}\,. \end{cases} \tag{B.11} $$

The leap days in the Julian and Gregorian calendars are also taken into account by the auxiliary quantity

$$ b_{MJD} = \begin{cases} -2 + \left\lfloor \frac{y_{MJD}+4716}{4} \right\rfloor - 1179 & \text{until 4 Oct. 1582}\,, \\ + \left\lfloor \frac{y_{MJD}}{400} \right\rfloor - \left\lfloor \frac{y_{MJD}}{100} \right\rfloor + \left\lfloor \frac{y_{MJD}}{4} \right\rfloor & \text{from 10 Oct. 1582} \end{cases} \tag{B.12} $$

The Modified Julian Date is hence derived from

$$ MJD = 365\,y_{MJD} - 679\,004 + b_{MJD} + \lfloor 30.6001\,(m_{MJD}+1) \rfloor + D_{CD}, \tag{B.13} $$

where the fractional part of a day D_{CD} is represented in seconds and $\lfloor \square \rfloor$ denotes the floor oper-

ator *.

The inverse transformation can be found at [32].

B.4. SUN VECTOR

In order to simulate the change of the Sun direction along the orbit, the Sun vector $\vec{S}$ was obtained from the satellite position vector $\vec{r}_{sat}$ and the Sun position w.r.t. to the Earth $\vec{r}_{sun/earth}$ (see Fig. B.3). The position of the satellite is know at any time from the mesurements, and $\vec{r}_{sun/earth}$ was obtained by means the JPL ephemerides.

The JPL ephemerides allow to approximate the position of any major planet by means of its Kepler parameters and the current JD, the complete procedure for the calculation of $\vec{r}_{sun/earth}$ can be found at [47].

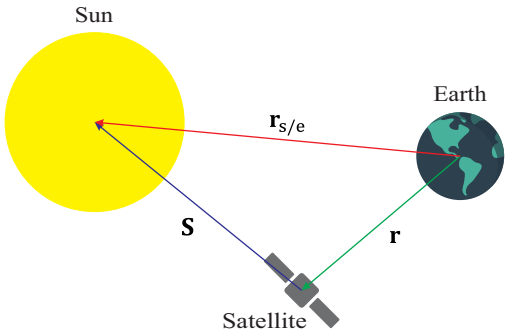

Figure B.3: Relevant position vectors.

B.5. REFERENCE FRAMES

The definitions for each of the frames presented in Table 1, is described in this section. Depending on the type of coordinates used for the representation of elements in a given frame, it can be classified as Cartesian or spherical.

B.5.1. Cartesian coordinated frames

For S2TEP the following reference frames were defined:

Earth-Centered Inertial frame

The Earth Centered Inertial (ECI) frame is denoted by $\mathcal{F}_i = \{\mathcal{O}_i, \boldsymbol{X}_i, \boldsymbol{Y}_i, \boldsymbol{Z}_i\}$. This frame is free of rotation and its origin is placed at the Earth's CoM, its $\boldsymbol{X}_i$-axis points towards the vernal equinox of year 2000 (J2000 in the Julian date calendar) and lies within the Earth's equatorial plane. $\boldsymbol{Z}_i$-axis points in the direction of the Earth's angular momentum vector, and $\boldsymbol{Y}_i$-axis completes a right-handed orthonormal system (see Fig. B.2). This frame is based on the quasi-inertial Inertial Celestial Reference Frame (ICRF), which was originally proposed by the International Astronomical Union (IAU) and it is currently mantained by the International Earth Rotation Service (IERS) [13, 31].

Earth-Centered Earth-Fixed frame

The Earth Centered - Earth Fixed frame is defined by $\mathcal{F}_e = \{\mathcal{O}_e, \boldsymbol{X}_e, \boldsymbol{Y}_e, \boldsymbol{Z}_e\}$. The origin of this frame is placed at the Earth's CoM, $\boldsymbol{X}_e$-axis lies within the equatorial plane and points towards the

*The floor operator receives a rational number x as argument, and it retrieves the greatest integer less than or equal to x.

IERS Reference Meridian (IRM), also known as the Greenwich meridian. $\boldsymbol{Z}_e$-axis points towards the Earth's angular momentum vector, and the remaining axis ($\boldsymbol{Y}_e$) completes a right-handed orthonormal system [31]. The ECEF frame is based on the International Terrestrial Reference Frame (ITRF) and it was was introduced by the Federal Agency for Cartography and Geodesy [14].

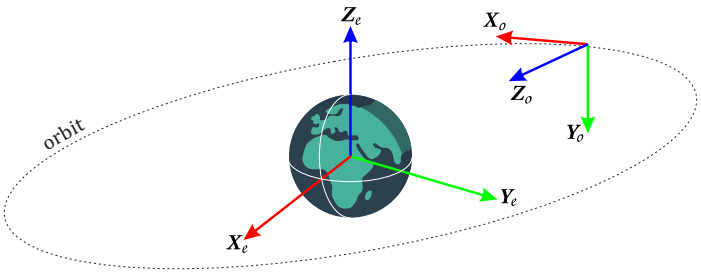

Figure B.4: ECEF and orbital frames.

Orbital frame

The orbital frame is denoted by $\mathcal{F}_o = \{\mathcal{O}_o, \boldsymbol{X}_o, \boldsymbol{Y}_o, \boldsymbol{Z}_o\}$. The origin of this frame can be placed at any point on the orbit, thus the orientation of its axes is evolving according to the selected position. Its $\boldsymbol{X}_o$-axis is parallel to the velocity vector, $\boldsymbol{Z}_o$-axis points in the direction of the cross product between $\boldsymbol{X}_o$ and the position vector $\vec{\boldsymbol{r}}$. The orthonormal system is then completed with the Nadir vector.

Body-Fixed frame

The satellite body frame is defined as $\mathcal{F}_b = \{\mathcal{O}_b, \boldsymbol{X}_b, \boldsymbol{Y}_b, \boldsymbol{Z}_b\}$. The origin of this frame is always specified at the CoM of the satellite. $\boldsymbol{Z}_b$-axis is placed on the satellite's axial symmetry axis (in direction of the top face), $\boldsymbol{X}_b$-axis is located in one of the lateral faces and $\boldsymbol{Y}_b$-axis completes a right-handed orthonormal system (see Fig. B.4) [48].

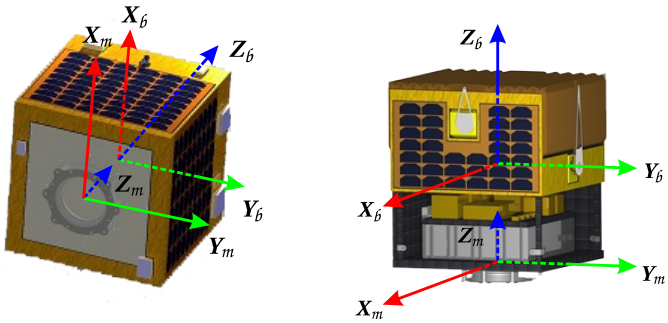

Figure B.5: Body and mechanical frames.

Mechanical Coordinated Frame

The Mechanical Coordinate frame is represented by $\mathcal{F}_m = \{\mathcal{O}_m, \boldsymbol{X}_m, \boldsymbol{Y}_m, \boldsymbol{Z}_m\}$. The origin of this frame is placed at any point in the structure of the satellite (sometimes it shares the same point with the origin of the structure in the CAD software). All the axes are parallel to those of the body

frame. This frame is particularly useful since most of the sensor measurements are described using it as reference. Fig. B.4 shows the position of the MCF for S2TEP.

Principal axes of inertia

The method for transforming a non-diagonal symmetric moment of inertia matrix into a diagonal one is a common procedure treated in linear algebra [42]. In the case of a spin stabilized satellite, the angular rates described in the body frame $\begin{bmatrix}\omega_x & \omega_y & \omega_z\end{bmatrix}$ in the kinetic energy equation

$$\mathbf{T}_{rot} = \frac{1}{2}\vec{\boldsymbol{\omega}}_{sat}^{T}\mathbf{J}_{sat}\vec{\boldsymbol{\omega}}_{sat}, \tag{B.14}$$

can be used to obtain the rotation matrix from body frame coordinates to principal coordinates. The components of ${}^{b}\vec{\boldsymbol{\omega}}_{sat}$ will be thus changed to ${}^{p}\vec{\boldsymbol{\omega}}_{sat}$ by means of the following transformation

$${}^{b}\vec{\boldsymbol{\omega}}_{sat} = {}^{b}\mathbf{R}_{p}\,{}^{p}\vec{\boldsymbol{\omega}}_{sat}. \tag{B.15}$$

The computation of ${}^{b}\mathbf{R}_{p}$ can be hence derived from equation B.14 as

$$2\,\mathbf{T}_{rot} = \left({}^{b}\mathbf{R}_{p}\,{}^{p}\vec{\boldsymbol{\omega}}_{sat}\right)^{T}{}^{b}\mathbf{J}_{sat}\left({}^{b}\mathbf{R}_{p}\,{}^{p}\vec{\boldsymbol{\omega}}_{sat}\right), \tag{B.16}$$

$$= {}^{p}\vec{\boldsymbol{\omega}}_{sat}{}^{T}\,{}^{b}\mathbf{R}_{b}{}^{T}\,{}^{b}\mathbf{J}_{sat}\,{}^{b}\mathbf{R}_{b}\,{}^{p}\vec{\boldsymbol{\omega}}_{sat}, \tag{B.17}$$

$$= {}^{p}\vec{\boldsymbol{\omega}}_{sat}{}^{T}\,{}^{p}\mathbf{J}_{sat}\,{}^{p}\vec{\boldsymbol{\omega}}_{sat}, \tag{B.18}$$

where the eigenvalues of matrix ${}^{b}\mathbf{J}_{sat}$ are the principal moments of inertia of the diagonal matrix ${}^{p}\mathbf{J}_{sat}$. The elements of the rotation matrix can be found by evaluating $det\left({}^{b}\mathbf{J}_{sat} - \lambda(\mathbf{I})\right)$, where $\mathbf{I}_{3\times3}$ is an identity matrix. The eigenvectors $\hat{\boldsymbol{e}}_1$, $\hat{\boldsymbol{e}}_2$, $\hat{\boldsymbol{e}}_3$ of ${}^{b}\mathbf{J}_{sat}$ will be the column vectors of the transformation matrix ${}^{b}\mathbf{R}_{p}$, or

$${}^{b}\mathbf{R}_{p} = \begin{bmatrix} e_{1_x} & e_{2_x} & e_{3_x} \\ e_{1_y} & e_{2_y} & e_{3_y} \\ e_{1_z} & e_{2_z} & e_{3_z} \end{bmatrix}, \tag{B.19}$$

where those eigenvectors can be found from the set of equations $\lambda_i\,\hat{\boldsymbol{e}}_i = {}^{b}\mathbf{J}_{sat}\,\hat{\boldsymbol{e}}_i;\ i = 1, 2, 3$.

Transformations between ECEF and ECI frames

As outlined in the definition of the ECI and ECEF coordinate frames, $\boldsymbol{Z}_e$- and $\boldsymbol{Z}_i$-axes are both parallel to the Earth's angular momentum vector, therefore the transformation from ECI coordinates to ECEF is defined by [32] as simple rotation around $\boldsymbol{Z}$-axis, or

$${}^{e}\mathbf{R}_{i} = \begin{bmatrix} \cos\psi_{earth} & \sin\psi_{earth} & 0 \\ -\sin\psi_{earth} & \cos\psi_{earth} & 0 \\ 0 & 0 & 1 \end{bmatrix}, \tag{B.20}$$

where ψ_{earth} denotes the rotation of the ECEF frame w.r.t. the ECI frame, and it can be directly obtained from the Modified Julian Date as

$$\psi_{earth} = 2\,\pi\{MJD\} \tag{B.21}$$

where the operator $\{\square\}$ represents the fractional part of the current Modified Julian Date. For this analysis it is considered that one revolution around the Earth's rotation axis takes roughly 1 day.

For the calculation of the inverse transformation, matrix B.20 is inverted and then multiplied by the position in the ECEF frame.

B.5.2. Spherical coordinated frames

In order to describe the position of any object orbiting the Earth (or even placed on its surface) not only Cartesian coordinate systems can be used, but also spherical coordinates. Among them, the most typical definitions for aerospace applications are the geocentric and geodetic coordinates, they both use the ECEF frame as reference frame. The main difference lies on how Earth's shape is modelled, the geocentric model uses an sphere while the geodetic uses an ellipsoid.

Let the longitude λ be the angle between $\boldsymbol{X}_e$-axis and the projection of vector ${}^e\vec{\mathbf{r}}$ onto the equatorial plane (XY_e), the geocentric latitude ϕ_{gc} is defined as the angle between vector ${}^e\vec{\mathbf{r}}$ and the equatorial plane, the geodetic latitude φ is the angle between the normal to the ellipsoid and the equatorial plane, and r the distance between the Earth's CoM and the satellite. These parameters are represented in a more illustrative way in Fig. B.4.

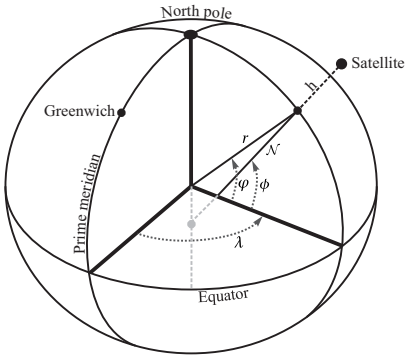

Figure B.6: Geocentric and geodetic coordinates.

The transformations used to change from spherical coordinates to Cartesian coordinates are presented in the next section, as well as the definitions to switch between geodetic and geocentric coordinates.

Geocentric coordinates

Let P be a point fixed on the ECEF frame, which is represented in Cartesian coordinates as ${}^e(x,\ y,\ z)$, the transformation of this point into geocentric coordinates ${}^{gc}(\phi_{gc},\ \lambda,\ r)$ can be derived from

$$\begin{aligned} \lambda &= \arctan\left(\frac{y}{x}\right), \\ \phi_{gc} &= \arcsin\left(\frac{z}{r}\right) = \arctan\frac{z}{\sqrt{x^2+y^2}}, \\ r &= \sqrt{x^2+y^2+z^2}. \end{aligned} \tag{B.22}$$

The inverse transformation is therefore defined as

$$\begin{aligned} x &= r\ \cos\phi_{gc}\ \cos\lambda, \\ y &= r\ \cos\phi_{gc}\ \sin\lambda, \\ z &= r\ \sin\phi_{gc}. \end{aligned} \tag{B.23}$$

Geodetic coordinates

According to Farell and Barth [12], the shape of the Earth can be approximated as an ellipse of revolution around its minor axis. The parameters that describe this ellipsoid are a semi-major axis

$$a_{earth} = 6\,378\,137\ \text{m},$$

a semi-minor axis

$$b_{earth} = 6\,356\,752.314\ \text{m},$$

and a flatness

$$f_{earth} = \frac{a_{earth} - b_{earth}}{a_{earth}} = 0.0034. \tag{B.24}$$

The eccentricity is thus defined as

$$e_{earth} = \sqrt{f_{earth}\left(2 - f_{earth}\right)} = 0.0818, \tag{B.25}$$

and the radius of curvature in the prime vertical as

$$\mathcal{N}_{earth} = \frac{a_{earth}}{\sqrt{1 - e_{earth}^2 \sin(\lambda)^2}}, \tag{B.26}$$

The transformation from ${}^{gd}(\varphi,\ \lambda,\ h)$ into ${}^{e}(x,\ y,\ z)$ will be

$$\begin{aligned} x &= (\mathcal{N} + h)\ \cos\varphi\ \cos\lambda, \\ y &= (\mathcal{N} + h)\ \cos\varphi\ \sin\lambda, \\ z &= \left[\mathcal{N}\ (1 - e^2) + h\right] \sin\varphi. \end{aligned} \tag{B.27}$$

The inverse process is not trivial, however Farell and Barth [12] proposed a method that guarantees convergence to the right geodetic representation, the procedure is defined as follows:

1. **Initialization**: Let

$$\begin{aligned} \lambda &= \arctan\left(\frac{y}{x}\right), \\ h_0 &= 0, \\ \mathcal{N}_0 &= a, \end{aligned}$$

2. **Perform the following iteration until convergence**:

$$\begin{aligned} \sin\varphi_i &= \frac{z}{\mathcal{N}_i\,(1 - e^2) + h_i}, \\ \mathcal{N}_i &= \frac{a}{\sqrt{1 - e^2\ \sin^2\varphi_i}}, \\ \varphi_i &= \arctan\left[\frac{z}{\sqrt{x^2 - y^2}}\left(1 - \frac{e^2}{1 + \frac{h_i}{\mathcal{N}_i}}\right)^{-1}\right], \\ h_i &= \frac{\sqrt{x^2 + y^2}}{\cos\varphi_i} - \mathcal{N}_i. \end{aligned}$$

Relationship between geodetic and geocentric coordinates

The relationship between the geodetic latitude φ and the geocentric latitude ϕ_{gc} is defined by Markley and Crassidis [30] as

$$\frac{\tan\phi_{gc}}{\tan\varphi} = 1 - \frac{\mathcal{N}}{\mathcal{N}+h}\, e^2 . \tag{B.28}$$

C

CONTROL THEORY

C.1. LYAPUNOV LINEARIZATION METHOD

The linearization of the state equation of a non-linear system

$$\dot{\vec{x}}(t) = \vec{\mathbf{f}}\left(\vec{x},\, \vec{u},\, t\right), \tag{C.1}$$

around an equilibrium point* $(\vec{x}_0,\, \vec{u}_0)$, is defined by Hendricks et al. [22] as the result of the computation of the Jacobian matrix of the non-linear state equations with respect to the state and output vectors, as

$$\mathbf{A} = \left.\frac{\partial \vec{\mathbf{f}}\left(\vec{x},\, \vec{u},\, t\right)}{\partial \mathbf{x}}\right|_{(\vec{x}_0,\, \vec{u}_0)}, \qquad \mathbf{B} = \left.\frac{\partial \vec{\mathbf{f}}\left(\vec{x},\, \vec{u},\, t\right)}{\partial \mathbf{u}}\right|_{(\vec{x}_0,\, \vec{u}_0)}, \tag{C.2}$$

this results in a linear representation of the form

$$\dot{\vec{x}}(t) = \mathbf{A}\,\vec{x}(t) + \mathbf{B}\,\vec{u}(t). \tag{C.3}$$

In order to apply the previous definition to equations 5.17 and 5.18, a state vector

$$\vec{x} = \begin{bmatrix} q_1 & q_2 & q_3 & q_4 & \omega_x & \omega_y & \omega_z \end{bmatrix}^T,$$

and an input vector

$$\vec{u} = \begin{bmatrix} \tau_{ctrl_x} & \tau_{ctrl_y} & \tau_{ctrl_z} \end{bmatrix},$$

are defined, the calculation of the input matrix is then carried out as

$$\mathbf{A} = \left[\begin{array}{cc} \dfrac{\partial \dot{\mathbf{q}}}{\partial \mathbf{q}} & \dfrac{\partial \dot{\mathbf{q}}}{\partial \vec{\omega}} \\ \dfrac{\partial \dot{\vec{\omega}}}{\partial \mathbf{q}} & \dfrac{\partial \dot{\vec{\omega}}}{\partial \vec{\omega}} \end{array}\right]_{(\mathbf{q}_0,\, \vec{\omega}_0)}, \tag{C.4}$$

$$= \left[\begin{array}{cc} \frac{1}{2}\boldsymbol{\Omega}'(\vec{\omega}) & \frac{1}{2}\boldsymbol{\Xi}\left(\mathbf{q}\right)_{1:4,1:3} \\ \mathbf{0}_{3\times 3} & \mathbf{A}_{\vec{\omega}} \end{array}\right]_{(\mathbf{q}_0,\, \vec{\omega}_0)}; \tag{C.5}$$

*An equilibrium point of a non-linear system is a state where the change in the dynamics of the system is null, and it is calculated by equating $\dot{\vec{x}}$ to zero. A non-linear dynamical system can have many equilibrium points, and they can be classified according to different mathematical properties. A more detailed analysis is carried out at Slotine and Li [44, pp. 53].

with

$$\begin{aligned}\mathbf{A}_{\vec{\omega}} &= \frac{\partial \dot{\vec{\omega}}}{\partial \vec{\omega}}, \\ &= \frac{\partial}{\partial \vec{\omega}}\left(\boldsymbol{J_{sat}}^{-1}\left(-\vec{\omega}\times \boldsymbol{J_{sat}}\,\vec{\omega}+\vec{\tau}\right)\right), \\ &= \boldsymbol{J_{sat}}^{-1}\left(\vec{\mathbf{1}}\times \boldsymbol{J_{sat}}\,\vec{\omega}-\vec{\omega}\times \boldsymbol{J_{sat}}\right), \\ &= \boldsymbol{J_{sat}}^{-1}\left(\boldsymbol{J_{sat}}\,\vec{\omega}\times\vec{\mathbf{1}}-\vec{\omega}\times \boldsymbol{J_{sat}}\right), \\ &= \boldsymbol{J_{sat}}^{-1}\left(\mathbf{S}(\boldsymbol{J_{sat}}\,\vec{\omega})-\boldsymbol{\Omega}(\vec{\omega})\,\boldsymbol{J_{sat}}\right), \end{aligned} \tag{C.6}$$

$$\mathbf{A}_{\vec{\omega}} = \begin{bmatrix} \left(\frac{J_y-J_z}{J_x}\right)\omega_z & \left(\frac{J_y-J_z}{J_x}\right)\omega_y & \\ \left(\frac{J_z-J_x}{J_y}\right)\omega_z & 0 & \left(\frac{J_z-J_x}{J_y}\right)\omega_x \\ \left(\frac{J_x-J_y}{J_z}\right)\omega_y & \left(\frac{J_x-J_y}{J_z}\right)\omega_x & 0 \end{bmatrix}, \tag{C.7}$$

and for the outputs matrix as

$$\mathbf{B} = \left[\begin{array}{c} \frac{\partial \dot{\mathbf{q}}}{\partial \vec{\tau}_{ctrl}} \\ \frac{\partial \dot{\vec{\omega}}}{\partial \vec{\tau}_{ctrl}} \end{array}\right]_{(\mathbf{q}_0,\,\vec{\omega}_0)}, \tag{C.8}$$

$$= \begin{bmatrix} \mathbf{0}_{4\times 3} \\ \boldsymbol{J_{sat}}^{-1} \end{bmatrix}. \tag{C.9}$$

If matrices C.5 and C.9 are evaluated at the equilibrium point $\boldsymbol{q}_0 = \begin{bmatrix}0 & 0 & 0 & 1\end{bmatrix}^T$ and $\vec{\omega}_0 = \begin{bmatrix}0 & 0 & 0\end{bmatrix}^T$, it is possible to observe that the dynamics of q_4 will no longer be affected by the other state variables; therefore, this variable can be eliminated for simplicity of the linear model. The new state vector will thus be

$$\vec{\boldsymbol{x}} = \begin{bmatrix} q_1 & q_2 & q_3 & \omega_x & \omega_y & \omega_z \end{bmatrix}^T, \tag{C.10}$$

and the corresponding state representation

$$\dot{\vec{\boldsymbol{x}}} = \begin{bmatrix} \mathbf{0}_{3\times 3} & \frac{1}{2}\mathbf{I}_{3\times 3} \\ \mathbf{0}_{3\times 3} & \mathbf{0}_{3\times 3} \end{bmatrix}\vec{\boldsymbol{x}} + \begin{bmatrix} \mathbf{0}_{3\times 3} \\ \boldsymbol{J_{sat}}^{-1} \end{bmatrix}\vec{\boldsymbol{u}}. \tag{C.11}$$

C.2. LYAPUNOV STABILITY THEORY

According to Ogata [37], given a non-linear system of the form

$$\dot{\vec{\boldsymbol{x}}}(t) = \vec{\mathbf{f}}(\vec{\boldsymbol{x}}, t), \tag{C.12}$$

and an equilibrium $\vec{\boldsymbol{x}}_e$, where $\vec{\mathbf{f}}(\vec{\boldsymbol{x}}_e, t) = 0$.

This equilibrium state is said to be stable in the sense of Lyapunov for each $\varepsilon > 0$, $\exists\, \delta(\varepsilon) > 0$

$$\|\vec{\boldsymbol{x}}_e - \vec{\boldsymbol{x}}_0\| < \delta(\varepsilon) \Rightarrow \|\vec{\boldsymbol{x}}(t) - \vec{\boldsymbol{x}}_0\| < \varepsilon, \text{ for all } t \geq 0, \tag{C.13}$$

In addition, it is said to be asymptotically stable, if it is stable in the sense of Lyapunov and if every solution with an initial $S(\delta)$ converges to $\vec{\boldsymbol{x}}_e$ as t increases,

$$\text{for } \exists \delta(\varepsilon) : \|\vec{\boldsymbol{x}}_e - \vec{\boldsymbol{x}}_0\| < \delta(\varepsilon) \Rightarrow lim_{t\,\to\inf} x(t) = \vec{\boldsymbol{x}}_e, \tag{C.14}$$

Let now $V(\vec{\boldsymbol{x}}, t) <$ be a time-varying function, which is positive definite in a region Ω, if there

exist a positive definite function such that

$$V(\vec{x}, t) > V(\vec{x}), \text{ for all } t > t_0, \tag{C.15}$$

$$V(\vec{0}, t) = 0, \text{ for all } t > t_0, \tag{C.16}$$

Theorem 1: Considering the system $\dot{\vec{x}}(t) = \vec{\mathbf{f}}(\vec{x}, t)$, which $\vec{\mathbf{f}}(\vec{0}, t)$, for all t. If there exist a scalar function $V(\vec{x}, t)$ having continuous, first partial derivative and guarantees that

- $V(\vec{x}, t)$ is positive definite, and
- $\dot{V}(\vec{x}, t)$ is negative definite

thus the equilibrium is said to be uniformly asymptotically stable.

C.3. LINEAR QUADRATIC REGULATOR

A time-invariant linear system

$$\dot{\vec{x}}(t) = \mathbf{A}\vec{x}(t) + \mathbf{B}\vec{u}(t), \tag{C.17}$$

is stabilisable trough the Linear Quadratic Regulator(LQR) with a feedback law

$$\vec{u}(t) = -\mathbf{K}\vec{x}(t), \tag{C.18}$$

while it is subject to the performance index

$$\mathcal{J}(\vec{u}(t)) = \frac{1}{2}\int_0^\infty \left(\vec{x}(t)^T \mathbf{Q}\vec{x}(t) + \vec{u}(t)^T \mathbf{R}\vec{u}(t)\right) dt. \tag{C.19}$$

iff the pair (**A**, **B**) is controllable [28].

The objective of this control formulation is to minimize both the control energy $\vec{u}$, and the tracking error $\vec{x}$ (for $\vec{\mathbf{r}} = 0$). This is achieved by the modification of the weighting matrices **Q** and **R**, which are diagonal positive-definite matrices, and they obey

$$\mathbf{Q} = \mathbf{Q}^T \geq \mathbf{0},$$
$$\mathbf{R} = \mathbf{R}^T > \mathbf{0}.$$

The value of the feedback matrix is then defined by Anderson and Moore [3] as

$$\mathbf{K} = \mathbf{R}^{-1}\mathbf{B}^T\mathbf{P}, \tag{C.20}$$

where **P** is the positive (symmetric) solution to the Ricatti algebraic equation

$$\mathbf{A}^T\mathbf{P} + \mathbf{P}\mathbf{A} - \mathbf{P}\mathbf{B}\mathbf{R}^{-1}\mathbf{B}^T\mathbf{P} + \mathbf{Q} = 0. \tag{C.21}$$

The final structure of the control loop is presented in Fig. C.1.

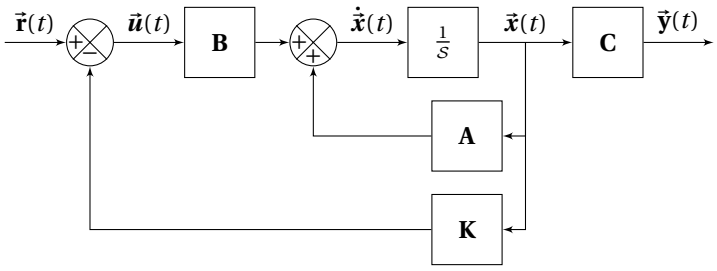

Figure C.1: LQR synthesis: control loop.

C.3.1. Stability proof [1]

Let consider the new closed-loop system with $\vec{\boldsymbol{u}}(t) = -\mathbf{K}\,\vec{\boldsymbol{x}}(t)$, as

$$\dot{\vec{\boldsymbol{x}}}(t) = (\mathbf{A} - \mathbf{B}\mathbf{K})\,\vec{\boldsymbol{x}}(t)\,, \tag{C.22}$$

the response of $\vec{\boldsymbol{x}}(t)$ to the initial conditions $\vec{\boldsymbol{x}}_0$ is

$$\vec{\boldsymbol{x}}(t) = e^{(\mathbf{A}-\mathbf{B}\mathbf{K})t}\,\vec{\boldsymbol{x}}_0\,, \tag{C.23}$$

and the performance index $\mathcal{J}$ becomes

$$\mathcal{J} = \frac{1}{2}\int_0^\infty \vec{\boldsymbol{x}}(t)^T\left(\mathbf{Q} + \mathbf{K}^\mathbf{T}\mathbf{R}\mathbf{K}\right)\vec{\boldsymbol{x}}(t)dt\,, \tag{C.24}$$

$$= \frac{1}{2}\vec{\boldsymbol{x}}_0^T\underbrace{\left(\int_0^\infty e^{(\mathbf{A}-\mathbf{B}\mathbf{K})t}\left(\mathbf{Q} + \mathbf{K}^T\mathbf{R}\mathbf{K}\right)e^{(\mathbf{A}-\mathbf{B}\mathbf{K})t}dt\right)}_{\mathbf{P}}\vec{\boldsymbol{x}}_0\,, \tag{C.25}$$

$$= \frac{1}{2}\vec{\boldsymbol{x}}_0^T\mathbf{P}\,\vec{\boldsymbol{x}}_0\,. \tag{C.26}$$

then, let $\mathbf{K}_c$ be the optimal value of $\mathbf{K}$ which minimizes $\mathcal{J}$, and $\mathbf{P}_c$ the particular solution to the Lyapunov equation (C.16), this results in

$$(\mathbf{A} - \mathbf{B}\mathbf{K}_c)^T\mathbf{P}_c + \mathbf{P}_c\,(\mathbf{A} - \mathbf{B}\mathbf{K}_c) + \mathbf{Q} + {\mathbf{K}_c}^T\mathbf{R}\mathbf{K}_c = 0\,. \tag{C.27}$$

A variation in $\mathbf{K}_c$ ($\mathbf{K}_c = \mathbf{K}_c + \mathbf{\Delta_K}$) leads to a variation in $\mathbf{P}_c$ ($\mathbf{P}_c = \mathbf{P}_c + \mathbf{\Delta_P}$), then equation C.27 is rewritten as

$$\left(\mathbf{A} - \mathbf{B}\,(\mathbf{K}_c + \mathbf{\Delta_K})\right)^T\left(\mathbf{P} + \mathbf{\Delta_P}\right) + \left(\mathbf{P} + \mathbf{\Delta_P}\right)\left(\mathbf{A} - \mathbf{B}\,(\mathbf{K}_c + \mathbf{\Delta_K})\right) + \mathbf{Q} + (\mathbf{K}_c + \mathbf{\Delta_K})^T\mathbf{R}\,(\mathbf{K}_c + \mathbf{\Delta_K}) = 0\,, \tag{C.28}$$

consequently, iff

$$\mathbf{\Delta_P} > 0 \;\; \forall \mathbf{\Delta_K}\,,$$

then

$$\mathbf{A} - \mathbf{B}\,(\mathbf{K}_c + \mathbf{\Delta_K})\,,$$

is said to be stable.

If equation C.27 is subtracted from C.28, this results in

$$(\mathbf{A} - \mathbf{B}\mathbf{K})^T\,\mathbf{\Delta_P} + \mathbf{\Delta_P}\,(\mathbf{A} - \mathbf{B}\mathbf{K}) + {\mathbf{\Delta_K}}^T\mathbf{R}\,\mathbf{\Delta_K} = 0\,, \tag{C.29}$$

which is also a Lyapunov equation, therefore if $\mathbf{A} - \mathbf{B}\mathbf{K}$ is stable, $\mathbf{\Delta_P}$ should be positive definite according to theorem 1, leading to

$${\mathbf{\Delta_K}}^T\left(\mathbf{R}\mathbf{K}_c - \mathbf{B}^T\mathbf{P}_c\right) + \left(\mathbf{R}\mathbf{K}_c - \mathbf{B}^T\mathbf{P}_c\right)\mathbf{\Delta_K} + {\mathbf{\Delta_K}}^T\mathbf{R}\,\mathbf{\Delta_K} > 0 \;\; \forall \mathbf{\Delta_K}\,, \tag{C.30}$$

where

$$\mathbf{R}\mathbf{K}_c - \mathbf{B}^T\mathbf{P}_c = 0\,, \tag{C.31}$$

from this equation the feedback matrix can be obtained

$$\mathbf{K}_c = \mathbf{R}^{-1}\mathbf{B}^T\mathbf{P}_c\,, \tag{C.32}$$

and if it substituted in equation C.27, the algebraic Riccati equation is obtained

$$\mathbf{P}_c\mathbf{A} + \mathbf{A}^T\mathbf{P}_c - \mathbf{P}_c\,\mathbf{B}\mathbf{R}^{-1}\mathbf{B}^T\mathbf{P}_c + \mathbf{Q}_x = 0\,. \tag{C.33}$$

D

ADDITIONAL PLOTS

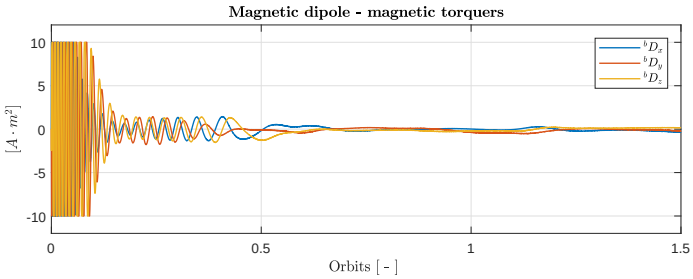

Figure D.1: DTM: Control inputs in nominal conditions.

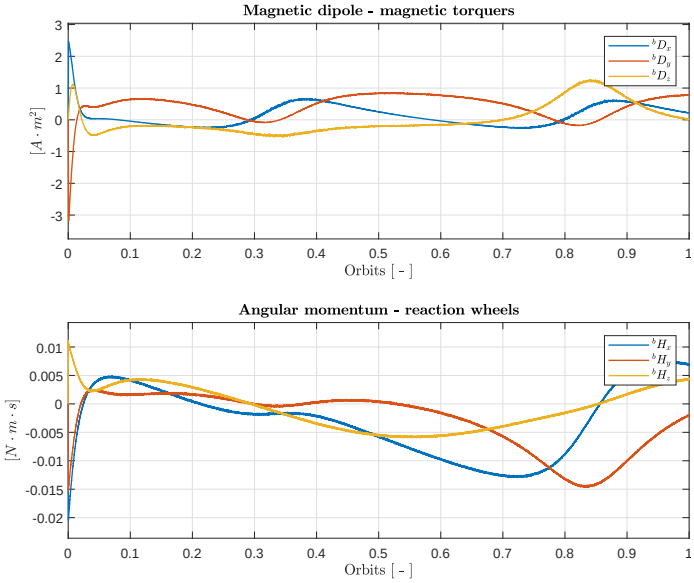

Figure D.2: NOM: Control inputs in nominal conditions for NPM.

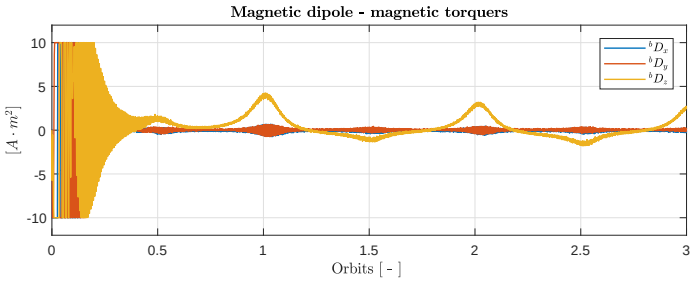

Figure D.3: CAM: Control inputs in nominal conditions.

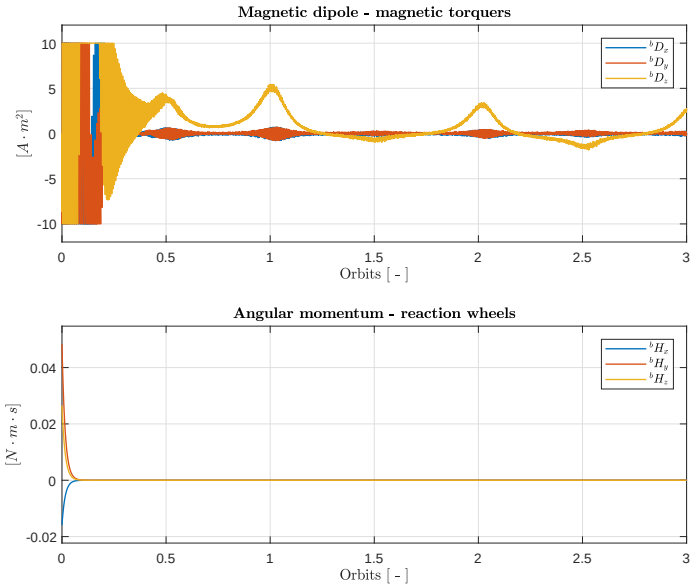

Figure D.4: SFM: Control inputs in nominal conditions.

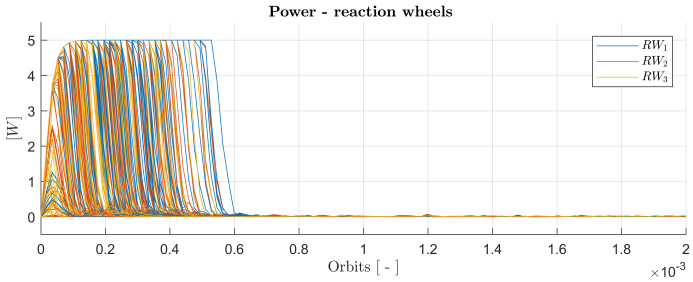

Figure D.5: Monte-Carlo simulation for 100 runs: NOM (NPM)- RWs power.

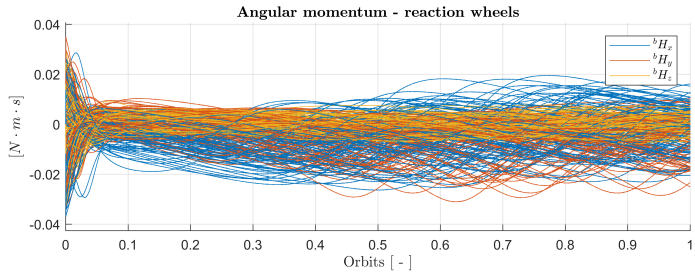

Figure D.6: Monte-Carlo simulation for 100 runs: NOM (NPM) - RWs angular momentum.

BIBLIOGRAPHY

[1] Alazard, D. (2016). *Lecture notes in Robust Control*. Institut Supérieur de l'Aéronautique et de l'Espace(ISAE). vii, 80

[2] Alminde, L., Bisgaard, M., Vinther, D., Viscor, T., and Ostergard, K. (2003). Educational value and lessons learned from the AAU-CubeSat project. In *Recent Advances in Space Technologies, 2003. RAST '03. International Conference*, pages 57–62. 40

[3] Anderson, B. and Moore, J. (2007). *Optimal Control: Linear Quadratic Methods*. Dover Books on Engineering. Dover Publications. 79

[4] Antonio Martelo (2017). S2TEP: S2TEP-Reference Mission Document. Technical Report STP-SYS-RP-0004, German Aerospace Center (DLR). 1, 2

[5] Avanzini, G. and Giulietti, F. (2012). Magnetic Detumbling of a Rigid Spacecraft. In *Journal of Guidance, Control and Dynamics*, volume 35:4, pages 1326–1334. American Institute of Aeronautics and Astronautics. 40

[6] Berlin Space Technologies AG (2010). St-200: Miniaturized autonomous star tracker datasheet. 35

[7] Capderou, M. (2006). *Satellites: Orbits and Missions*. Springer Science & Business Media. 69

[8] de Ruiter, A. (2011). A fault-tolerant magnetic spin stabilizing controller for the JC2Sat-FF mission. *Acta Astronautica*, 68(1):160–171. 41, 42

[9] Deutsches Zentrum für Luft- und Raumfahrt (2007). Phoenix: Spaceborne gps receiver datasheet. 36

[10] Diebel, J. (2006). Representing Attitude: Euler Angles, Unit Quaternions and Rotation Vectors. *Stanford University*. 66

[11] ESA Requirements and Standarts Division (November 15, 2008). ECSS-E-ST-10-04C, Space Engineering: Space Environment. Technical report, ESA-ESTEC. 17, 20, 23

[12] Farell, J. A. and Barth, M. (1999). *The Global Position System & Inertial Navigation*. McGraw-Hill Education, US. 74

[13] Federal Agency for Cartography and Geodesy (2013). *International Earth Rotation and Reference Systems Service (IERS)*. `https://www.iers.org/`. "Visited on June 7th, 2017". 70

[14] Federal Agency for Cartography and Geodesy (2016). *International Terrestrial Referemce Frame (ITRF)*. `http://itrf.ensg.ign.fr/`. "Visited on June 8th, 2017". 71

[15] Flatley, T. W., Morgenstern, W., Reth, A., and Bauer, F. (1997). A B-dot acquisition controller for the RADARSAT spacecraft. In *NASA conference publication*, pages 79–90. NASA. 40

[16] Grundmann, J. T., Auster, U., Baturkin, V., Bellion, A., Bibring, J.-P., Biele, J., Boden, R., Bompis, O., Borgs, B., Bousquet, P., Canalias, E., Celotti, L., Cenac-Morthe, C., Cordero, F., Deleuze, M., Evesque, C., Findlay, R., Fredon, S., Glaßmeier, K. ., Granena, D., Grimm, C., Grott, M., Hamm, V., Hendrikse, J., Hercik, D., Ho, T.-M., Jaumann, R., Krause, C., Kroth, R., Ksenik, E., Lange, C., Lange, M., Mierheim, O., Okada, T., Reill, J., Sasaki, K., Schmitz, N., Sedlmayr, H.-J., Talapina, M., Tangruamsub, S., Termtanasombat, N., Ulamec, S., Wejmo, E., Wrasmann, M., Yoshimitsu, T., Ziach, C., and the MASCOT team (2015). Mobile Asteroid Surface Scout (MASCOT) - Design, Development and Delivery of a Small Asteroid Lander Aboard Hayabusa2. In *4th IAA Planetary Defense Conference – PDC 2015*, IAA Scientific Activities. IAA. 1

[17] Grundmann, J. T., Mottola, S., Baturkin, V., Behrens, J., Biering, B., Drentschew, M., Drobczyk, M., Gerené, S., Hahn, G., Hallmann, M., Hartmann, J., Heidecker, A., Kazeminejad, B., Kührt, E., Lieder, M., Lötzke, H.-G., Michaelis, H., Schlotterer, M., Schmitz, N., Siemer, M., and Spietz, P. (2009). From Observational Geometry to Practical Satellite Design: AsteroidFinder/SSB. In *1st IAA Planetary Defense Conference*. ESA. 1

[18] Hauslage, J., Lebert, M., and Müller, H. (2014). Eu:CROPIS – Euglena and Combined Regenerative Organic-food Production in Space. In *Life in Space for Life on Earth (Joint Life Sciences Meeting of ISGP, ESA and CSA)*. 1

[19] Heidecker, A., Kato, T., Maibaum, O., and Hölzel, M. (2014). Attitude Control System of the Eu:CROPIS Mission. In *65th International Astronautical Congress*. International Astronautical Federation. 40

[20] Heidecker, A. and Schlotterer, M. (May 12, 2017). Eu:CROPIS: AOCS Analysis Report. Technical Report EC-AOCS-RP-0009, German Aerospace Center (DLR). 7, 26, 29, 33, 57

[21] Heidecker, A., Steffes, S. R., Reershemius, S., and Theil, S. (2012). Attitude Control System for the CLAVIS Nano Satellite Bus. In *Deuscher Luft- und Raumfahrtkongress 2012*. 40

[22] Hendricks, E., Jannerup, O., and Sørensen, P. H. (2008). *Linear Systems Control: Deterministic and Stochastic Methods*. Springer-Verlag Berlin Heidelberg. 77

[23] Hintz, G. R. (2015). *Orbital Mechanics and Astrodynamics: Techniques and Tools for Space Missions*. Springer. 68, 69

[24] Hughes, P. C. (2012). *Spacecraft Attitude Dynamics*. Dover Books on Aeronautical Engineering. Dover Publications, New York, US. 37, 64

[25] Klumpp, A. R. (1977). Singularity-free Extraction of a Quarternion from a Direction-Cosine Matrix. *Journal of Spacecraft and Rockets*, 13. 64

[26] Kramer, H. J. and Cracknell, A. P. (2008). An overview of small satellites in remote sensing. *International Journal of Remote Sensing*, 29(15):4285–4337. 1

[27] Kuipers, J. B. (1999). *Quaternions and Rotation Sequences*, volume 66. Princeton University Press. 65, 66

[28] Maciejowski, J. M. (1989). *Multivariable Feedback Design*. Electronic Systems Engineering Series. Addison-Wesley. 79

[29] Mainie, A. K. and Varsha, A. (2014). *Satellite Technology: Principles and applications*. Wiley and Sons. 68

[30] Markley, F. L. and Crassidis, J. L. (2014). *Fundamentals of Spacecraft Attitude Determination and Control*. Springer, New York, US. 37, 38, 75

[31] McCarthy, D. D. and Gérard, P. (2004). IERS Conventions 2003. Technical report, International Earth Rotation and Reference Systems (IERS). 70, 71

[32] Montenbruck, O. and Gill, E. (2012). *Satellite Orbits: Models, Methods and Applications*. Springer Science & Business Media. 69, 70, 72

[33] NASA (January, 1971). Spacecraft Aerodynamic Torques. Technical report, NASA. 16

[34] NASA (March, 1969b). Spacecraft Magnetic Torques. Technical report, NASA. 14

[35] NASA (May, 1969a). Spacecraft Gravitational Torques. Technical report, NASA. 13

[36] NASA (October, 1969c). Spacecraft Radiation Torques. Technical report, NASA. 16

[37] Ogata, K. (1997). *Modern Control Engineering (3rd Ed.)*. Prentice-Hall, Inc., Upper Saddle River, NJ, USA. 78

[38] Royal Observatory of Belgium (2017). *Sunspot Index and Long Term Solar Observations*. `http://www.sidc.be/silso/monthlyssnplot`. "Visited on June 22th, 2017". ix, 18

[39] Ruiter, A. H., Damaren, C. J., and Forbes, J. R. (2013). *Spacecraft Dynamics and Control: An Introduction*. Wiley, West Sussex, UK. 37

[40] Sarda, K., Grant, C., Eagleson, S., Kekez, D. D., and Zee, R. E. (2010). Canadian Advanced Nanospace Experiment 2 Orbit Operations: Two Years of Pushing the Nanosatellite Performance Envelope. In *ESA Small Satellites, Services and Systems Symposium*. 40

[41] Sensonor (2015). Stim300 inertial measurement unit datasheet. 33

[42] Sidi, M. J. (1997). *Spacecraft Dynamics & Control: A Practical Engineering Approach*. Cambridge University Press, Cambridge, UK. 30, 31, 37, 43, 44, 52, 64, 72

[43] Sinclair Interplanetary (2016). *Microsatellite Reaction Wheels (RW3-0.0060) datasheet*. 32

[44] Slotine, J.-J. E. and Li, W. (1991). *Applied Nonlinear Control*. Prentice Hall Englewood Cliffs, NJ. 77

[45] Solar MEMS (2017). Ssoc-d60 datasheet. 35

[46] Spröwitz, T., Bauer, W., Drobczyk, M., Nohka, F., and Heidecker, A. (2010). CLAVIS – Erste Schritte zu einer standardisierten NanoSat-Plattform. In *Internationale Luft- und Raumfahrtaustellung 2010*. 1

[47] Standish, E. M. (2006). *Keplerian Elements for Approximate Positions of the Major Planets*. 70

[48] Stephan Theil (2017). S2TEP: Time and Reference Frames. Technical Report STP-SYS-TN-0087, German Aerospace Center (DLR). 71

[49] Thébault, E., Finlay, C., and Toh, H. (2015). International Geomagnetic Reference Field: The 12th generation. *Earth, Planets and Space*, 67(1):158. 14, 33

[50] Volodymyr Baturkin (2017). S2TEP: Subsystem Specification - Thermal Control. Technical Report STP-TCS-SP-0207, German Aerospace Center (DLR). 7

[51] Wertz, J. R. (1978). *Spacecraft Attitude Determination and Control*. Astrophysics and Space Science Library. Kluwer Academic Publishers, Dordrecht, Netherlands. 13, 14, 15, 16, 27, 37, 64

[52] Wertz, J. R. and Larson, W. (1999). *Space Mission Analysis and Design*. Space Technology Library. Springer, New York, US. 14, 15, 16, 17, 25, 26, 29

[53] Zarm Technik AG (2009a). *Magnetic Torquers for S/C Attitude Control datasheet*. 29

[54] Zarm Technik AG (2009b). *Magnetometers for S/C Attitude Determination datasheet*. 34

[55] Zentrum für Angewandte Raumfahrttechnologie und Mikrogravitation and Deutsches Zentrum für Luft- und Raumfahrt (2015). *HPS - High Performance Satellite Dynamics Simulator*. Bremen, Germany. 3